Ca' Foscari
University
of Venice

Department of Molecular Sciences and Nanosystems

Master's Degree Programme
in Science and Technology of Bio and Nanomaterials

Master's Degree Thesis

**High Entropy Layered Double Hydroxides
as Robust Trifunctional Catalysts for Enhanced
Water Splitting and Ethanol Electrooxidation**

Supervisor
Dr. Kassa Belay Ibrahim

Co-supervisor
Prof. Alberto Vomiero

Graduand
Adham Haredy
896968

Academic Year
2024/2025

وَمَا تَوْفِيقِي إِلَّا بِاللَّهِ ۚ عَلَيْهِ تَوَكَّلْتُ وَإِلَيْهِ أُنِيبُ

My success is not but through Allah.
Upon him I have relied, and to Him I return.
[Qur'an | Surah Al-Hud | 11:88]

A chi lotta per la rivoluzione e la libertà.
Alla Palestina, al coraggio del popolo di Gaza.

ABSTRACT

The desire for a sustainable and clean energy future continues to concern the scientific community. Green hydrogen production via water electrolysis offers a sustainable, carbon-neutral pathway to meet future energy demands. However, most of the energy lost in conventional water electrolysis is limited by the sluggish kinetics of the oxygen evolution reaction (OER), leading to high overpotentials and reduced system efficiency.

Considering the overall water splitting, the OER process requires a high voltage to drive it; therefore, substituting OER with an electro-oxidation reaction with a lower theoretical potential is an efficient methodology to alleviate this issue. Recently, as an alternative to traditional hydrogen production from electrocatalytic water splitting, many readily oxidizable molecules, including alcohols, have been deployed to replace the OER process and improve energy efficiency. The ethanol oxidation reaction (EOR) usually competes with the OER at working potentials, serving as an alternative anodic process to overcome the kinetic limitations of OER. Developing highly active electrocatalysts through simple and quick methods remains challenging. In response, high-entropy materials have recently gained attention as promising electrocatalysts due to their structural stability, tunable composition, and synergistic interactions among diverse metal constituents.

Herein, we introduce the concept of a high-entropy layered double hydroxide (HE-LDH) catalyst composed of Ni, Fe, Cu, Mg, and In, engineered to function as a robust trifunctional electrocatalyst capable of efficiently driving the HER, OER, and EOR. The HE-LDH was synthesized via hydrothermal treatment process at 120 °C for 12 hours, using a defined metal precursor molar ratio (Ni:Fe:Cu:Mg:In = 3:1:0.5:0.5:0.5). To further optimize performance, the etching process using a two-step liquid-phase was applied for different etching times (10, 20, 20, and 60 minutes), with the 20-minutes etched sample demonstrating the best electrochemical properties.

Different characterization techniques including X-ray diffraction (XRD), Scanning Electron microscopy (SEM), Energy-Dispersive X-Ray Spectroscopy (EDS), and X-ray photoelectron spectroscopy (XPS) were used to confirm the HE-LDHs. Electrochemical tests in alkaline media (0.5 M KOH) for HER and OER; (0.5 M KOH + 1 M EtOH) for EOR were measured. The HER overpotential reduced from 507 mV (NiFe-LDH) to 321 mV (HE-LDH), and further to 187 mV after etching. For OER, overpotentials reduced from 169 mV (NiFe-LDH) to 150 mV (HE-LDH), and 143 mV after etching, while EOR saw reductions from 148 mV (HE-LDH) to 143 mV after etching.

Corresponding Tafel slope improvements were observed: for HER, from 266.61 mV/dec to 136.69 mV/dec; for OER, from 226.64 mV/dec to 87.98 mV/dec; and for EOR, from 100.01 mV/dec to 56.83 mV/dec. Electrochemical impedance spectroscopy (EIS) and electrochemical active surface area (ECSA) analyses further substantiated these findings. Charge transfer resistance for HER/OER decreased from 160 Ω (NiFe-LDH) to 65 Ω (HE-LDH) and 25 Ω after etching, with ECSA increasing from 0.079 mF/cm² to 0.32 mF/cm². For EOR, EIS dropped from 125 Ω to 40 Ω after etching, indicating improved charge mobility and catalytic site exposure.

In addition, after 100 hours of continuous operation for both HER and EOR the catalytic performance of et-HELDH (20 min) shows no obvious deterioration. The rich selectivity of the elements and the fine regulation of the nanostructure injects new vitality into the performance improvement of high-entropy catalyst. These findings highlight the transformative potential of high-entropy engineering and fine nanostructure control open opportunities to solve the problems of low intrinsic activity, very few active sites, instability, and low conductance.

ACKNOWLEDGEMENT

TABLE OF CONTENTS

LIST OF FIGURES

LIST OF TABLES AND CHARTS

LIST OF ABBREVIATIONS

LDH	Layered Double Hydroxide
ME-LDH	Medium Entropy Layered Double Hydroxide
HE-LDH	High Entropy Layered Double Hydroxide
et-HELDH	Etched High Entropy Layered Double Hydroxide
HEOs	High Entropy Oxides
HEMs	High Entropy Materials
HEAs	High Entropy Alloys
GHGs	Greenhouse gases
HER	Hydrogen Evolution Reaction
OER	Oxygen Evolution Reaction
EOR	Ethanol Oxidation Reaction
DEFC	Direct Ethanol Fuel Cell
PGMs	Platinum group materials
OH^-	Hydroxide ions
MOOH	Metal oxyhydroxide
XRD	X-ray Diffraction
SEM	Scanning Electron Microscopy
TEM	Transmission Electron Microscopy
EDS / EDX	Energy Dispersive X-ray Spectroscopy
XPS	X-ray Photoelectron Spectroscopy
JCPDS	Joint Committee on Powder Diffraction Standards
η	Overpotential
I	Current
J	Current density
cps/eV	Counts Per Second per Electron Volt
R_{ct}	Charge transfer resistance
C_{dl}	Double-Layer Capacitance
At%	Atomic Percent
NF	Nickel Foam
CC	Carbon Cloth
GC	Glass Carbon
ITO	Indium Tin Oxide
CNT	Carbon Nanotubes
LSV	Linear Sweep Voltammetry
EIS	Electrochemical Impedance Spectroscopy
CV	Cyclic Voltammetry
ECSA	Electrochemical active surface area
CA	Chronoamperometry
CP	Chronopotentiometry
RHE	Reversible Hydrogen Electrode
SHE	Standard Hydrogen Electrode
Ag/AgCl	Silver/Silver chloride electrode

CHAPTER 1. INTRODUCTION

1.1 GLOBAL ENERGY DEMANDS AND THE PROMISE OF HYDROGYN AS A GREEN ENERGY CARRIER

In the 21st century, we are faced with a challenge, meeting the increasing global demand, for energy while also addressing the negative impacts of climate change.[1] The use of fossil fuel-based energy systems, which have been crucial for development has proven to be unsustainable due to their limited availability and environmental repercussions.[2-4] Since the industrial revolution, our reliance on fossil fuels has led to a dramatic rise in CO_2 and other greenhouse gases (GHGs), which have significantly contributed to global warming.[5-9] Therefore, shifting towards alternative sources of clean, sustainable, and renewable energy is crucial for achieving future energy sustainability and ensuring global security.[10,11] According to a recent survey on the availability of coal and hydrocarbons, it is very clear that in 50 to 60 years, there will not be sufficient carbon to burn to meet energy requirements.[12-14] Hence, it is necessary to adapt to an alternate fuel source while simultaneously ensuring that the new fuel we are introducing is not accompanied by any of the negative impacts of carbonaceous fuels.[12-14]

Hydrogen is the simplest element in the periodic table. Hydrogen gas is also one of the lightest i.e. 14 times light compared to air and 57 times lighter than gasoline. Apparently, hydrogen covers 75% of the universe's mass. Hydrogen gas has a very highly flammable range (between 4%-75% in air) in contrast to traditional fuels. Using hydrogen as alternative fuel to conventional fuel could lead to a new era of cheap, clean and renewable energy. Unlike other traditional fuels, when hydrogen is burned with oxygen, it doesn't emit any carbon base by product. The output of hydrogen combustion with oxygen is water, electricity and heat energy. Therefore, Hydrogen can serve a wide range of energy services.[15] Many countries like Canada, Scotland, Germany, and Norway have already started to use the hydrogen as an alternate transportation fuel to diesel and petrol. [16]

Hydrogen (H2) fuel has been identified as one of the top priorities by energy researchers.[17] Since H2 is clean and cost-effective, with high gravimetric energy density (120 MJ/kg), it proves to be an energy alternative for coming generations.[18,19] Currently, around 95% of the world's total hydrogen (H2) production (65 million tons) is done by natural gas reforming/combustion. which require high temperature and pressure. The global hydrogen energy requirement has achieved 94 Mt in 2021, which is a 5% increase from 2020.[20] Predictions show that in 2030 hydrogen energy demand will reach 180 Mt, providing up to 18% of the world's final energy demand, which benefits heavy industry, hydrogen-based fuels, and power generation. [21] Currently, 75 Mt of pure H2 and 45 Mt of mixed gases with H2 are produced per year.[22] The global hydrogen market will grow from $142 billion in 2019 to $209 billion in 2027. Green and sustainable hydrogen generation allows for low-cost and highly efficient technology that is crucial for the deployment of the hydrogen economy at the terawatt scale.[23] Otherwise, it is not possible for green hydrogen to compete with grey hydrogen from fossil fuels (e.g., Methane reforming).

1.2 WATER ELECTROLYSIS AS A SUSTAINABLE PATHWAY FOR HYDROGEN PRODUCTION

Electrochemical water splitting as a promising hydrogen production method attracted great interest in the past decades.[17,18] Water electrolysis technology has emerged as an alternative, reliable method for generating H2 as an efficient and sustainable green energy. [24,25] Water electrolysis outruns the performance of most other conventional techniques, which involve two half-reactions, namely HER and OER.[26] Hence, electrochemical water splitting has been accepted as a means of secondary storage of energy on a large scale as chemical fuel. With these requisites, researchers worldwide recently accepted that H2 is the only fuel which can provide a solution to all energy-related environmental problems and aid in making the Earth green again.[27-29] At present, there are several methods for hydrogen production, namely water electrolysis,[30–33] photoelectrocatalytic water splitting,[34-36] steam reformation of hydrocarbons,[37–39] acidic hydrolysis of reactive metals and hydrolysis of metal hydrides (also known as 'on-demand H2 generation')[40–42] Among these, water electrolysis is superior in many ways.[35,43-45] Photoelectrochemical water splitting is a greener method for producing highly pure H2 because it directly utilizes photons to generate H2. However, the quantity of H2 produced even after several days is still less than 100 mL in volume, which means that although this method is greener, the poor quantity of H2 produced per unit time makes it the least efficient option for H2 production; for the same reason, this method cannot be adopted for large and immediate generation of H2.[46–47] Hydrolysis of reactive metals, metal hydrides and alkali and alkaline earth metal borohydrides is a relatively rapid method of producing H2 in large quantities. However, the sources are always toxic metals, metal hydrides and borohydrides that are synthesized via fine chemical industries on a large scale while polluting the environment. This means once again that this method cannot be adopted as a greener way of producing H2 when very large amounts are required, although it is rapid.[48-51] Steam reforming of hydrocarbons at high pressure and temperature is a large scale H2 production method in current use. However, due to the use of high pressure and temperature, it is as hazardous as carbonaceous fuels to the environment and also to human health.[37-39] Moreover, the H2 obtained by this method is of poor quality and is always accompanied by oxides of N, S and C. Due to these impurities, the use of H2 obtained by steam reforming of hydrocarbons in fuel cells is not advised because the impurities will poison the catalytic surface and reduce its cycle life drastically.[35,43]

Given that water electrolysis is the best method to produce highly pure H2 on a large scale within short periods of time and with much less harm to the environment, studies on improving the cell performance of water electrolysers are very attractive. The following equation is the simplest description of the electrochemical splitting of water into H_2 and O_2 in neutral conditions. $H_2O(l) \rightarrow H_2(g) + 1/2 O_2(l)$ E0 = 1.23 V vs. SHE. However, to minimize the accompanying energy loss, water electrolysis should be performed either in highly acidic conditions (such as in 0.5 M H2SO4) or in highly alkaline conditions (such as in 1 M KOH).[28,35] Electrolysis carried out in both these extreme pH conditions has its own advantages and disadvantages.

1.3 ROLE OF CATALYSTS IN HER

Catalysts play a crucial role in enhancing the efficiency and viability of the HER, a key half-reaction in water electrolysis for hydrogen production. The HER involves the reduction of protons to molecular hydrogen at the cathode, a process that, in the absence of a catalyst, is kinetically hindered and requires a high overpotential. Catalysts lower this energy barrier, thereby accelerating the reaction rate and improving overall energy efficiency. Platinum-group metals (PGMs), especially platinum (Pt), are the benchmark HER catalysts due to their near-zero overpotential and exceptional catalytic activity in both acidic and alkaline media. Tremendous advancements have been made in recent years to replace these precious metals, particularly for HER, which had previously been catalyzed solely by Pt.[34,52-55] Materials such as 3d metal phosphides,[31,35,43,55-57] sulfides,[58–67] and selenides[43,68–86] were recently reported to be highly active for HER in both acidic and alkaline media. In some cases, these materials were proven to be even more effective than Pt in high-current water electrolysis, with better endurance in long term electrolysis.[31,35,43,87-89]

1.4 ROLE OF CATALYSTS IN OER

Catalysts are essential to overcoming the intrinsic sluggish kinetics of the OER, the anodic half-reaction in water electrolysis, which involves the four-electron oxidation of water to molecular oxygen. Due to its complex multi-step mechanism and high energy barriers, OER typically demands substantial overpotential, significantly limiting the overall efficiency of electrochemical water splitting. Catalysts reduce these overpotentials by stabilizing reaction intermediates and facilitating electron transfer, thus enhancing both reaction rate and energy efficiency. Concerning OER in acidic conditions, IrO_2 and RuO_2 are still the most stable catalysts.[45,90-96] Many attempts have been made to use the 3d iron group metals by alloying them with minimal Ir or Ru for applications in catalyzing OER in acidic environments. However, due to the rapid solubility of Co, Ni and Fe metals, they are unsuitable for OER in acid, although they possess impressive OER activity in alkaline medium.[45,90] Later, researchers turned their attention to minimizing the use of Ir and Ru by alloying them with post-transition metals such as Sn, Pb and Sb.[97,110] Although these post-transition metals possess significantly lower OER activities, they act as stable synergistic materials with oxides of Ir and Ru during OER in acidic environments.[97,98,100,101,103-109] Materials such as 3d transition metal oxides,[111-114] hydroxides,[57,83,115-121] and LDHs [122-137] have been found to be better performing electrocatalysts for alkaline OER; they are frequently reported with different structural and electronic modifications as nanomaterials. Moreover, materials such as 3d transition metal chalcogenides,[34,35,52,138,139] pnictogenides,[31,55,140] and carbides[141,142] are also reported to be highly active pre-catalysts for OER in alkaline conditions. Many of these materials have been shown to be more active and stable than both Ir and Ru oxides for OER electrocatalysis in alkaline medium. However, because Pt has poor HER kinetics in alkaline medium, the advantages of these high-performance alkaline OER electrocatalysts received little attention in earlier stages.[143,144] Then, catalysts based on transition metal phosphides emerged in the field of water electrolysis with good HER kinetics in alkaline medium;

these discoveries raised hope that highly active alkaline OER electrocatalysts could be used in combination with transition metal phosphides for total water splitting. [31,35,55]

1.5 MOTIVATION AND SCOPE OF THE RESEARCH

The increasing global demand for sustainable and clean energy sources has placed green hydrogen at the forefront of energy research and development. Among the various production routes, water electrolysis powered by renewable energy has emerged as a promising and environmentally benign method for generating high-purity hydrogen. However, one of the major technical challenges limiting the widespread adoption of water electrolysis is the sluggish kinetics of the OER, which significantly increases the required energy input and reduces overall system efficiency. To address this challenge, the design and development of highly active, stable, and cost-effective electrocatalysts for both the HER and OER are of critical importance. Traditional noble-metal-based catalysts, while highly efficient, suffer from scarcity, high cost, and limited long-term stability. This creates a compelling need to explore alternative catalyst materials that can deliver comparable or superior performance. High-entropy materials, particularly HE-LDHs, offer a new horizon in catalyst design due to their exceptional structural versatility, compositional tunability, and synergistic effects arising from multi-element interactions. Incorporating multiple metal species in equimolar or near-equimolar ratios enhances the catalytic active site density, electron transfer properties, and overall durability. Moreover, the potential of HE-LDHs to serve as trifunctional catalysts simultaneously catalyzing HER, OER, and EOR presents an exciting opportunity to develop integrated and energy-saving approaches for hydrogen production and green chemical synthesis. This research explores the concept of HE-LDHs as trifunctional catalysts for HER, OER, and EOR in alkaline media. The scope includes a systematic investigation of compositional effects, defect engineering, and structure–activity correlations, with the goal of understanding and optimizing the catalytic mechanisms at play. The study seeks to position HE-LDHs as next-generation catalysts that address existing performance gaps in sustainable electrochemical energy systems.

CHAPTER 2. LITERATURE REVIEW

2.1 THERMODYNAMICS AND KINETICS OF WATER ELECTROLYSIS

Water electrolysis is an electrochemical process that utilizes electrical energy to split water (H_2O) into their elemental gases; hydrogen (H_2) and oxygen (O_2). Water electrolysis is widely considered a promising method for storing renewable electricity in the form of hydrogen fuel. This reaction occurs within an electrochemical cell that consists of two electrodes (anode and cathode) immersed in an electrolyte, which serves to conduct ions and separate the half-reactions spatially. Upon application of external voltage, water molecules undergo redox (reduction-oxidation) reactions at the electrode surfaces. Anions migrate toward the positively charged anode where oxidation occurs (loss of electrons), while cations move toward the negatively charged cathode where reduction takes place (gain of electrons). The overall reaction is a redox process, involving both oxidation and reduction: $2H_2O$ (l) $\rightarrow$ $2H_2$ (g) + O_2 (g) is shown in **Figure 1**. This reaction is thermodynamically non-spontaneous under standard conditions and requires an energy input of at least 1.23 V to overcome the strong O–H bonds in water molecules. The two critical half-reactions are typically described as follows: at the anode, OER takes place either $2H_2O \rightarrow O_2 + 4H^+ + 4e^-$ in acidic media or $4OH^- \rightarrow O_2 + 2H_2O + 4e^-$ in alkaline media while at the cathode, the HER occurs either $4H^+ + 4e^- \rightarrow 2H_2$ in acidic media or $2H_2O + 2e^- \rightarrow H_2 + 2OH^-$ in alkaline conditions.[90,91, 145,146]
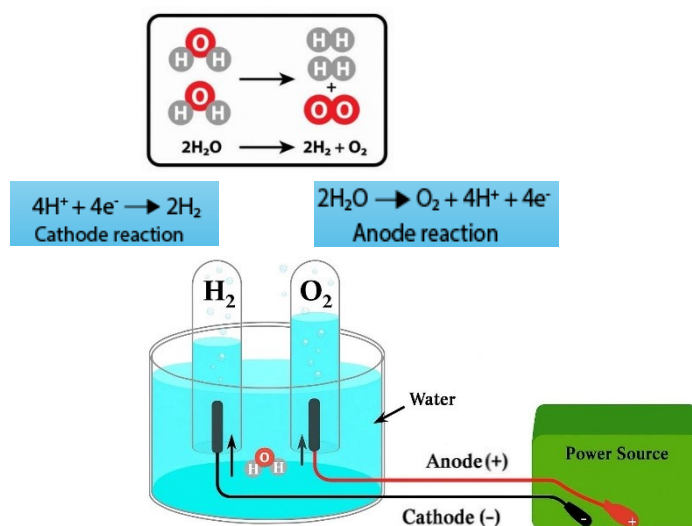
Figure 1. Schematic Illustration of the basic water electrolysis Process

The mechanism of OER is complicated, involving slower kinetics than HER due to four-electron transfer to achieve the evolution of oxygen. OER is the half-reaction of water splitting under acidic (Eqn. (1)) and alkaline (Eqn. (2)) conditions, suggesting the four-electron transfer process [147]. The OER process is carried out effectively in the alkaline media, and the formation of intermediates (M to MOOH) is shown in (Eqns. (3)–(7)). The schematic illustration of the OER pathway is shown in **Figure 2** (a).

Initially, the hydroxide ions (OH^-) adsorbed on the active sites (M - OH) and oxidized to donate an electron to the electrode surface. In the second step, another OH^- group is adsorbed on the M - OH site forming MO (Eqn. (2)). M - O experiences two different pathways to form O2 molecules. On the one hand, the direct reaction involving 2M - O produces $O_2(g)$ (Eqn. (3)). On the other hand, the M - O converts into the oxyhydroxide M-OOH intermediates after the addition of the third hydroxide ion with the third electron transfer. Finally, the fourth hydroxide ion is adsorbed on the M-OOH species to generate oxygen (O_2) and the active sites for further hydroxyl species adsorption. The universalized reaction mechanism involved in OER includes the following steps of metal (M) into intermediates (M - OH, M - O, and M-OOH).

In particular, the reaction energy of each elementary step and the OER scaling relationship between the real and ideal electrocatalyst reveal the binding energy of the metal surface for the adsorbed hydroxide ions, is shown in **Figure 2** (b). ΔG represents the free energy of formation for the reaction intermediates which is exothermic/energy releasing when negative and endothermic/energy consuming when positive. E0 denotes the standard reversible electrode potential of the HER, E1, E2, and E3 represent the different electrode potentials, and η is the overpotential. The energetics of real and ideal catalysts at various electrode potentials are better illustrated. At the electrode potential E1, for either catalyst, all steps are uphill, so OER cannot proceed. ΔG for the reaction intermediates determines the potential determining step in most electrochemical conversion reactions. Hence, Eqn. (7) describes the potential limiting step for OER, which ascribes the required high potential of 1.23 V to drive the electrocatalytic reaction.

If the kinetic limitations are negligible, the ideal catalyst has no overpotential at the reversible electrode potential. To make all steps downhill for the real electrocatalyst, E3 is required, at which OER can occur at a prescribed pace.[148] As a result of irregular variations in the adsorption energies of the intermediate species, the binding energies for each step are different. The strong binding energy of O2 will increase the complication of M-OOH formation, and the weak binding energy of oxygen to the surface can increase the difficulty of M - O formation.[149]

Acidic OER half-reaction: $2H_2O \rightarrow O_2 + 4H+ + 4e^-$ (1)

Alkaline OER half-reaction: $4OH^- \rightarrow O_2 + 2H_2O + 4e^-$ (2)
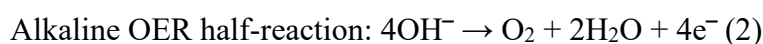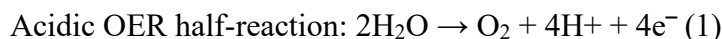
The reaction mechanism of OER under alkaline conditions is as follows:

$$M + OH^- \rightarrow M\text{-}OH + e^- \qquad (3)$$

$$M\text{-}OH + OH^- \rightarrow M\text{-}O + H_2O \qquad (4)$$

$$2M\text{-}O \rightarrow 2\,M + O_2\,(g) \qquad (5)$$

$$M\text{-}O + OH^- \rightarrow M\text{-}OOH + e^- \qquad (6)$$

$$M\text{-}OOH + OH^- \rightarrow M + O_2(g) + H_2O + e^- \qquad (7)$$
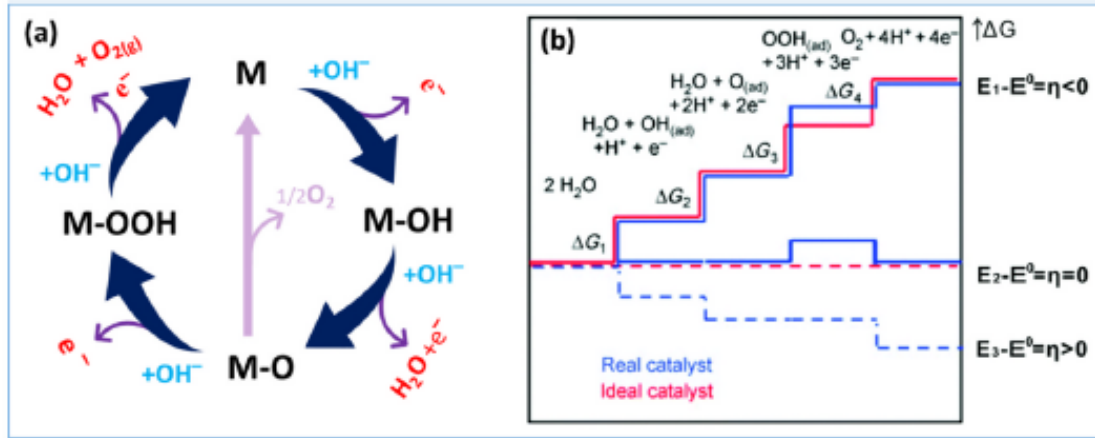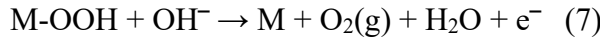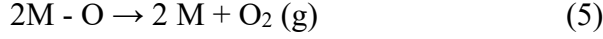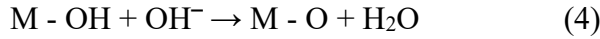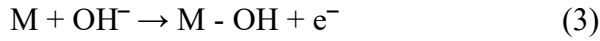
Figure 2. (a) Schematic representation of OER mechanism in the alkaline condition. (Blue line indicates the M-OOH pathway, whereas the purple line indicates the direct reaction of two (M - O) species to evolve oxygen. (b) Gibbs free energy reaction pathway plots of real and ideal electrocatalysts for OER mechanism.[149]

HER is composed of a two-step electron transfer process that takes place on the cathode, forming hydrogen (H2).[150] Initially, during HER, the protons are adsorbed (H*) on the active sites (M) of the electrode by water (H_2O) dissociation with one electron transfer from the electrode surface, which is called the Volmer step (Eqn. (6)). Subsequently, there are two possible pathways to form hydrogen (H_2). The first one is the combination of an adsorbed proton (H*) with one electron transferred from the electrode and one proton from the electrolyte, resulting in one hydrogen (H_2) molecule, which is the Heyrovsky step (Eqn. (7)). The other step is a faster reaction pathway named the Tafel step (Eqn. (8)), which involves the direct formation of an H_2 molecule from two adsorbed protons (H*) from the surface of electrocatalyst.[151]

HER in alkaline media is as follows:

$$\text{Volmer step: } M + H_2O + e^- \rightarrow M^* + OH^- \qquad (8)$$

$$\text{Heyrovsky step: } H_2O + M\text{-}H^* + e^- \rightarrow M + H_2 + OH^- \qquad (9)$$

$$\text{Tafel step: } 2M\text{-}H^* \rightarrow 2\,M + H_2 \qquad (10)$$
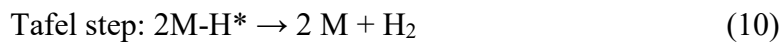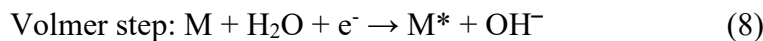
2.2 ETHANOL ELECTROOXIDATION REACTION (EOR)

Ethanol (CH_3CH_2OH) is one of the volatile organic compounds, and renewable alcohol is obtained from food crops, plants, and forest residue. Renewable and environmentally friendly fuel production pathways are increasingly needed to meet future energy demands. Alcohol oxidation is an organic reaction of the alcohol functional group converted into other functional groups like ketone, aldehyde, and carboxyl acid is shown in **Figure 3**. The electrooxidation of alcohols is a great candidate for replacing OER for the production of energy-efficient hydrogen. Hence, the EOR technique is used to minimize the anodic potential and generate oxidized products.[152]
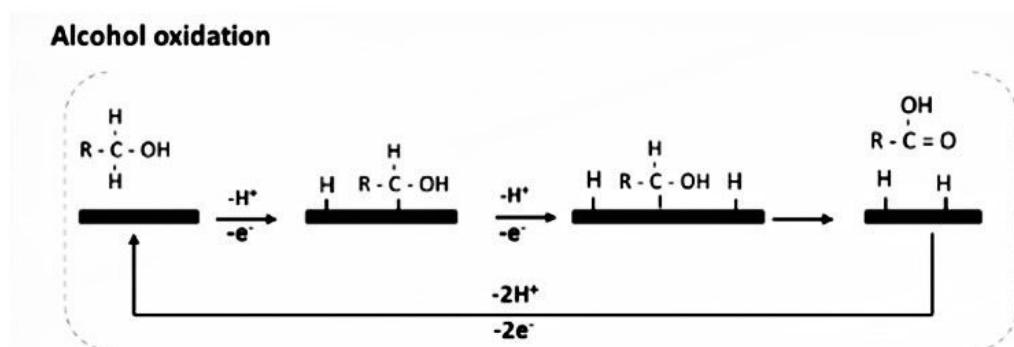
Figure 3. Schematic diagram of proposed alcohol oxidation reaction pathway.

EOR is an economical pathway in many electrochemical systems for clean energy, such as ethanol fuel cells and the anodic reaction in hydrogen generation. Noble metals, such as platinum, are benchmark catalysts for EOR owing to their superb electrochemical capability. To improve sustainability and product selectivity, nickel (Ni)-based electrocatalysts are considered promising alternatives to noble-metal EOR. Although Ni-based electrocatalysts are relieved from intermediate poisoning, their performances are largely limited by their relatively high onset potential. Therefore, the EOR usually competes with the OER at working potential, resulting in low EOR efficiency. The direct ethanol fuel cell (DEFC) is seen as a promising power conversion device for compact and automobile applications. The high efficiency electrocatalysts for the EOR have enhanced the further development of DEFCs. The EOR process is generally believed to follow a dual reaction mechanism pathway, namely the C1 pathway and C2 pathway is shown in **Figure 4**. According to the C1 pathway, electrochemical ethanol to carbon dioxide conversion with $12e^-$ transfer would benefit the overall efficiency of ethanol fuel cells. In most cases, incomplete oxidation of ethanol into acetic acid occurs through the C2 pathway. The most reported palladium-based and platinum-based electrocatalysts show a low selectivity of the C1 pathway, about 1%–7% at room temperature, even if they substantially increased the reaction rate of ethanol oxidation. As a result, it is critical and urgent that new EOR electrocatalysts can be rationally designed and prepared with high C1 pathway selectivity.[153]

Ethanol is commonly used due to its easy agricultural synthesis, less toxicity, and high energy density of 8.03 kWh kg^{-1}.[152] However, the transition metal-based electrocatalysts Fe, Ni, and Cu are generally considered the EOR catalyst, and their effectiveness in enhancing the overall electrocatalytic activity and modifying its electronic structure to form OH$^-$ species is highly desirable by-product formation of CO. The hydrogen generation method is due to low electrolyze voltage. Ethanol is oxidized to hydrogen production at low toxicity, superior chemical stability, and high hydrogen content. [153]
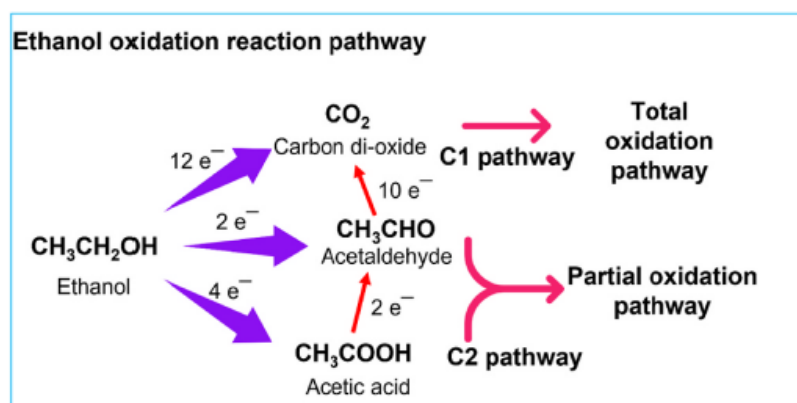
Figure 4. Schematic illustration of the parallel pathway in the ethanol oxidation reaction electron transfer process.[153]

2.3 TRIFUNCTIONAL CATALYSTS

Catalysts are materials that facilitate electrochemical reactions such as oxidation and reduction. The development of these catalysts has evolved from precious metals to more sustainable HE-LDHs. The evolution from precious metals to HE-LDHs represents a shift towards more sustainable, efficient, and affordable electrocatalysts. Currently, the single most active metal Pt for HER and IrO2 for OER are known to exhibit high water splitting activities[154,155], but their prohibitive cost and extreme scarceness have hindered their uses in practical applications. Therefore, it is significantly imperative to develop less expensive and highly active electrocatalysts that are highly competitive in terms of their performance with the counterpart noble metal-based catalysts. Toward this end, some important progress has been made in the rational design of MOF-based electrocatalysts, which have been used as a promising platform to promote OER and HER kinetics.[156-160] Recently, Zhao et al.[161] rationally designed a bimetallic NiFe-MOF electrocatalyst on nickel mesh and used this as both an anode and cathode in an electrolytic cell for overall water splitting, achieving a current density of 10 mA cm^{-2} at a voltage of 1.55 V, which was 70 mV smaller than the benchmark Pt/C cathode and IrO2 anode. Also, CoNi-MOF and CoNiN@C on copper substrates were used as the anode and cathode for water splitting, which required 1.64 V to reach 10 mA cm^{-2}.[162] Ternary Mo51Ni40Fe9 nanobelts were synthesized to achieve a remarkable water splitting performance, using Mo51Ni40Fe9 nanobelts as the anode and commercial Pt/C as the cathode, which required 1.55 V to achieve 10 mA cm^{-2} current density.[163] Lately, it has been shown that the unique 3D architecture of titania nanotubes with a deposit of palladium particles significantly reduced the potential by about <1.0 V to produce hydrogen by replacing anodic oxygen evolution with the readily oxidizable species of ethanol.[164]

Trifunctional catalysts are advanced electrocatalytic materials engineered to simultaneously facilitate three key reactions: HER, OER, and EOR. These catalysts are particularly significant in renewable energy technologies, where integrating HER and OER enables water splitting for green hydrogen production, while EOR serves as an alternative anodic process to overcome the kinetic limitations of OER. The ability of a single catalyst to efficiently catalyze all three reactions not only simplifies system design but also improves energy efficiency and cost-effectiveness by reducing the overall overpotential required for electrolysis. Trifunctional catalysts must exhibit excellent electrochemical activity, fast reaction kinetics, high surface area, and long-term structural and operational stability under alkaline conditions. Materials such as HE-LDHs have emerged as strong candidates due to their compositional diversity, tunable electronic structure, and synergistic effects among multi-metal constituents. Their capacity to act as a unified platform for HER, OER, and EOR makes them highly attractive for integrated electrochemical systems, especially those targeting hydrogen generation from water and value-added chemical production from alcohols like ethanol.
[156-161]

2.4 LAYERED DOUBLE HYDROXIDES (LDHs)

Layered double hydroxides (LDHs) are made up of two metal cations, divalent and trivalent, in the form of double layers or lamellar structures. Anions (nitrates, sulfates, or carbonates) and water molecules essentially fill the interlayer gaps between the metal hydroxide layers.[165,166] The general formula for LDHs is $[M_{1-x}^{2+}M_x^{3+}(OH)_2]^{x+}(A^{n-})_{x/n}\cdot yH_2O$, where M^{2+} and M^{3+} are the divalent and trivalent metal cations, respectively; A^{n-} is the related anion; and x is the ratio of $M^{3+}/(M^{2+} + M^{3+})$, where $(0.1 < x < 0.5)$. Furthermore, the M^{2+}/M^{3+} ratio must be in the range of 1–6[167,169] to produce LDHs. From an industrial standpoint, LDHs come from brucite, or mineral clay, which is mostly made of $Mg(OH)_2$. An equivalent amount of trivalent metal cations (M^{3+}) replaces a portion of divalent metal cations (M^{2+}) during the production of LDHs based on brucite. Consequently, positive charges are left on the surface of the layers, which are balanced by water molecules and comparable anions that occupy the interspace among the layers. The assembly of the lamellae and the formation of distinctive LDH structures are supported by the compensation of anions of the generated positive charges.[170] The hydroxide layers are contained in the cores of octahedral structures is shown in **Figure 5**, and the cations M^{2+} and M^{3+} are uniformly distributed throughout the lamellar structures.[169,171] The LDH structures are stabilized due to the electrostatic interaction among the positive charge layers and the negative charge anions present amongst these layers. The density of the remaining positively charged layers and the number of negative charge anions connected to the construction can be established by the ratio among the M^{2+} and M^{3+} cations in the framework of the LDH layers. The valence of the cations and the relationship between the different ion types significantly affect the layered double hydroxide characteristics, particularly their porosity, ion exchange propensity, and crystallinity.[172]
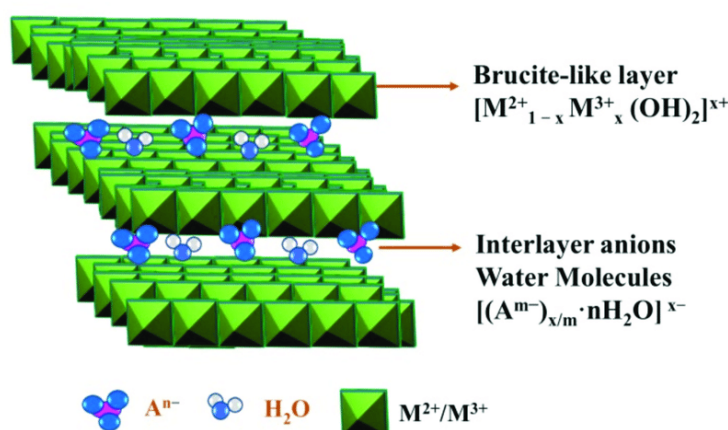
Figure 5. Schematic illustration of LDH structure and chemical component.[170]

2.5 HIGH ENTROPY MATERIALS (HEMs)

High-entropy materials (HEMs) have garnered substantial research interest over the last 15 years because of their unique properties stemming from their high configurational entropy.[173] In 2004, Cantor and Yeh et al. presented this idea.[173,174] High-entropy alloys (HEAs) are a type of HEM composed of five or more elements, each with a distinct chemical composition. To enhance their performance, HEMs with large specific surface areas, multiple active sites, and stable phase structures have been synthesized.[175-178] Various HEMs, including alloys,[179-182] oxides,[183-186], oxyfluorides,[187-189] borides,[190,191] carbides,[192,193] nitrides,[194,195] sulfides,[196,197] and phosphides[198,199] have been studied for applications in thermal electricity, thermal and environmental protection, electrochemical energy storage, and catalytic processes.

The sluggish diffusion effect due to irregular atomic arrangements and varied interactions increases the diffusion activation energy by slowing atomic movement.[200] Differences in the atomic radii result in lattice distortion, considerably affecting material characteristics.[201] HEAs, which are characterized by a high entropy of mixing (ΔS_{mix}), exhibit low Gibbs free energy ($\Delta G_{mix} = \Delta H_{mix} - T\Delta S_{mix}$) at elevated temperatures, promoting stability and atomic disorder, resulting in a more uniform distribution of atoms within the lattice.[202] These synergistic effects enhance the catalytic performance in energy conversion processes and have led to an interest in high-entropy noble-metal and noble-metal-free electrocatalysts for the oxidation of methanol,[203-205] oxygen evolution,[206-211] and reactions involving oxygen reduction. [212-214] Two-dimensional (2D) materials are solid crystals consisting of one or a few atomic layers, typically ranging from 1 to 10 Å in thickness, with lateral dimensions extending to tens of micron.[215] Among these, 2D layered hydroxides belong to a distinct subclass characterized by thin, flat sheets of metal hydroxide layers arranged in a stacked, lamellar structure. These ionic solids consist of positively charged metal hydroxide layers interspersed with interlayer gaps that encapsulate solvent molecules and anions, ensuring charge balance.

HE-LDHs offer a distinct suite of advantages, offering new opportunities for material design and functionalization. Notably, HE-LDHs share structural similarities with conventional LDHs but are distinguished by incorporating multiple metallic cations (typically five or more) into brucite-like $M(OH)_6$ octahedral layers. This high-entropy configuration enhances structural stability, thermal resistance, and catalytic performance. The positively charged layers are balanced by interlayer anions and water, with tunable basal spacing and composition, enabling the customization of properties for diverse applications.[216] HE-LDH exhibits remarkable stability under harsh conditions and possesses adjustable electronic, magnetic, and catalytic properties, making it highly promising for catalysis, energy storage, and environmental remediation. Despite extensive research on zero-dimensional and bulk high-entropy materials, their 2D counterparts, such as HE-LDHs, remain relatively underexplored. The synergy of high entropy and cocktail effects in HE-LDHs enables precise property tuning, offering substantial advantages over conventional materials in advancing renewable energy technologies and promoting environmental sustainability.[217-219]

CHAPTER 3. RESEARCH OBJECTIVES

The primary objective of this research is to design, synthesis, and optimize HE-LDHs as robust trifunctional electrocatalysts capable of efficiently catalyzing the HER, OER, and EOR under alkaline conditions. This work addresses the urgent demand for multifunctional, cost-effective, and stable catalysts for sustainable hydrogen production and organic electrooxidation by integrating the principles of HE-LDHs.

3.1 DEVELOPMENT OF TRIFUNCTIONAL HE-LDH CATALYST

Electrocatalytic activity is influenced by various parameters of the electrocatalyst, including surface area and porosity, electrical conductivity, chemical composition, crystallinity and phase purity, surface chemistry, morphology and nanostructure, electrochemical active surface area (ECSA), charge transfer resistance (R_{ct}), stability and durability. These parameters must be optimized collectively to achieve a high-performance electrocatalyst for applications like water splitting and ethanol oxidation. By varying these parameters, different results can be achieved.

The careful selection of these elements is based on their complementary electrochemical, structural, and catalytic properties, which collectively contribute to achieving superior trifunctional catalytic performance. The periodic table shown in **Figure 6** marks these ions that can be used to prepare HELHs in this strategy. Nickel (Ni^{2+}) was chosen due to its well-documented activity toward HER and OER in alkaline media. Ni forms the structural backbone of many LDHs and contributes significantly to both conductivity and catalytic performance. It provides active sites that facilitate the adsorption and desorption of hydrogen intermediates during HER and serves as a redox-active center for OER. Iron (Fe^{3+}) is a cost-effective and earth-abundant metal that is highly synergistic with Ni in bimetallic LDH systems. Fe enhances the OER performance by modifying the electronic structure of Ni, lowering the overpotential, and increasing the oxidation state flexibility. It also improves the structural stability of the LDH layers by forming a mixed-valence hydroxide network. Copper (Cu^{2+}) plays a dual role in this system. It contributes to enhanced electron transfer kinetics due to its high electrical conductivity and introduces additional redox-active sites beneficial for ethanol electrooxidation. Cu also aids in modulating the electronic environment of the catalyst, enabling improved catalytic selectivity and reaction kinetics, particularly in organic oxidation pathways. Magnesium (Mg^{2+}), while electrochemically inert, serves a crucial structural function. It promotes crystallinity, enhances thermal and structural stability, and maintains the integrity of the LDH lattice without competing for redox activity. Mg also improves the dispersion of active sites and contributes to the formation of ultrathin nanosheets with large electrochemically active surface areas. Indium (In^{3+}) is incorporated to introduce structural defects and modulate the surface acidity/basicity of the LDH. In^{3+} can disrupt the charge distribution and induce localized electronic heterogeneity, which can improve the adsorption of reactants and facilitate intermediate formation during EOR and OER. Its relatively large ionic radius also contributes to lattice distortion, increasing the number of reactive edge sites and enhancing catalytic activity. This combination of elements NiFeCuMgIn ensure a balance of conductivity

and high catalytic activity, and stability making them an ideal electrocatalyst for water splitting applications.

In this study, the optimization process focused on balancing the compositional complexity with structural stability, aiming to harness the synergistic effects of multi-metal incorporation while avoiding phase segregation. **Table 1** summarizes the optimization process of metal cation ratios during the synthesis of HE-LDHs. It outlines various compositions of metal precursors, synthesis conditions, and their corresponding outcomes. Eight different samples were synthesized using various combinations of Ni, Fe, Cu, Mg, and In salts, with a fixed hydrothermal treatment condition (primarily at 120 °C for 12 hours). The aim was to identify the appropriate composition and synthesis environment that would result in the formation of a well-defined LDH phase, as confirmed by XRD. In the first four samples, sodium hydroxide and/or sodium carbonate were used as the base to control pH and promote precipitation. However, these formulations failed to produce characteristic XRD peaks associated with the LDH structure. This absence of crystallographic signals indicated that no proper LDH formation occurred, suggesting that the chosen metal ratios or the synthetic environment were not favorable for stable phase development. Beginning with sample 5, the experimental approach was modified by introducing urea as a hydrolysis agent. Urea decomposes slowly under hydrothermal conditions, releasing OH^- ions gradually and thereby enabling a controlled increase in pH. This method supports homogeneous nucleation and growth of the LDH layers. The results showed noticeable improvement: sample 6 exhibited partial success, showing some evidence of NiFe LDH formation in the XRD results, although it was not completely satisfactory for the NiFeCuMgIn HE-LDH. The most significant breakthrough was achieved in sample 8, where the optimized metal ratio of Ni:Fe:Cu:Mg:In = 3:1:0.5:0.5:0.5 was used along with 10 mmol of urea. This formulation yielded clear and strong XRD reflections corresponding to an LDH structure. The success of this sample can be attributed to a more balanced cationic composition that supports the structural requirements of LDH layers and the effective role of urea in maintaining a stable environment for crystallization. Thus, sample 8 was identified as the optimal condition for synthesizing high-quality HE-LDH.

By combining these five metals in near-equimolar ratios, the resulting HE-LDH structure benefits from configurational entropy stabilization, which promotes the formation of a single-phase solid solution, suppresses phase separation, and enhances long-term structural integrity. This unique multi-metal synergy is expected to yield a catalyst with superior multifunctionality, enhanced conductivity, increased active site density, and improved durability across all three target reactions. Thus, the strategic selection of Ni, Fe, Cu, Mg, and In provides a rational foundation for the development of a high-performance trifunctional HE-LDH electrocatalyst.

Figure 6. Periodic table of elements, in which the elements that can form HELH are exhibited in red letters on the yellow background.[220]

Sample	Metal cation ratios Ni : Fe	Ni : Fe : Cu : Mg : In	Additives	Hydrothermal treatment	LDH structure formation
1	1 : 1	1 : 1 : 1 : 1 : 1	1 M NaOH (pH ≈ 10)	120 °C for 12 hr	✖
2	1 : 1	1 : 1 : 1 : 1 : 1	1 M NaOH (pH ≈ 10)	160 °C for 16 hr	✖
3	1 :1	1 : 1 : 1 : 1 : 1	1 M NaOH (pH ≈ 10) + 0.1 M Na_2CO_3	120 °C for 12 hr	✖
4	3 : 1	3 : 1 : 1 : 1 : 1	0.1 M NaOH (pH ≈ 10) + 0.1 M Na_2CO_3	120 °C for 12 hr	✖
5	3 : 1	3 : 1 : 1 : 1 : 1	0.1 M Na_2CO_3	120 °C for 12 hr	✖
6	3 : 1	3 : 1 : 1 : 1 : 1	4 mmol urea	120 °C for 12 hr	✔/✖
7	3 : 1	3 : 1 : 1 : 1 : 1	10 mmol urea	120 °C for 12 hr	✖
8	3 : 1	3 : 1 : 0.5 : 0.5 : 0.5	10 mmol urea	120 °C for 12 hr	✔

Table 1. Optimization of metal cation ratios during the synthesis of HE-LDHs.

3.2 UNDERSTANDING THE ROLE OF HE-LDHs IN IMPROVING CATALYTIC PERFORMANCE

The central objective of this research is to understand the role of HE-LDHs in enhancing the catalytic performance of LDHs across multiple electrochemical reactions. To investigate how the high-entropy design modulates the electronic structure, active site distribution, and synergistic interactions between metal constituents. This objective aims to correlate entropy-induced structural stability and surface reactivity with the observed electrocatalytic performance, using both experimental techniques and literature-supported interpretation.

HE-LDHs represent a transformative advancement in the design of next-generation electrocatalysts. Their unique ability to incorporate five or more metal cations into a single-phase layered structure enables the creation of highly tunable and synergistically enhanced catalytic systems. The improvement in catalytic performance observed in HE-LDHs arises primarily from the high configurational entropy, which stabilizes the multi-metal lattice and facilitates the formation of metastable phases with superior functional properties.

In the context of electrocatalysis, the incorporation of diverse metal species such as Ni, Fe, Cu, Mg, and In introduces heterogeneous active sites, each contributing differently to the catalytic processes. For example, Ni and Fe are particularly active for HER and OER, while Cu enhances ethanol electrooxidation through improved conductivity and organic substrate activation. Mg acts as a structural stabilizer, and In modulates surface reactivity by altering the electron density and introducing localized distortions. The synergistic interactions among these metals generate an optimized electronic environment that improves the binding energies of key intermediates, reduces activation barriers, and accelerates charge transfer kinetics across all three reactions: HER, OER, and EOR.

Furthermore, the high entropy effect leads to enhanced defect engineering, electronic heterogeneity, and structural robustness, all of which are critical for long-term catalytic durability and activity retention. The presence of multiple redox-active centers enables dynamic adaptation to varying electrochemical conditions, making HE-LDHs inherently more versatile than traditional binary or ternary catalysts. Their layered structure also supports interlayer ion diffusion, contributing to fast mass transport and increased electrochemically active surface area.

In summary, the superior catalytic performance of HE-LDHs stems from the entropy-driven stabilization of a multi-metallic framework, which enables optimized structural, electronic, and surface properties. Understanding this role is essential for the rational design and fine-tuning of multifunctional catalysts tailored for high-efficiency water splitting and ethanol electrooxidation applications.

3.3 EXPLORATION OF STRUCTURE-PROPERTY-PERFORMANCE RELATIONSHIPS

A critical objective of this research is to establish a detailed understanding of the relationship between the structural features (crystallinity, morphology, surface area), physicochemical properties (oxidation states, conductivity), and the electrochemical performance (overpotential, Tafel slope, EIS, and ECSA) of the synthesized HE-LDHs to uncover how variations in structural features and physicochemical characteristics directly influence their electrocatalytic behavior. Understanding these relationships is essential for the rational design and optimization of multifunctional electrocatalysts capable of efficiently driving HER, OER, and EOR. The unique structural complexity of HE-LDHs arising from the incorporation of multiple metal cations results in significant variations in crystal phase composition, lattice distortion, defect density, and interlayer spacing. These structural characteristics are closely tied to key functional properties, such as electrical conductivity, redox potential, surface charge distribution, and active site availability. By systematically analyzing the structure, morphology, layer thickness, elemental distributions, and surface chemistry of the synthesized HE-LDHs using techniques such as XRD, SEM, TEM, EDS, and XPS. Electrochemical techniques such as LSV, Tafel analysis, EIS, and CV will be employed to link structural and surface modifications with key performance metrics. This integrated investigation aims to build a comprehensive framework that connects material structure and composition with functional electrochemical behavior. Such insights are not only fundamental to optimizing catalyst design but also to advancing the broader field of high-entropy electrocatalysis, ultimately enabling the development of next-generation materials with superior efficiency, selectivity, and long-term operational stability.

3.4 INTEGRATION OF HER, OER, AND EOR WITHIN A SINGLE ELECTROCATALYTIC FRAMEWORK

To demonstrate the feasibility of using HE-LDHs as trifunctional catalysts in a single system, replacing the sluggish four-electron transfer of anodic OER with EOR to enhance overall water splitting efficiency. The objective is to show how this hybrid approach can reduce energy input, produce high-purity hydrogen, and enable value-added chemical production from ethanol oxidation. Developing anodic reactions with cell potential lower than OER is a promising way for fundamentally lowering the energy requirements for electrocatalytic H2 production. Such anode oxidation reactions have the additional benefit of producing value-added products from inexpensive industrial feedstocks or renewable biomass sources. The EOR is a key electrochemical process that occurs at the anode of direct ethanol fuel cells (DEFCs), where ethanol (C_2H_5OH) is oxidized to intermediate or final products such as acetaldehyde (CH_3CHO), acetic acid/acetate (CH_3COOH/CH_3COO^-), or ideally carbon dioxide (CO_2). This reaction is of particular importance for renewable energy technologies, especially due to ethanol's safety, availability, and ease of storage compared to hydrogen. For reactions of this kind, applying large positive potential would unavoidably result in uncontrolled OER, therefore applying moderate potential is necessary to achieve high Faradaic efficiency (FE) toward target products. To improve the four-electron transfer sluggish reaction kinetics of the OER, it can be replaced with

the oxidation of small molecules that have lower oxidation potential. This approach enables cost-effective H2 production from aqueous solutions containing organic waste, such as ethanol which can be easily produced by the food crops, plants, and forest residue.

The schematic shown in **Figure 7** illustrates a hybrid ethanol-assisted water electrolysis system, where ethanol electrooxidation occurs at the anode and hydrogen evolution takes place at the cathode. This integrated electrochemical setup enhances the efficiency of hydrogen production by replacing the conventional OER with the more thermodynamically favorable EOR. In this system, the anode serves as the site for ethanol (EtOH) oxidation, where ethanol reacts with water to produce carbonate ions (CO_3^{2-}), protons, and electrons. This process significantly lowers the overpotential typically associated with OER. Simultaneously, at the cathode, water molecules are reduced by the incoming electrons to generate molecular hydrogen (H_2), along with hydroxide ions. The complete oxidation of ethanol follows the reaction: $C_2H_5OH + 12OH^- \rightarrow 2CO_2 + 9H_2O + 12e^-$, but in alkaline media, CO_2 reacts with OH^-: $CO_2 + 2OH^- \rightarrow CO_3^{2-} + H_2O$. Then, in alkaline media, the complete oxidation of ethanol to CO_2 follows the reaction: $CH_3CH_2OH + 12OH^- \rightarrow 2CO_3^{2-} + 6H_2O + 12e^-$. However, though in practice, complete oxidation to CO_2 is rare due to the difficulty in breaking the C–C bond. The overall reaction enables the concurrent conversion of ethanol into value-added products while efficiently producing high-purity hydrogen. The schematic also shows the flow of electrons from the anode to the cathode via an external power supply, and the movement of products and reactants within the electrolyte medium. This hybrid strategy not only reduces energy consumption but also offers a sustainable approach for coupling hydrogen production with organic oxidation, making it highly promising for green energy technologies and biomass utilization.
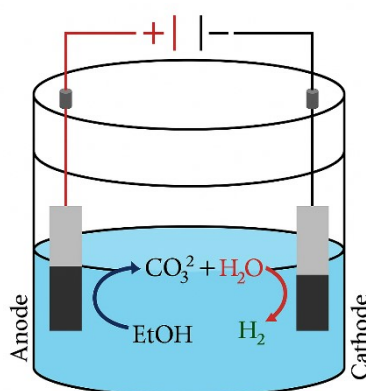
Figure 7. Schematic illustration of a hybrid ethanol-assisted water electrolysis system that combines EOR at the anode with HER at the cathode to improve energy efficiency and produce high-purity hydrogen.

CHAPTER 4. EXPERIMENTAL SECTION

4.1 MATERIALS AND REAGENTS

All chemicals and reagents used in this study were of analytical grade and utilized without further purification. Metal precursors, including nitrates or chlorides of transition metals such as nickel(II) nitrate hexahydrate ($Ni(NO_3)_2 \cdot 6H_2O$, ≥99%, MW = 290.81 g/mol), iron(III) nitrate nonahydrate ($Fe(NO_3)_3 \cdot 9H_2O$, MW = 404.00 g/mol), copper(II) nitrate trihydrate ($Cu(NO_3)_2 \cdot 3H_2O$, MW = 241.60 g/mol), magnesium(II) nitrate hexahydrate ($Mg(NO_3)_2 \cdot 6H_2O$, MW = 256.40 g/mol), and indium(III) chloride ($InCl_3$, MW = 221.18 g/mol) were selected to ensure compositional diversity in the synthesis of HE-LDHs. Urea ($CO(NH_2)_2$, MW = 60.06 g/mol) was employed as a slow-release base to facilitate homogeneous nucleation and growth of the LDH structure during hydrothermal synthesis. Ethanol and deionized water were used as solvents and for washing the final products. ammonium hydroxide solution, purists., 30-33% NH_3 in H_2O ($NH_3 . H_2O$, MW= 17.031 g/mol) was used for etching to further enhance catalytic efficiency. All solutions were prepared using high-purity deionized water.

4.2 SYNTHESIS OF HIGH ENTROPY ELECTROCATALYSTS

The HE-LDHs were synthesized via a hydrothermal treatment method shown in **Figure 8**. Four compositions with increasing cationic complexity were prepared systematically as follows: Initially, metal nitrate salts were dissolved in deionized water under continuous magnetic stirring at room temperature to obtain homogeneous precursor solutions. In the first formulation, 2.4 mmol of nickel (II) nitrate hexahydrate ($Ni (NO_3)_2 \cdot 6H_2O$) and 0.8 mmol of iron (III) nitrate nonahydrate ($Fe (NO_3)_3 \cdot 9H_2O$) were dissolved in 30 mL of deionized water. In the second sample, 0.4 mmol of copper (II) nitrate trihydrate ($Cu (NO_3)_2 \cdot 3H_2O$) was added to the NiFe system and dissolved in 30 mL of water. The third solution was prepared by adding 0.4 mmol of magnesium (II) nitrate hexahydrate ($Mg (NO_3)_2 \cdot 6H_2O$) to the previous mixture. Finally, the high-entropy composition was obtained by incorporating 0.4 mmol of indium (III) chloride ($InCl_3$) to the NiFeCuMg mixture. All salts were fully dissolved using a magnetic stirrer. Once homogeneity was achieved in each solution, 2.4 g of urea ($CO(NH_2)_2$) was added serving as a slow-releasing hydroxide source, was added in excess to control the pH and facilitate uniform precipitation of the metal hydroxide phases under continuous stirring at room temperature. The resulting mixtures were transferred into four separate 150 mL Teflon-lined stainless-steel autoclaves and subjected to hydrothermal treatment at 120 °C for 12 hours in a preheated oven.

After cooling to room temperature, the solid products were collected by centrifugation at 3000 rpm for 5 minutes. The precipitates were washed three times with distilled water and once over with ethanol to remove residual ions and organics. The final products were dried in the oven at 60 °C overnight and ground manually using a mortar to obtain uniform fine powders, which were then stored for further characterization and electrochemical testing. This synthesis route allows for compositional tunability, reproducibility, and scalability, making it suitable for

producing multifunctional HE-LDH electrocatalysts for HER, OER, and EOR applications.

To further enhance catalytic efficiency, the etching process was carried out using a two-step liquid-phase strategy as shown in **Figure 9**. 200 mg of HE-LDH was dissolved in 100 mL ethanol to produce solution A. Then, 50 mL $NH_3 \cdot H_2O$ and 200 mL DI water were mixing to obtain a solution B. Afterward, the solution B was directly poured into the solution A under stirring at room temperature. After continuous stirring for 10, 20, 30 and 60 minutes. The obtained mixed solution was filtered and washed with water many times, and the products were dried in the oven at 60 °C overnight to obtain et-HELDH product.
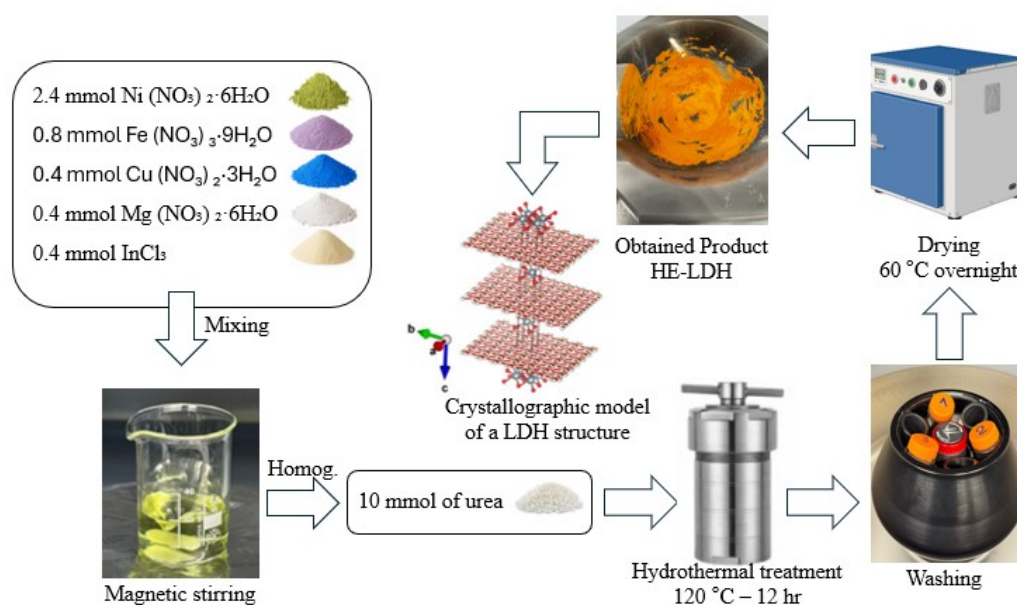
Figure 8. Schematic diagram of the synthesis process for HE-LDH.
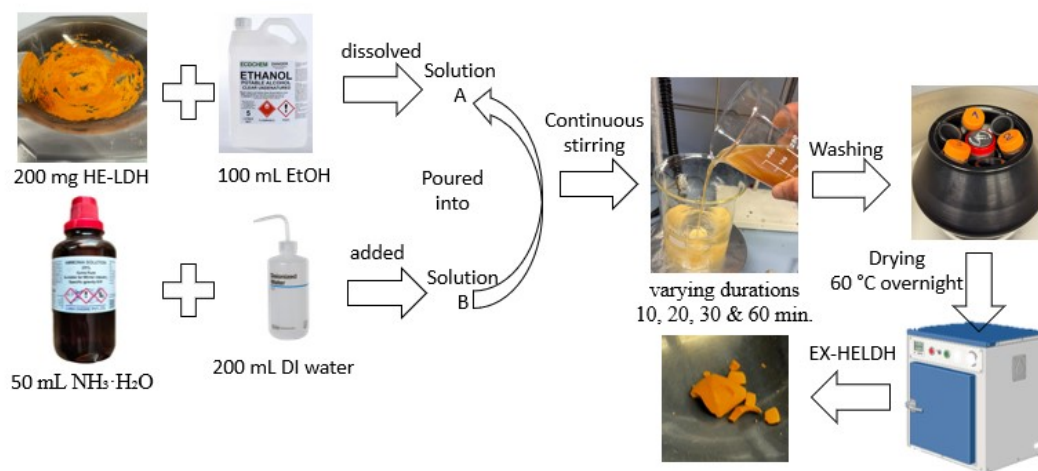
Figure 9. Schematic diagram of the etching process of the synthesized HE-LDH.

4.3 CHARACTERIZATION TECHNIQUES

4.3.1 MORPHOLOGICAL AND ELEMENTAL DISTRIBUTION ANALYSIS (SEM/EDS)

The surface morphology and elemental analysis for the synthesized materials were examined using SEM and EDS, respectively. SEM images were obtained under identical imaging conditions an accelerating voltage of 3.00 kV, a working distance (WD) of 5.8 mm, a beam current of 25 pA, and a Through-Lens Detector (TLD). The SEM micrographs of various synthesized layered double hydroxide (LDH) samples were captured at 50,000× magnification with a 1 μm scale bar. To estimate the elemental distribution, confirm the presence and chemical compositional analysis of the synthesized materials EDS analysis was performed.

As can be depicted in **Figure 10** (a), the SEM image for NiFe LDH shows a typical plate-like morphology with stacked, thin, and irregular nanosheets. This structure is characteristic of conventional LDHs, providing a high surface area ideal for catalytic applications.

Figure 10 (b), (c) & (d) display the elemental mapping of NiFe LDH using EDS analysis, which confirms the presence of the expected Ni, Fe and O constituent elements with the uniform distribution. As can be seen in **Figure S1, S5** (Supplementary data), NiFe LDH showing a uniform distribution of Ni and Fe, indicating successful synthesis of the binary LDH. The atomic percentages (At%) obtained from this analysis are as follows: O (77.9%), Ni (14.1%), and Fe (8.0%). The strong O peak at ~0.5 keV reflected the hydroxide-rich structure, while the Ni and Fe signals, observed at 0.85 keV (Ni L-line), 7.5–8.3 keV (Ni K-lines), 0.7 keV (Fe L-line), and 6.4 keV (Fe K-line), confirmed the incorporation of these metals as divalent and trivalent cations, respectively, within the brucite-like layers of the LDH framework.
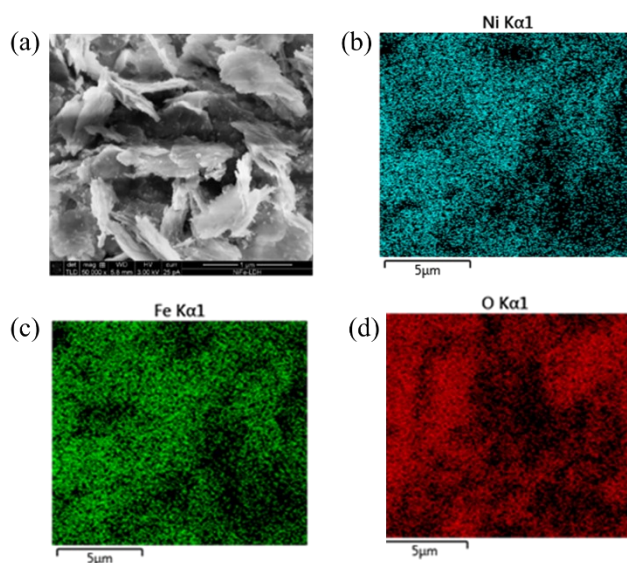
Figure 10. (a) SEM images for NiFe LDH. EDS mapping for NiFe LDH (b) Ni (c) Fe, and (d) O elements.

As can be depicted in **Figure 11** (a); after introducing copper, the morphology becomes slightly more aggregated, with sheets appearing thicker and partially crumpled, suggesting increased layer interaction and possible synergistic effects among the metals.

Figure 11 (b), (c), (d) & (e) display the elemental mapping of NiFeCu ME-LDH using EDS analysis, which confirms the presence of the expected Ni, Fe, Cu and O constituent elements with the uniform distribution. As can be seen in **Figure S2, S6** (Supplementary data), NiFeCu ME-LDH showing a uniform distribution of Ni, Fe, and Cu indicating successful synthesis of the ternary ME-LDH. The atomic percentages (At%) obtained from this analysis are as follows: O (77.6%), Ni (13.7%),Fe (8.2%), and Cu (0.5%).
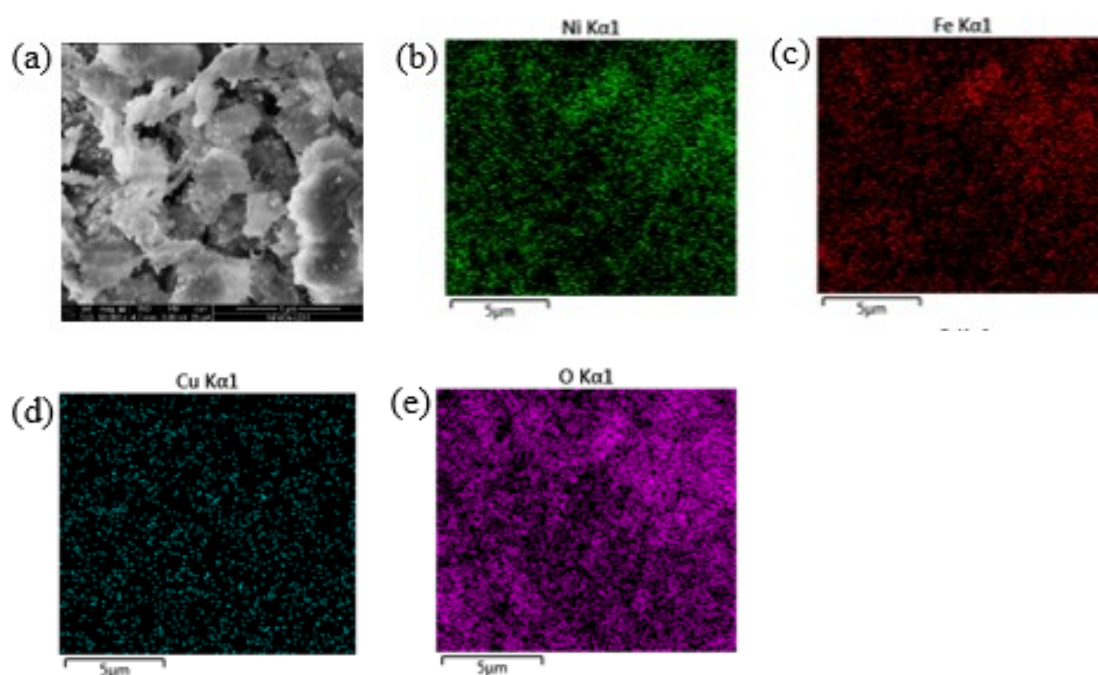
Figure 11. (a) SEM images for NiFeCu ME-LDH. EDS mapping for NiFeCu ME-LDH (b) Ni (c) Fe, and (d) Cu, and (e) O elements.

As can be depicted in **Figure 12** (a); after introducing magnesium, the surface becomes rougher and denser. Distinct microcrystalline structures are observed, likely enhancing active surface sites due to the presence of uniformly distributed Mg.

Figure 12 (b), (c), (d), (e) & (f) display the elemental mapping of NiFeCuMg ME-LDH using EDS analysis, which confirms the presence of the expected Ni, Fe, Cu, Mg and O constituent elements with the uniform distribution. As can be seen in **Figure S3, S7** (Supplementary data**)**, NiFeCuMg ME-LDH showing a uniform distribution of Ni, Fe, Cu, and Mg indicating successful synthesis of the quaternary ME-LDH. The atomic percentages (At%) obtained from this analysis are as follows: O (73.7%), Ni (12.4%), Fe (10.6%), Cu (0.8%), and Mg (2.6%). Compared to the previous sample, a slight decrease in oxygen content and corresponding increase in Fe indicates better elemental balance.

Figure 12. (a) SEM images for NiFeCuMg ME-LDH. EDS mapping for NiFeCuMg ME-LDH (b) Ni (c) Fe, and (d) Cu, (e) Mg, and (f) O elements.

As can be depicted in **Figure 13** (a); after introducing indium, the surface becomes in a more compact and flower-like morphology. The surface appears granulated with well-dispersed particles, indicating a HE-LDH with potentially improved structural stability and active site availability.

Figure 13 (b), (c), (d), (e), (f) & (g) display the elemental mapping of NiFeCuMgIn HE-LDH using EDS analysis, which confirms the presence of the expected Ni, Fe, Cu, Mg, In and O constituent elements with the uniform distribution. As can be seen in **Figure S4, S8** (Supplementary data), NiFeCuMgIn HE-LDH show a uniform distribution of Ni, Fe, Cu, Mg, and In indicating successful synthesis of the quinary HE-LDH. The maps reveal a more complex elemental profile, indicating successful multi-metal incorporation. The signals are evenly distributed, implying that all five metals were successfully co-integrated to form a HE-LDH. The atomic percentages (At%) obtained from this analysis are as follows: O (81.2%), Ni (10.8%), Fe (3.9%), Cu (0.5%), Mg (2.0%), and In (1.7%). The uniform presence of all intended elements suggests homogeneous distribution and stable incorporation within the layered lattice, with no evidence of phase separation or elemental segregation.
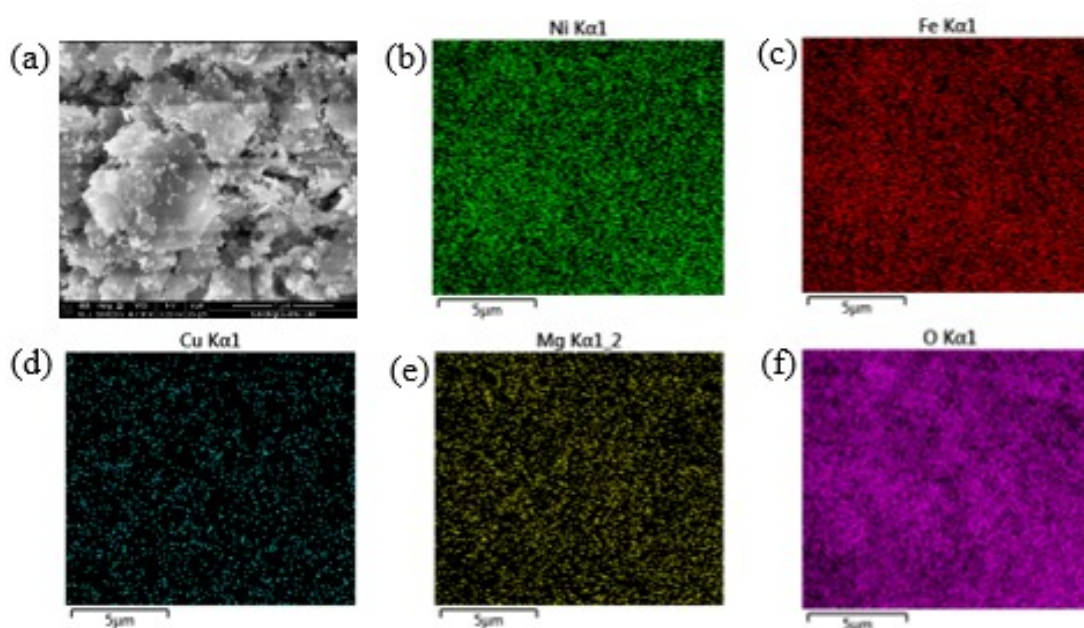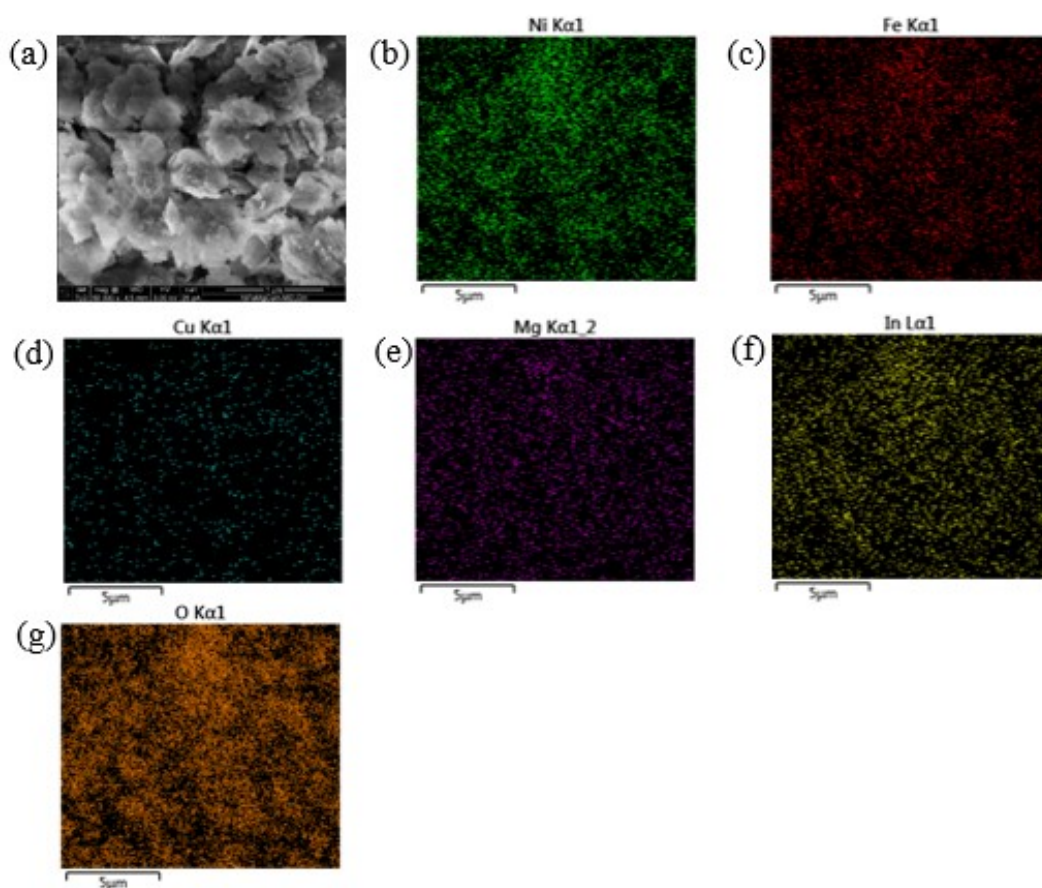

Figure 13. (a) SEM images for NiFeCuMgIn HE-LDH. EDS mapping for NiFeCuMgIn HE-LDH (b) Ni (c) Fe, and (d) Cu, (e) Mg, (f) In, and (g) O elements.

4.3.2 SURFACE CHEMISTRY (XPS)

To gain insight into the surface elemental composition and electronic states of the catalysts, XPS was employed as key analytical techniques. XPS was employed to analyze the elemental states and surface oxidation of each metal component. High-resolution spectra were recorded for Ni 2p, Fe 2p, Cu 2p, Mg 1s, In 3d, and O 1s regions to determine the oxidation states and quantify the relative contributions of each element at the catalyst surface. Peak deconvolution revealed the presence of mixed valence states (e.g., Ni^{2+}, Fe^{2+}/Fe^{3+}, Cu^{2+}, Mg^{2+}, In^{3+}), which are often associated with enhanced redox activity and catalytic performance. The O 1s spectrum provided insights into surface hydroxides, lattice oxygen, and adsorbed oxygen species, all of which are relevant to electrochemical reactivity. The C 1s spectrum in XPS primarily provides information on the types of carbon-containing species present on the surface of a material. Even when carbon is not intentionally included in the sample, it often appears due to adventitious carbon contamination from air exposure. However, it can also arise from carbon-based supports (e.g., carbon cloth), solvents, or surfactants.

Collectively, the XPS analysis provided comprehensive information on the surface chemistry, and elemental valency present in the HE-LDH catalysts, offering essential insights into their structure–reactivity relationships and catalytic behavior in HER, OER, and EOR.

4.4 ELECTROCHEMICAL ANALYSIS

The electrochemical performance of the synthesized HE-LDH electrocatalysts was systematically evaluated toward the HER, OER, and EOR in alkaline media. All measurements were conducted using a conventional three-electrode electrochemical cell. In the three-electrode setup, the catalytic samples were prepared, nickel foam coated with the catalyst ink served as the working electrode, while a carbon black-graphite composite (CB/Gr) was employed as the counter electrode, and an Ag/AgCl electrode was used as the reference electrode. The electrolyte was 0.5 M KOH for HER and OER, and a mixture of 0.5 M KOH with 1.0 M EtOH was used for EOR studies (Supplementary data S2).

Catalyst inks were prepared by dispersing 10 mg of the catalyst powders in a mixture of 750 μL of deionized (DI) water, 200 μL of 2-propanol, and 50 μL of 5% Nafion solution followed by ultrasonically mixing for 1 hour to ensure a homogeneous suspension. A proper amount of the resulting catalyst mixture was then loaded onto nickel foam by drop casting (The loading mass is approximately 1 mg cm^{-2}), followed by drying until the sample was completely dry as shown in **Figure 14**.

Figure 14. Electrode preparation for electrochemical measurements.

4.5 STABILITY AND DURABILITY TESTS

To evaluate the long-term operational reliability of the synthesized et-HELDH electrocatalyst, comprehensive stability and durability tests were conducted under continuous electrochemical conditions relevant to HER and EOR in alkaline media. The CA and CP measurements were performed to monitor current and potential stability, respectively, over extended durations for 100 hours, under constant applied potential or current densities corresponding to practical operating conditions. These tests were performed in 0.5 M KOH for HER, and in 0.5 M KOH containing 1.0 M EtOH for EOR, using a three-electrode setup. Catalyst-coated electrodes were subjected to sustained electrolysis while continuously recording electrochemical signals to detect any performance degradation. Post-stability structural analysis using XRD were also conducted to identify any shifts in the peaks, which would indicate catalytic deactivation. These stability and durability evaluations are critical for validating the robustness of HE-LDH catalysts and confirming their suitability for prolonged use in practical electrochemical devices. The results provide insights into catalyst lifetime, electrochemical resilience, and structural integrity under operational stress.

CHAPTER 5. RESULTS AND DISCUSSION

5.1 SYNTHESIS AND STRUCTURAL CHARACTERIZATIONS

5.1.1 X-RAY DIFFRACTION (XRD)

The NiFeCuMgIn HE-LDH electrocatalysts were successfully synthesized using a hydrothermal treatment method. The synthesis yielded fine powders with a characteristic layered morphology, indicative of the successful formation of the LDH structure. The crystalline structure and phase purity of the synthesized LDHs were investigated by XRD.

As shown in **Figure 15** (a). All the as-synthesized samples, including NiFe LDH, NiFeCu ME-LDH, NiFeCuMg ME-LDH, and NiFeCuMgIn HE-LDH, exhibit characteristic diffraction peaks corresponding to the LDH structure with an important 2θ shift. The observed reflections at $2\theta \approx 11.4°$, $22.9°$, $34.5°$, $38.7°$, $46.9°$, $60.8°$, and $62.1°$ can be indexed to the (003), (006), (012), (015), (018), (110), and (113) planes, respectively, in a good agreement with the standard hydrotalcite-like LDH phase (JCPDS no. 40-0215). No secondary phases or impurity peaks were appeared, suggesting the effective incorporation of all five metal cations into a single-phase solid solution and affirming the phase purity and crystallinity of the synthesized HE-LDHs. The retention of well-defined LDH peaks across all samples suggests that the introduction of multiple metal cations, including Cu, Mg, and In, does not disrupt the fundamental layered structure. Notably, a slight broadening and shift in peak positions is observed with increasing compositional complexity (from binary NiFe to quinary NiFeCuMgIn), which can be attributed to lattice distortion induced by the incorporation of multiple cations with varying ionic radii. This shift depicted from the enlarged in **Fig. 15** (b) further confirms the successful incorporation of the elements to the latice of NiFeLDH to the formation of high-entropy LDH phases, characterized by homogeneous distribution of metal species within the brucite-like layers. These results indicate that the high-entropy strategy effectively stabilizes the LDH structure while incorporating diverse metal species, paving the way for tunable electronic properties and enhanced catalytic activity.

Figure 15 (c) displays the XRD patterns of NiFeCuMgIn et-HELDH subjected to chemical etching for different durations (10, 20, 30, and 60 minutes), compared with the pristine (non-etched) HE-LDH sample. The preserved peak positions across all etched samples indicate that the LDH crystalline phase remains intact during the etching process. However, subtle variations in peak intensity and broadening are observed as etching time increases. Notably: After 10 and 20 minutes of etching, the peak intensities are slightly reduced, and peak broadening becomes more apparent, suggesting partial etching, reduced crystallite size, and increased structural disorder. Etching for 30 and 60 minutes leads to further intensity reduction, particularly in the (003) and (006) planes, indicating a progressive disruption of the long-range stacking order in the LDH layers. This is consistent with increased delamination or partial amorphization often reported in chemically etched LDHs.
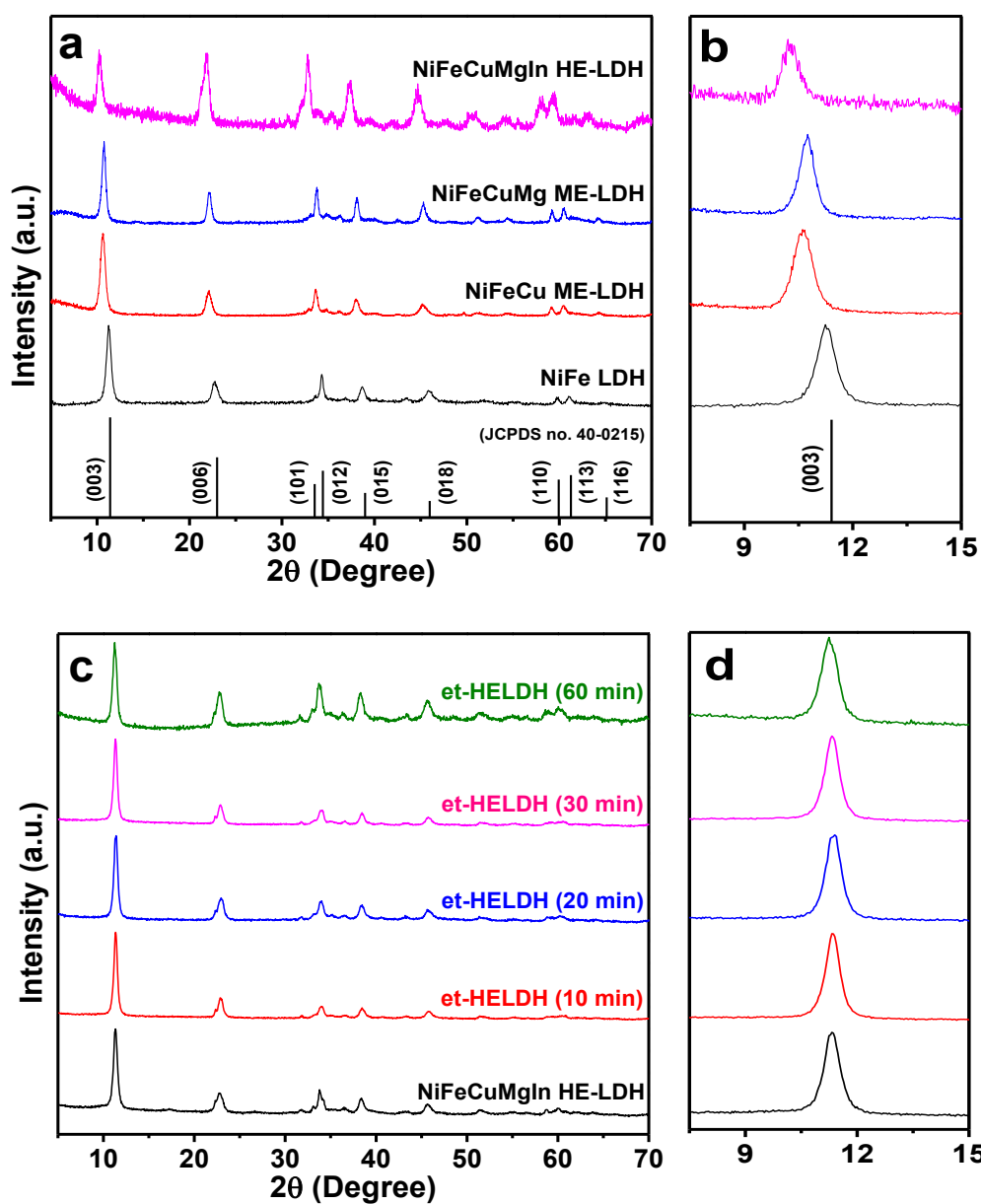
Figure 15. XRD pattern of all samples, **(a)** NiFe LDH, NiFeCu ME-LDH, NiFeCuMg ME-LDH, and NiFeCuMgIn HE-LDH, **(b)** Enlarged version of (003), **(c)** NiFeCuMgIn et-HELDH subject to variable chemical etching time (10, 20, 30, and 60 minutes), and **(d)** Enlarged version of (003).

5.1.2 X-RAY PHOTOELECTRON SPECTROSCOPY (XPS)

In **Figure 16**, the XPS spectra collected for four different samples; NiFe LDH, HE-LDH, et-HELDH, and et-HELDH post-stability, provide insight into the surface elemental composition and electronic states of the catalysts. All samples consistently show the coexistence presence of Ni, Fe, O, and C, with Cu, Mg, and In appearing in HE-LDH and etched samples. High-resolution core-level analysis further elaborates the chemical environments of key elements. The C 1s region displayed three deconvoluted peaks centered at ~284.8 eV (C–C/C–H, graphitic carbon), ~286.5 eV (C–O/C–OH), and ~288.8 eV (O–C=O), indicating various carbon bonding environments. The O 1s region revealed three distinct peaks: 529.4, 531.0, and 532.5 eV (**Figure 16** (e), (f), (g), and (h)). Those peaks are ascribed to oxygen atoms bound to metals (O1), defect sites (O2), and hydroxyl groups or adsorbed oxygen (O3), respectively.[221]

Ni 2p and Fe 2p peaks dominate, confirming these as primary metals in the catalyst. Cu, Mg, and In show lower atomic concentrations due to their lower molar ratio in synthesis. The Ni 2p peaks at 855.7-857.3 eV confirm Ni species exists in the form of Ni^{2+}. The Fe 2p peaks at 711.1-711.9 eV confirm Fe species exists in the form of Fe^{3+}. The Cu 2p peaks at 933.5-933.6 eV confirm Cu species exists in the form of Cu^{2+}. The In 3d peaks at 444.5–446.3 eV confirm In species exists in the form of In^{3+} (**Figure S9, S10, S11, S12**) (Supplementary data). Post-Stability Sample, Detected additional F 1s (689.4 eV) and N 1s (398–400 eV) possibly due to: electrolyte contamination or residuals from long-term testing. Fe signal dropped significantly, suggesting leaching or surface restructuring. O 1s peak shift and distribution changes indicate modifications in surface oxygen species after long-term operation. Ni, Cu, In maintained surface presence, indicating better stability compared to Fe.

These XPS findings validate the successful incorporation of multiple metal species (Ni, Fe, Cu, Mg, In) into the LDH framework and their chemical stability post-exfoliation and operation. The enhancement in electrochemical performance correlates well with: Increased surface hydroxyls (favorable for catalytic activity), strong metal-oxygen bonding, retained oxidation states, modest surface composition changes after durability testing.
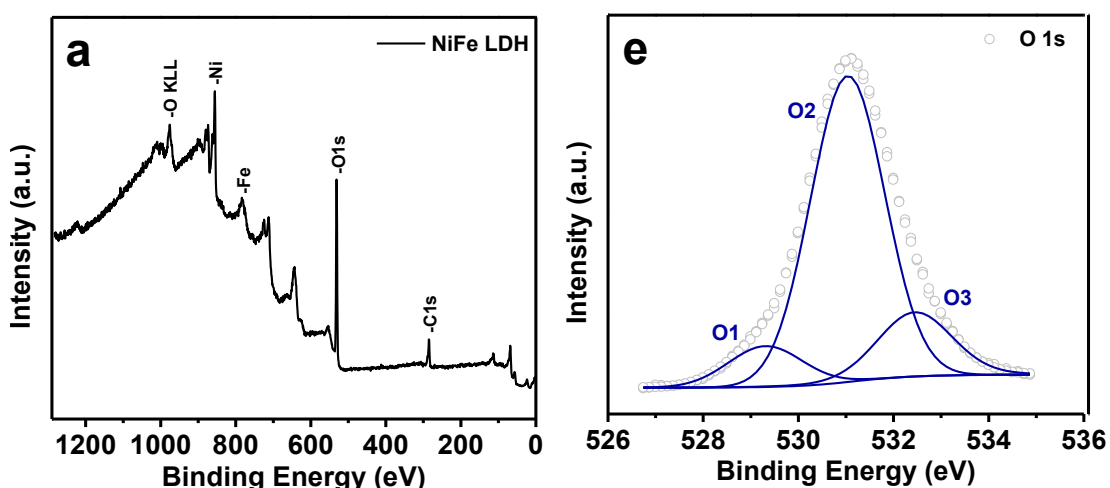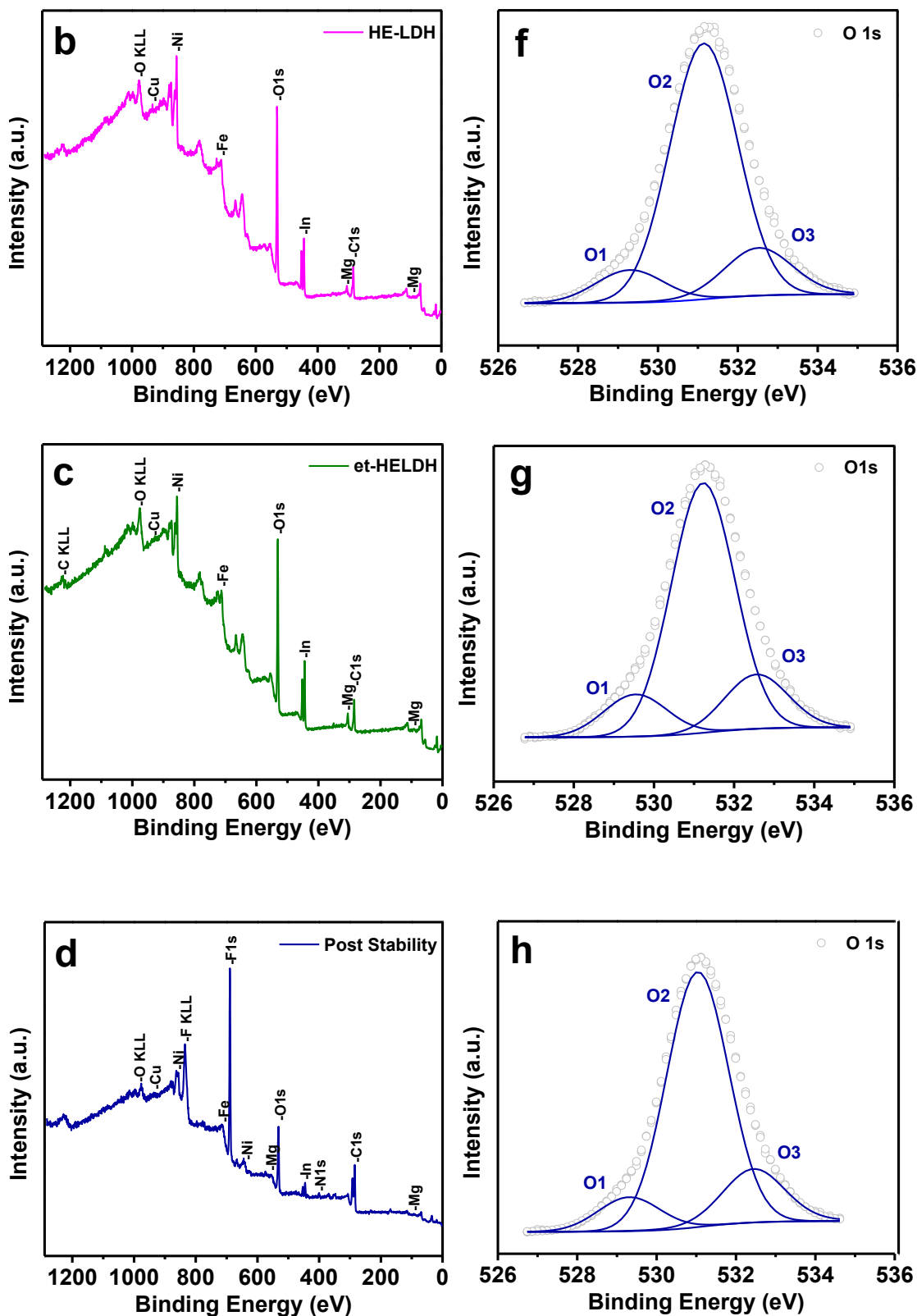
Figure 16. XPS spectrum of, (a) NiFe LDH, (b) HE-LDH, (c) et-HELDH, (d) et-HELDH post stability, (e) XPS spectrum of the O element of NiFe LDH, (f) XPS spectrum of the O element of HE-LDH, (g) XPS spectrum of the O element of et-HELDH, and (h) XPS spectrum of the O element of et- HELDH post stability.

5.2 ELECTROCATALYTIC PERFORMANCE

5.2.1 LINEAR SWEEP VOLTAMMETRY (LSV) - HER

The electrocatalytic activity of the synthesized catalysts toward the HER was assessed using LSV in 0.5 M KOH solution at a scan rate of 10 mV/s versus the RHE. The results for various catalyst compositions were conducted at current density of $50 \, mA/cm^2$.

Figure 17 (a) compares the HER polarization curves of four samples: NiFe-LDH, NiFeCu ME-LDH, NiFeCuMg ME-LDH, and NiFeCuMgIn HE-LDH. A clear improvement in HER activity is observed with increasing compositional complexity. The overpotential decreased from 507 mV for NiFe-LDH to 444 mV for NiFeCu ME-LDH, and further to 386 mV for NiFeCuMg ME-LDH. The best performance among these was achieved by the NiFeCuMgIn HE-LDH, which exhibited a significantly reduced overpotential of 321 mV. This progressive enhancement can be attributed to the synergistic effects arising from the incorporation of multiple metal cations, which improve charge transfer characteristics, increase active site density, and modulate the electronic structure of the catalyst.

To further improve catalytic performance of the synthesized HE-LDH, the etching process was carried out using a two-step liquid-phase for varying etching times: 10, 20, 30, and 60 minutes. As shown in **Figure 17** (b), the etched samples showed a further reduction in overpotential, with the 20-minute etched sample demonstrating the most optimal HER activity. The overpotential was reduced from 321 mV for HE-LDH to 187 mV after 20 minutes etching. However, beyond this duration, performance began to slightly deteriorate, with overpotentials increasing to 387 mV for 60-minute etched sample. The initial improvement is attributed to the enhanced electrochemical surface area, increased exposure of catalytically active sites, and better electron transport resulting from the thinner, delaminated structure. On the other hand, extended etching times may lead to nanosheet restacking or structural degradation, which could reduce the accessibility of active sites.

In summary, both high-entropy engineering and controlled etching significantly improve the HER catalytic activity. The HE-LDH demonstrated superior activity compared to binary and medium-entropy analogs, and the 20-minute et-HELDH achieved the best overall performance, making it a highly promising candidate for efficient alkaline hydrogen production.

Figure 17. (a) LSV polarization curves showing HER performance of NiFe-LDH, NiFeCu ME-LDH, NiFeCuMg ME-LDH, and NiFeCuMgIn HE-LDH, (b) HER activity comparison of HE-LDH and et-HE-LDH samples at different etching times (10, 20, 30, and 60 minutes), showing best performance for the 20-minute etched sample.

5.2.2 TAFEL PLOTS - HER

To further investigate the kinetic behavior of HER, Tafel plots were derived from the LSV data. The results for various catalyst compositions are illustrated in **Figure 18** (a), while the impact of etching on the HE-LDH is shown in **Figure 18** (b).

As presented in **Figure 18 (a)**, the Tafel slope for NiFe-LDH was 266.61 mV/dec, indicating slow kinetics and high energy barriers for HER. The introduction of Cu into the LDH structure improved the kinetics slightly, as reflected in the Tafel slope of 226.82 mV/dec for NiFeCu ME-LDH. Further addition of Mg resulted in a more pronounced enhancement, lowering the slope to 194.74 mV/dec for NiFeCuMg ME-LDH. The NiFeCuMgIn HE-LDH, which incorporates a high-entropy composition, exhibited the lowest Tafel slope of 145.52 mV/dec among all the non-etched samples. This improvement underscores the synergistic effects among multiple metal cations, which optimize hydrogen adsorption, promote electron transfer, and create a favorable catalytic environment for HER in alkaline media.

Figure 18 (b) compares the Tafel slopes of HE-LDH and et-HELDH to assess the impact of etching on reaction kinetics. The etched sample showed a slightly lower Tafel slope of 136.69 mV/dec, compared to 145.52 mV/dec for the HE-LDH. This reduction confirms that etching not only increases the electrochemical surface area but also enhances the availability of active sites and the accessibility of electrons and protons, resulting in faster reaction kinetics.

In conclusion, Lower Tafel slopes indicate faster kinetics and more efficient electron transfer. The HE-LDH and et-HELDH catalysts demonstrate excellent reaction kinetics. Tafel slope analysis aligns with the LSV results, demonstrating that both high-entropy composition and controlled etching significantly improve HER kinetics. The combination of these two strategies enables the development of highly efficient, noble-metal-free electrocatalysts suitable for practical hydrogen production.
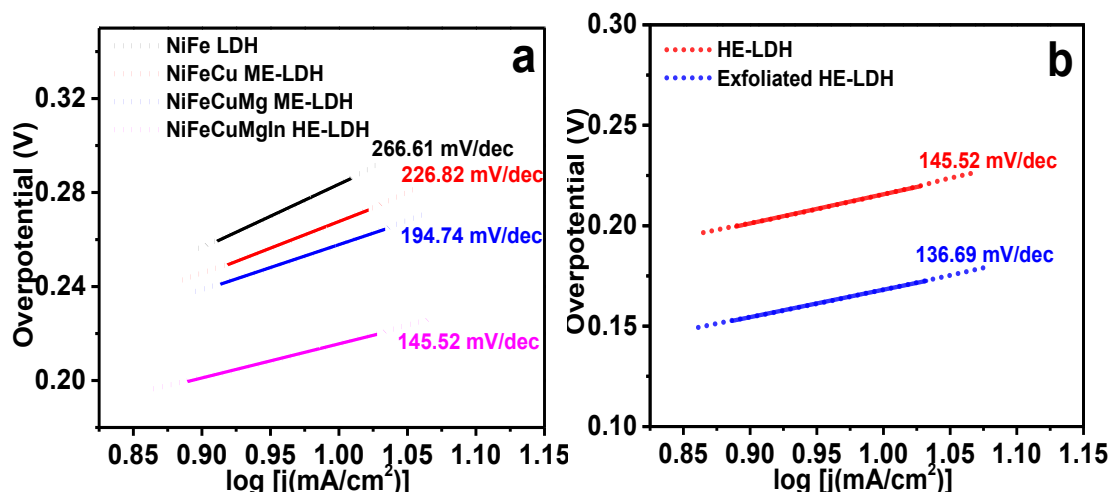
Figure 18. (a) Tafel plots for HER showing the improved reaction kinetics with increasing compositional complexity: NiFe-LDH, NiFeCu ME-LDH, NiFeCuMg ME-LDH, and NiFeCuMgIn HE-LDH, (b) Comparison of Tafel slopes for HE-LDH and et-HELDH , illustrating the kinetic advantage gained from etching.

5.2.3 LINEAR SWEEP VOLTAMMETRY (LSV) - OER

The electrocatalytic activity of the synthesized catalysts toward the OER was assessed using LSV in 0.5 M KOH solution at a scan rate of 10 mV/s versus the RHE. The results for various catalyst compositions were conducted at current density of 10 mA/cm².

Figure 19 (a) compares the OER polarization curves of four samples: NiFe-LDH, NiFeCu ME-LDH , NiFeCuMg ME-LDH, and NiFeCuMgIn HE-LDH. A clear improvement in OER activity is observed with increasing compositional complexity. The overpotential required decreased from 169 mV for NiFe-LDH to 158 mV for NiFeCu ME-LDH, and further to 153 mV for NiFeCuMg ME-LDH. The best performance among these was achieved by the NiFeCuMgIn HE-LDH, which exhibited a significantly reduced overpotential of 150 mV

As shown in **Figure 19** (b), the 20-min et-HELDH outperformed the HE-LDH, reducing the overpotential to 143 mV. This enhancement is a result of increased surface area, improved exposure of active sites, and better charge transport facilitating more efficient reaction pathways.

In summary, both high entropy composition and controlling etching significantly improve OER catalytic activity. The NiFeCuMgIn et-HELDH catalyst demonstrates the most promising performance, with a substantially reduced overpotential and enhanced current response. These results underscore the potential of entropy-engineered and nanostructured LDH catalysts for use in efficient and sustainable alkaline water electrolysis systems.

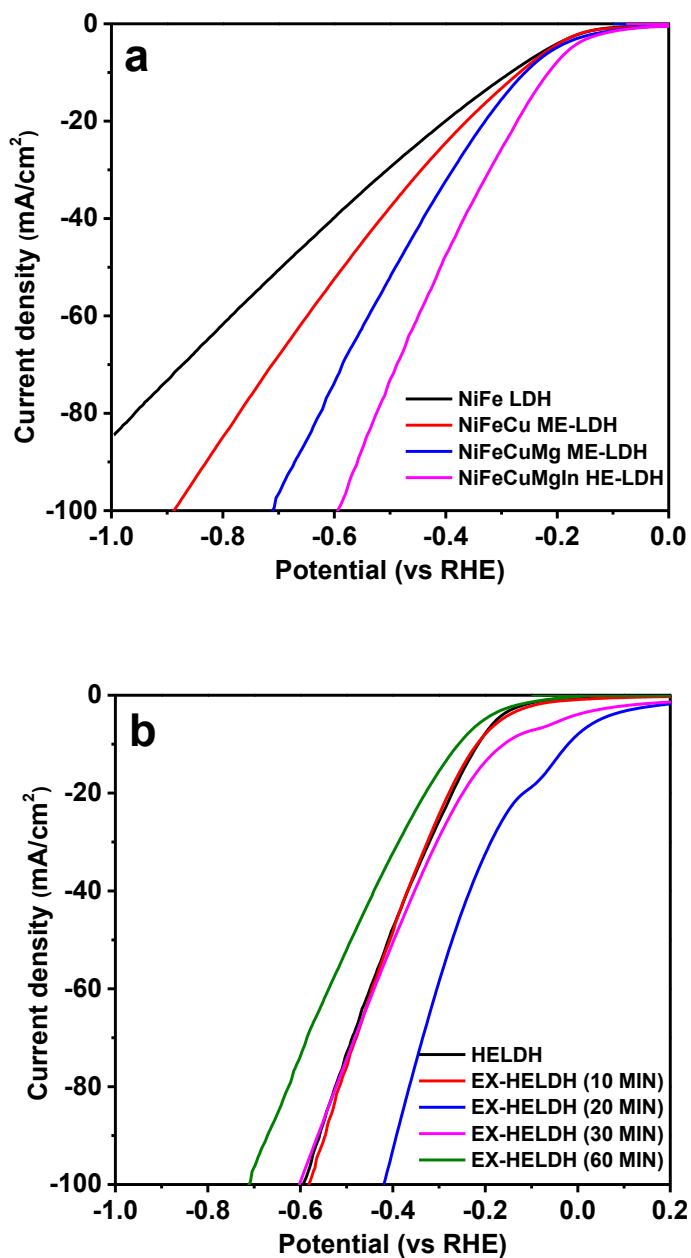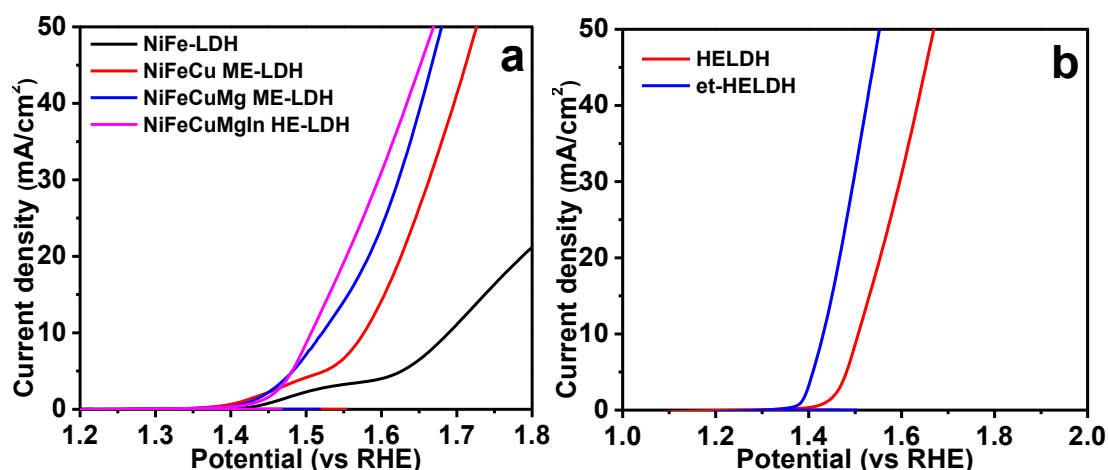**Figure 19.** (a) LSV polarization curves showing OER performance of NiFe-LDH, NiFeCu ME-, NiFeCuMg ME-LDH, and NiFeCuMgIn HE-LDH, (b) Comparison of OER performance between HE-LDH and et-HELDH, highlighting performance enhancement after etching.

5.2.4 TAFEL PLOTS - OER

To further investigate the kinetic behavior of the OER, Tafel plots were derived from the LSV data. The results for various catalyst compositions are illustrated in **Figure 20** (a), while the impact of etching on the HE-LDH is shown in **Figure 20** (b).

As shown in **Figure 20** (a), the Tafel slopes for NiFe-LDH, NiFeCu ME-LDH, NiFeCuMg ME-LDH, and NiFeCuMgIn HE-LDH were found to be 226.64 mV/dec, 161.74 mV/dec, 146.45 mV/dec, and 102.03 mV/dec, respectively. The progressive decrease in Tafel slope clearly reflects the enhanced OER kinetics with the incorporation of additional metal elements, attributed to increased active site availability, modified electronic structure, and synergistic interactions among the constituent metals.

Figure 20 (b) compares the Tafel slopes of HE-LDH and et-HELDH. The etched sample exhibited a significantly reduced Tafel slope of 87.98 mV/dec, compared to 102.03 mV/dec for HE-LDH. This improvement highlights the beneficial effect of etching, which enhances mass transport and facilitates better exposure of active catalytic sites by increasing surface area and reducing the diffusion pathway for ions.

In conclusion, the Tafel analysis supports the findings from LSV data, confirming that both high-entropy design and etching contribute significantly to the improved OER performance by accelerating reaction kinetics and lowering the activation energy barrier.
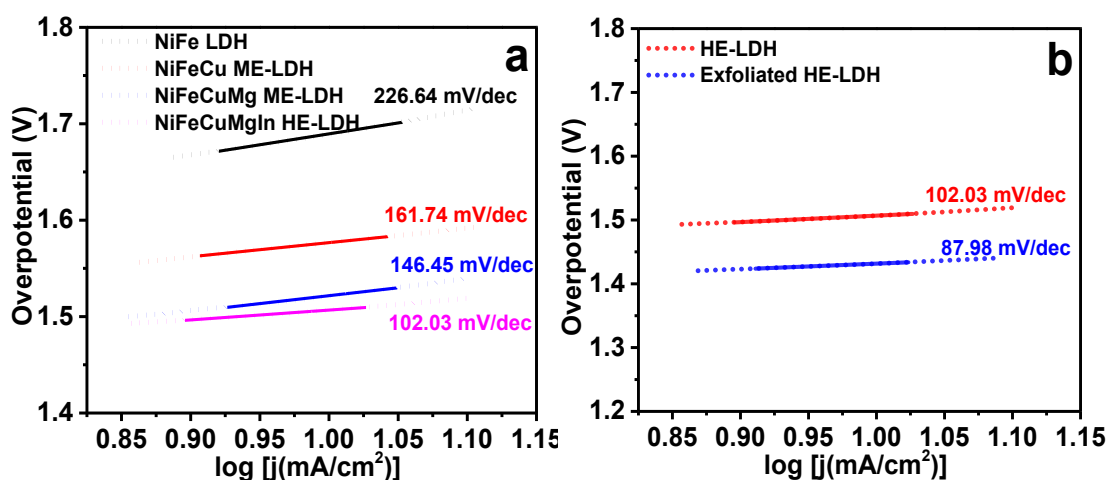
Figure 20. (a) Tafel plots for NiFe-LDH, NiFeCu ME-LDH, NiFeCuMg ME-LDH, and NiFeCuMgIn HE-LDH, showing progressive improvement in OER kinetics., (b) Comparison of Tafel slopes between HE-LDH and et-HELDH, indicating enhanced kinetic performance after etching.

5.2.5 ELECTROCHEMICAL IMPEDANCE SPECTROSCOPY (EIS) – HER & OER

EIS was employed to gain further insight into the interfacial charge transfer behavior and electrochemical conductivity of the synthesized LDH catalysts during HER and OER. Nyquist plots obtained from EIS measurements for various catalyst compositions are presented in **Figure 21**, where the semicircular regions reflect the charge transfer resistance (R_{ct}) at the catalyst electrolyte interface.

The NiFe-LDH exhibits the largest semicircle, corresponding to the highest R_{ct} value of approximately 160 Ω, indicating poor electrical conductivity and sluggish charge transfer kinetics. With the incorporation of additional metal elements, the charge transfer resistance is significantly reduced. The R_{ct} values for NiFeCu ME-LDH, NiFeCuMg ME-LDH, and NiFeCuMgIn HE-LDH were found to be approximately 110 Ω, 85 Ω, and 65 Ω, respectively. The progressive reduction in resistance with increasing compositional complexity highlights the impact of high-entropy design in facilitating charge transport and improving catalytic activity.

The most pronounced improvement is observed for the et-HELDH, which exhibits the smallest semicircle with an R_{ct} value of only 25 Ω. This dramatic reduction in resistance confirms that etching further enhances electrochemical performance by increasing the surface area, improving the exposure of active sites, and shortening the electron diffusion path through thinner, more conductive nanosheets.

These findings strongly agree with the LSV and Tafel results discussed earlier. The decrease in R_{ct} across the series correlates directly with the observed improvement in HER and OER activity, reinforcing the conclusion that both compositional tuning via high entropy alloying and structural optimization via etching are effective strategies to enhance electrocatalyst efficiency.
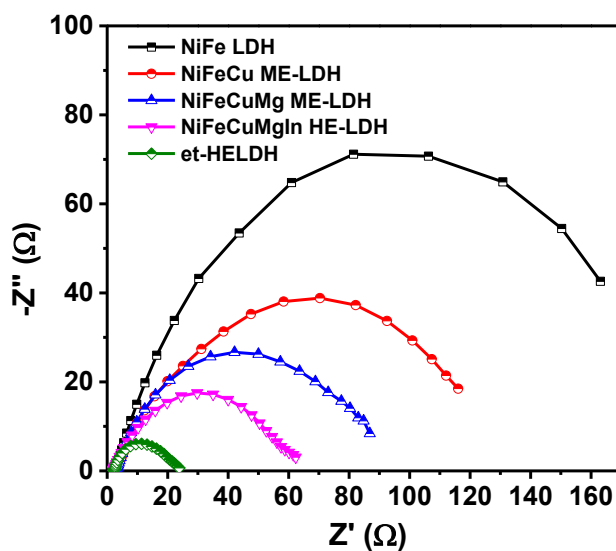
Figure 21. Nyquist plots from EIS showing the charge transfer resistance of NiFe-LDH, NiFeCu ME-LDH, NiFeCuMg ME-LDH, NiFeCuMgIn HE-LDH, and et-HELDH.

5.2.6 ELECTROCHEMICAL ACTIVE SURFACE AREA (ECSA) – HER & OER

CV was performed to estimate the ECSA of the synthesized LDH catalysts, which directly correlates with the number of accessible catalytic sites. The ECSA was evaluated by measuring the double-layer capacitance (C_{dl}) from CV curves obtained at various scan rates in a non-faradaic region **(Figure S12)** (Supplementary data). The relationship between current density and scan rate for each catalyst, with the slope of each linear fit corresponding to the C_{dl} value is plotted in **Figure 22**.

The NiFe-LDH sample showed the lowest C_{dl} of 0.079 mF/cm² , indicating a relatively small electroactive surface area. With the addition of Cu, the C_{dl} slightly increased to 0.085 mF/cm² for NiFeCu ME-LDH. The incorporation of Mg further improved this to 0.11 mF/cm² in the NiFeCuMg ME-LDH sample. A substantial increase was observed for the NiFeCuMgIn HE-LDH, which achieved a C_{dl} of 0.21 mF/cm² , highlighting the positive impact of entropy-driven compositional complexity in increasing accessible active sites.

The most significant enhancement was obtained with the et-HELDH, which exhibited the highest C_{dl} value of 0.32 mF/cm² . This enhancement compared to HE-LDH is attributed to the successful etching process, which delaminates the layered structure, reduces thickness, and exposes a larger number of surface-active regions to the electrolyte. As a result, the et-HELDH catalyst possesses more readily available active sites for charge transfer and reactant adsorption during both HER and OER processes.

Overall, the CV-derived C_{dl} results reinforce the earlier LSV, Tafel, and EIS findings, confirming that both HE-LDH and et-HELDH play key roles in enhancing electrocatalytic efficiency. The improvements observed at ECSA correlate strongly with the superior performance of the et-HELDH catalyst, further validating its potential for advanced energy conversion applications.
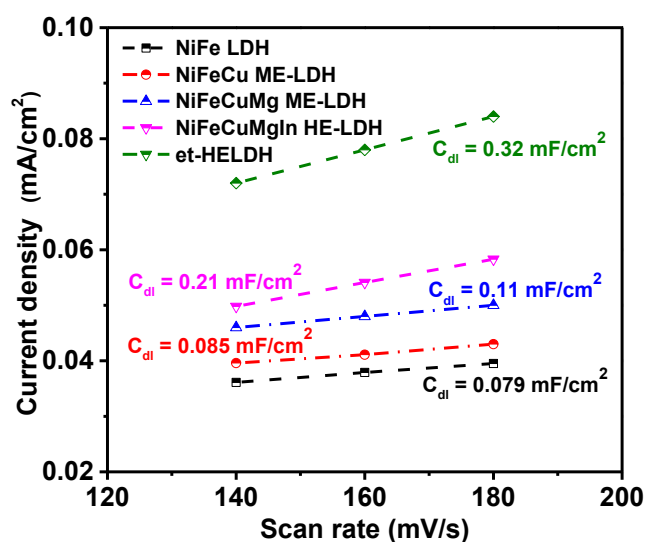
Figure 22. C_{dl} values of NiFe-LDH, NiFeCu ME-LDH, NiFeCuMg ME-LDH, NiFeCuMgIn HE-LDH, and et-HELDH.

5.2.7 LINEAR SWEEP VOLTAMMETRY (LSV) - EOR

The EOR performance of the synthesized HE-LDH catalysts was evaluated in a mixed electrolyte solution containing 1 M ethanol and 0.5 M KOH at a scan rate of 10 mV/s versus the RHE. The results for various catalyst compositions were conducted at current density of 10 mA/cm².

Figure 23 compares the EOR polarization curves of two samples HE-LDH and et-HELDH. The et-HELDH exhibits a significantly improved EOR performance compared to the HE-LDH. The overpotential was reduced from 148 mV for HE-LDH to 143 mV for et-HELDH, demonstrating enhanced catalytic activity upon etching. This performance enhancement is attributed to the structural advantages provided by etching. The process increases the electrochemically active surface area, promotes better dispersion of active sites, and facilitates faster charge and mass transport. These factors collectively result in improved ethanol oxidation kinetics and greater utilization of the catalyst surface. In summary, the LSV analysis confirms that etching significantly enhances the EOR activity of HE-LDH catalysts
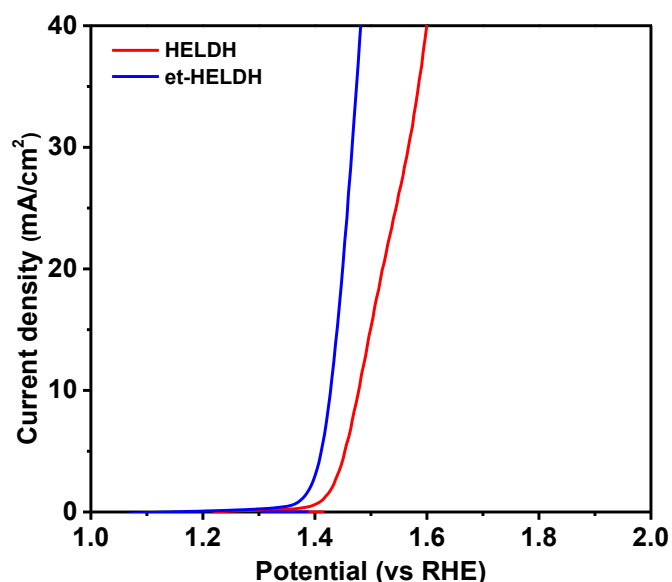
Figure 23. LSV polarization curves for EOR performance of HE-LDH and et-HELDH, highlighting performance enhancement after etching.

5.2.8 TAFEL PLOTS - EOR

To further assess the kinetics of ethanol electrooxidation, Tafel slope analysis was carried out for both HE-LDH and et-HELDH catalysts as shown in **Figure 24**. Tafel plots were derived from the LSV data.

The et-HELDH exhibited a markedly lower Tafel slope of 56.83 mV/dec, compared to 100.01 mV/dec for the HE-LDH. This significant reduction in Tafel slope confirms that etching enhances the intrinsic catalytic kinetics of the material, allowing faster charge transfer and more efficient ethanol oxidation.

The improvement is attributed to the increased accessibility of active sites and shortened electron diffusion paths in the etched sample. The higher surface area and better exposure of edge and basal planes achieved through etching reduce the energy barriers associated with intermediate formation during the EOR process.

Overall, the Tafel slope analysis aligns with the LSV findings, reinforcing the conclusion that et-HELDH offers superior ethanol oxidation kinetics. This enhancement makes et-HELDH a highly promising and efficient electrocatalyst for integrated energy conversion technologies involving alcohol fuels.
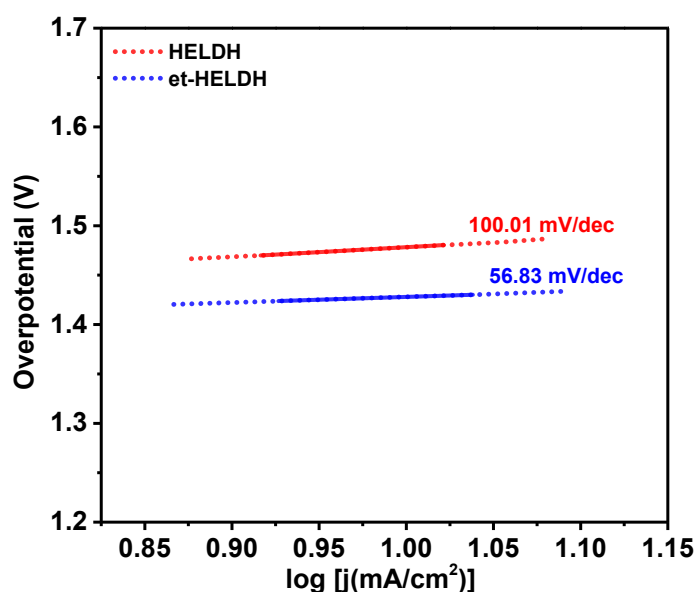
Figure 24. Tafel plots for NiFeCuMgIn HE-LDH and et-HELDH, indicating enhanced kinetic performance after etching.

5.2.9 ELECTROCHEMICAL IMPEDANCE SPECTROSCOPY (EIS) - EOR

EIS was conducted to further investigate the interfacial charge transfer resistance associated with the EOR for both HE-LDH and EXHELDH. The Nyquist plots obtained from EIS measurements are shown in **Figure 25**, where the diameter of the semicircle reflects the magnitude of the charge transfer resistance (R_{ct}) at the catalyst electrolyte interface.

The HE-LDH (red curve) exhibits a significantly larger semicircle with a high R_{ct} of approximately 125 Ω, indicating slower electron transfer and less efficient catalytic performance. In contrast, the et-HELDH (blue curve) displays a much smaller semicircle, corresponding to a greatly reduced R_{ct} of about 40 Ω. This substantial decrease in resistance demonstrates that etching dramatically improves the electronic conductivity and interfacial kinetics of the catalyst during ethanol oxidation.

The reduced charge transfer resistance in the etched sample is attributed to its expanded surface area, better exposure of active sites, and thinner nanosheet morphology, all of which contribute to more efficient mass and electron transport. These features lower the energetic barriers for charge transfer processes and enhance the overall electrocatalytic performance.

In summary, the EIS results strongly support the earlier LSV and Tafel analyses, confirming that et-HELDH provides a more favourable interfacial environment for EOR. The significant drop in R_{ct} demonstrates the effectiveness of etching as a strategy for boosting catalytic efficiency and highlights the potential of et-HELDH as a robust anodic material for ethanol-assisted energy conversion systems.
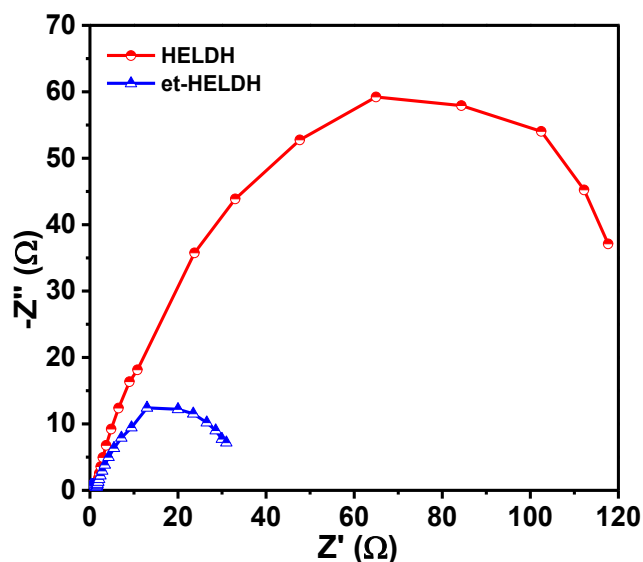
Figure 25. Nyquist plots showing the charge transfer resistance of HE-LDH and et-HELDH during ethanol electrooxidation, illustrating improved interfacial conductivity after etching.

5.2.10 ELECTROCHEMICAL ACTIVE SURFACE AREA (ECSA) - EOR

CV was conducted in the non-faradaic potential region to estimate the ECSA of both HE-LDH and et-HELDH during the EOR **(Figure S13)** (Supplementary data).

As shown in **Figure 26**, the calculated C_{dl} values reveal that et-HELDH exhibits a slightly higher electrochemical surface area than HE-LDH. Specifically, the C_{dl} of et-HELDH was found to be 0.04 mF/cm², compared to 0.02 mF/cm² for HE-LDH. While these values are relatively low, likely due to the partial blocking of active sites by ethanol intermediates during measurement they still indicate improved accessibility and electrochemical responsiveness in the etched material.

The higher C_{dl} of et-HELDH suggests that etching enhances the effective surface area available for catalysis, contributing to its superior performance in EOR, as demonstrated by earlier LSV, Tafel, and EIS results. The structural delamination achieved through etching likely improves electrolyte penetration and charge distribution, both of which are crucial for multi-step oxidation reactions such as EOR.

In conclusion, the CV analysis further confirms that et-HELDH possesses a larger electroactive surface and greater catalytic potential compared to the non-etched sample. These findings reinforce the value of etching as a structural engineering approach for improving the efficiency of high-entropy catalysts in alcohol electrooxidation applications.
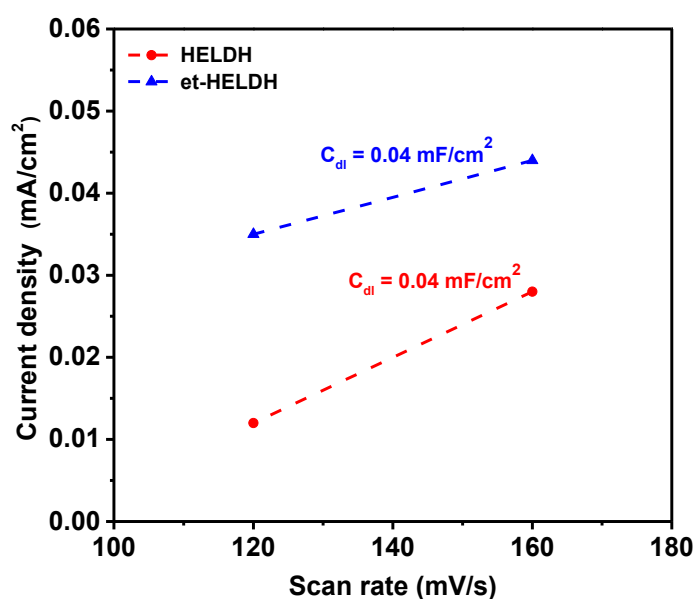
Figure 26. C_{dl} values of HE-LDH and et-HELDH, indicative of increased electrochemical surface area during EOR.

Figure 27 illustrates the long-term electrochemical stability of the et-HELDH catalyst via chronoamperometric measurements conducted over a continuous 100 hours under constant current conditions. The test was performed for both HER and EOR.

The black line, representing HER, shows no obvious deterioration, indicating excellent catalytic stability under prolonged reductive conditions. The red line, corresponding to EOR, remains constant throughout the duration of the test, demonstrating strong oxidative stability and structural integrity of the catalyst. This highlights the strong structural and chemical stability of the etched catalyst, even in the more complex and aggressive environment posed by organic molecule oxidation, making it a promising candidate for long-term operation in integrated water splitting and alcohol electrooxidation systems. These findings reinforce the practical potential of entropy-engineered and etched LDH materials for real-world clean energy applications.
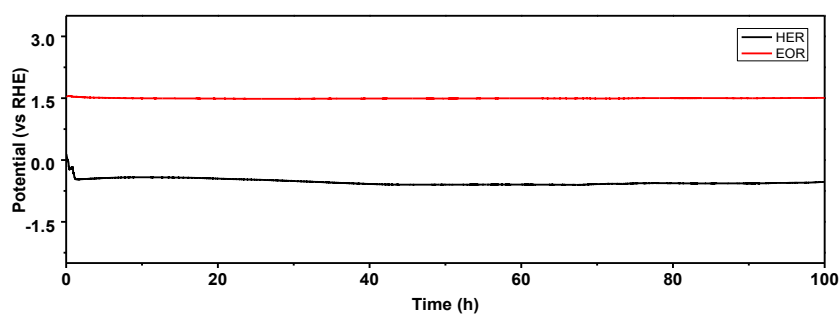
Figure 27. Chronopotentiometry curve of the et-HELDH for HER (black), and for EOR (red).

5.4 POST-STABILITY STRUCTURAL ANALYSIS

To assess the structural stability of the et-HELDH catalyst after extended electrochemical operation, XRD analysis was performed before and after the 100-hour stability test. The resulting diffraction patterns are presented in **Figure 28**, where the black curve corresponds to the sample before stability testing, and the red curve corresponds to the same sample after durability assessment.

Before the test, the catalyst exhibits sharp and well-defined diffraction peaks at $2\theta \approx 11.4°$, $22.9°$, and $34.5°$, assigned to the (003), (006), and (012) planes of the typical hydrotalcite-like LDH phase. This confirms the presence of a highly ordered layered structure in the et-HELDH. Following 100 hours of operation, the main LDH peaks remain clearly visible in the red curve, indicating preservation of the layered crystalline structure. However, a broad peak appears at $26.0°$ in good agreement with (JCPDS no. 41-1487), corresponds to the (002) plane of graphitized carbon from carbon cloth substrate, used as the working electrode. Carbon materials typically exhibit amorphous or graphitic features in this range, and their contribution becomes more pronounced after prolonged operation due to enhanced surface interaction or partial exposure. A peak at around $30.3°$ is often associated with NiO, Fe_2O_3, or mixed metal oxide phases, indicating oxidation of the original LDH structure during prolonged electrochemical operations. Importantly, the LDH phase is retained, and no other significant new phases or decomposition products are detected, highlighting the excellent phase stability and structural resilience of et-HELDH under the harsh operational conditions. These results align with the electrochemical stability data, reinforcing the catalyst's robustness for long-term water splitting and ethanol oxidation applications.
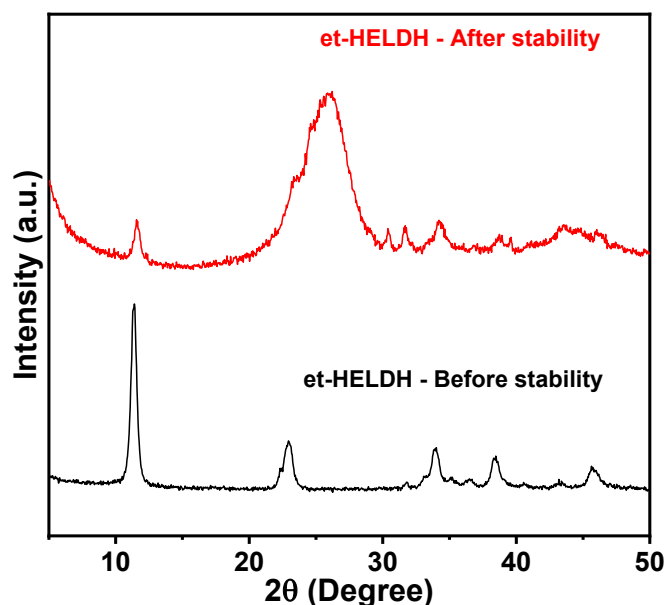
Figure 28. XRD patterns of et-HELDH before and after 100-hour electrochemical stability testing.

5.5 COMPARISON WITH BENCHMARK CATALYSTS

To assess the electrocatalytic efficiency and practical viability of the synthesized NIFeCuMgIn et-HELDH, its electrocatalytic performance was compared with state-of-the-art conventional benchmark catalysts commonly reported in the literature for HER, OER, and EOR. These benchmarks include commercially available or literature-reported catalysts such as Pt/C (for HER), and RuO_2/IrO_2 (for OER and EOR),

Table 2 illustrates the HER performance where the et-HELDH exhibits a low overpotential of 187 mV and a Tafel slope of 136.6 mV dec^{-1}, outperforming many traditional non-noble metal-based catalysts and approaching the activity of Pt-based systems. **Table 3** outline the OER performance. The et-HELDH shows excellent activity with a significantly reduced overpotential to 143 mV and a favorable Tafel slope of 87.9 mV dec^{-1}, demonstrating competitiveness against RuO and IrO_2-based materials. To further enhance the reaction kinetics, the sluggish OER was strategically replaced with the more thermodynamically favorable EOR. The et-HELDH shows excellent activity with a significantly reduced Tafel slope to reach 56.83 mV dec^{-1}. These results collectively highlight the trifunctional activity and robustness of the developed HE-LDH catalyst, validating its potential as a highly effective and economical candidate for integrated electrochemical applications compelling next-generation platform for sustainable and scalable electrochemical energy technologies.

Catalysts	Electrolyte	Substrate	Overpotential (mV vs RHE) (-10 mA.cm^2)	Tafel slope (mV dec^{-1})	Ref.
Pt-C	0.1 M KOH	NF	37	31	[222]
NiFeCr ME-LDH	1 M KOH	CC	356	231	[223]
NiFeCoCuMn HEA	1 M KOH	GC	445	-	[224]
NiFeCoCuMo HEA	1 M KOH	GC	286	125	[224]
NiFeCoCuCr HE-LDH	1 M KOH	NF	545	231	[225]
NiFeCuMgIn et-HELDH	0.5 M KOH	NF	187	136.6	This work

Table 2. Comparison of HER performance of various electrocatalysts.

Catalysts	Electrolyte	Substrate	Overpotential (mV vs RHE) (-10 mA.cm^2)	Tafel slope (mV dec^{-1})	Ref.
IrO$_2$	1 M KOH	GC	300	76	[226]
RuO$_2$	0.5 M KOH	GC	373	70	[227]
NiFeMn ME-LDH	1 M KOH	NF	474	99	[227]
NiFeCoCuMn HEA	1 M KOH	GC	480	-	[224]
NiFeMgCoAl HE-LDH	1 M KOH	CC	230	-	[228]
NiFeCuMnAl HE-LDH	1 M KOH	NF	208	-	[229]
NiFeCuMnCo HE-LDH	1 M KOH	NF	323	85.5	[230]
NiFeCuMgIn et-HELDH	0.5 M KOH	NF	143	87.9	This work
NiFeCuMgIn et-HELDH	0.5 M KOH + 1 M EtOH	NF	143	56.83	This work

Table 3. Comparison of OER performance of various electrocatalysts.

CHAPTER 6. CONCLUSIONS AND FUTURE DIRECTIONS

This study demonstrated the successful design, synthesis and characterization of NiFeCuMgIn HE-LDH with excellent trifunctional electrocatalytic performance for HER, OER, and EOR in alkaline media, achieving substantial improvements in catalytic activity, stability, and energy efficiency. The experimental results showed that the entropy driven stabilization of multiple metal cations within a layered hydroxide framework not only preserved structural integrity but also enabled synergistic interactions among the constituent metals. This led to enhanced redox dynamics, optimized charge transfer, and increased electrochemically active surface area. Among the various samples tested, 20 minutes et-HELDH exhibited the best performance metrics, owing to improved nanosheet dispersion and maximized active site exposure. The substitution of traditional OER with EOR in water electrolysis offered a significant energetic advantage, effectively improving the kinetics for anodic reactions and increasing overall hydrogen production efficiency. This ethanol assisted approach also introduces value added products and improves the safety profile by eliminating oxygen gas evolution.

6.1 KEY FINDINGS AND THEIR IMPLICATIONS

Key findings from this study include significant reductions in overpotentials for all three reactions upon the introduction of entropy stabilized multimetallic compositions. The 20 minutes et-HELDH sample showed the best electrochemical performance, with HER overpotential reduced to 187 mV, OER and EOR reduced to 143 mV, . Tafel slope analysis and EIS revealed faster reaction kinetics and reduced charge transfer resistance. Furthermore, long-term durability tests over 100 hours confirmed the structural robustness and sustained catalytic performance of the et-HELDH catalyst. The replacement of the sluggish OER with EOR in water electrolysis also enabled a significant reduction in energy input, promoting the generation of high-purity hydrogen while offering the potential for valuable byproduct formation from ethanol oxidation.

6.2 LIMITATIONS OF THE CURRENT STUDY

Despite these promising results, the study had several limitations. The mechanistic understanding of the individual roles of each metal cation remains limited. Due to the compositional complexity inherent to high entropy systems, it is challenging to isolate and quantify the specific contribution of each element to the overall catalytic behavior. This hampers the ability to establish precise structure–activity relationships. Additionally, the etching process, while effective, was not optimized for precise control over nanosheet thickness and uniformity, which may affect reproducibility. The durability tests were conducted under laboratory-scale conditions and moderate current densities, which may not fully reflect the stability and performance of the catalysts in industrial applications. Further, the selectivity and product distribution of the EOR were not comprehensively studied, which limits the understanding of the economic and

environmental implications of the anodic oxidation products. The electrochemical testing was conducted exclusively under alkaline conditions; the performance and stability of the HE-LDHs in acidic or neutral media remain uninvestigated, which could restrict broader applicability in different electrochemical environments.

6.3 SUGGESTIONS FOR FUTURE RESEARCH

Building upon the outcomes and limitations of the current study, several promising avenues are suggested for future research to further advance the design and application of HE-LDHs as efficient, multifunctional electrocatalysts. Future efforts should focus on optimizing electrocatalyst composition and structure through defect engineering, surface modification, and composite design. Expanding the compositional space of HE-LDHs through systematic variation in elemental combinations and stoichiometric ratios could offer deeper insights into the individual and synergistic roles of each metal. Investigating how different cationic configurations influence the electronic structure, active site density, and catalytic kinetics will enable more rational and targeted design strategies. In particular, introducing other redox-active or electronically modulating elements could further enhance performance across HER, OER, and EOR.

Additionally, understanding the fundamental differences between OER and alternative anodic reactions (AORs) such as EOR is critical for improving reaction selectivity and controlling the formation of desired products. In-depth mechanistic studies using in-situ/operando spectroscopic techniques and density functional theory (DFT) simulations can provide insights into intermediate species and active site behavior. Profiling and selectivity analysis of EOR reactions using analytical tools like GC-MS and HPLC would also be essential to assess the commercial viability of the generated byproducts. Moreover, to gain a deeper mechanistic understanding, the application of in situ and operando characterization methods is highly recommended. Techniques such as operando X-ray absorption spectroscopy (XAS) and Raman spectroscopy, can reveal dynamic changes in oxidation states, surface reconstruction, and active site evolution during electrocatalytic operation, helping to identify the true catalytic centers and reaction pathways. Another important direction involves the integration of HE-LDHs into complete electrochemical devices. Testing these materials in practical setups such as full water electrolyzers, direct ethanol fuel cells, or hybrid energy storage systems will allow assessment of their long-term durability, energy efficiency, and scalability under realistic operating conditions, which is essential for industrial translation.

In conclusion, HE-LDH represent a promising pathway for advancing next-generation electrochemical energy systems. Integrating water splitting with ethanol electrooxidation enables efficient, sustainable, and cost-effective hydrogen production. Combining experimental research with computational tools such as DFT and machine learning can accelerate the discovery and optimization of catalyst formulations, paving the way for innovative and scalable green energy solutions. Together, these future research directions will not only deepen scientific understanding of high entropy electrocatalysts but also facilitate their practical implementation in sustainable energy technologies.

REFERENCES

[1] J. Luo, W. Zhuo, S. Liu, B. Xu. The optimization of carbon emission prediction in low carbon energy economy under big data. IEEE Access, 12 (2024), pp. 14690-14702.

[2] F. Martins, C. Felgueiras, M. Smitkova, N.J.E. Caetano. Analysis of fossil fuel energy consumption and environmental impacts in European countries.12 (6) (2019), p. 964.

[3] B. Pillot, M. Muselli, P. Poggi, J.B. J.E.p. Dias Historical trends in global energy policy and renewable power system issues in Sub Saharan Africa: the case of solar PV, 127 (2019), pp. 113-124.

[4] R. Wang, R. Zhang. Techno-economic analysis and optimization of hybrid energy systems based on hydrogen storage for sustainable energy utilization by a biological inspired optimization algorithm. J Energy Storage, 66 (2023/08/30/2023), Article 107469.

[5] F. Ahmed, I. Ali, S. Kousar, S. Ahmed. The environmental impact of industrialization and foreign direct investment: empirical evidence from Asia-Pacific region. Environ Sci Pollut Control Ser (2022), pp. 1-15.

[6] F. Dawood, M. Anda, G.M. Shafiullah. Hydrogen production for energy: an overview. Int J Hydrogen Energy, 45 (7) (2020), pp. 3847-3869.

[7] M. Sankir, N.D. Sankir. Hydrogen production technologies.John Wiley & Sons (2017).

[8] A. Valavanidis "Global Warming and Climate Change. Fossil fuels and anthropogenic activities have warmed the Earth's atmosphere, oceans, and land," (2022).

[9] E.I. Epelle, et al. A comprehensive review of hydrogen production and storage: a focus on the role of nanomaterials. Int J Hydrogen Energy, 47 (47) (2022/06/01/2022), pp. 20398-20431.

[10] P.A. Owusu, S.J.C.E. Asumadu-Sarkodie. A review of renewable energy sources, sustainability issues and climate change mitigation. 3 (1) (2016), Article 1167990.

[11] M. Russo, D. Carvalho, N. Martins, A. J. S. E. T. Monteiro, and Assessments. Forecasting the inevitable: a review on the impacts of climate change on renewable energy resources, 52 (2022), Article 102283.

[12] M. Jakob and J. Hilaire, Nature, 2015, 517, 150–152.

[13] C. McGlade and P. Ekins, Nature, 2015, 517, 187–190.

[14] N. Abas, A. Kalair and N. Khan, Futures, 2015, 69, 31–49.

[15] E4tech, Introduction to hydrogen energy projects.

[16] Vanhool (2018), available: https://www.vanhool.be/en/news/van-hool-bouwt-40-waterstofbussen-voor-keulen-en-wuppertal-duitsland-copy.

[17] Y. Yan, B.Y. Xia, B. Zhao, X. Wang. A review on noble-metal-free bifunctional heterogeneous catalysts for overall electrochemical water splitting. J Mater Chem, 4 (45) (2016), pp. 17587-17603.

[18] C. Hu, L. Zhang, J. Gong. Recent progress made in the mechanism comprehension and design of electrocatalysts for alkaline water splitting. Energy Environ Sci, 12 (9) (2019), pp. 2620-2645.

[19] J. Luo, D.A. Vermaas, D. Bi, A. Hagfeldt, W.A. Smith, M. Grätzel. Bipolar membrane-assisted solar water splitting in optimal pH. Adv Energy Mater, 6 (13) (2016), Article 1600100.

[20] IEA. Hydrogen [cited 2023 January 5]; Available from: https://www.iea.org/reports/hydrogen; 2022.

[21] Vesborg PCK, Jaramillo TF. Addressing the terawatt challenge: scalability in the supply of chemical elements for renewable energy. RSC Adv 2012;2(21): 7933–47.

[22] IRENA. Hydrogen [cited Available from: https://www.irena.org/Energy-Transition/Technology/Hydrogen; 2023 January 5.

[23] M. Chatenet, B.G. Pollet, D.R. Dekel, F. Dionigi, J. Deseure, P. Millet, R.D. Braatz, M.Z. Bazant, M. Eikerling, I. Staffell, P. Balcombe, Y. Shao-Horn, H. Schäfer. Water electrolysis: from textbook knowledge to the latest scientific strategies and industrial developments. Chem Soc Rev, 51 (11) (2022), pp. 4583-4762.

[24] H. Zhang, A.W. Maijenburg, X. Li, S.L. Schweizer, R.B. Wehrspohn. Bifunctional heterostructured transition metal phosphides for efficient electrochemical water splitting. Adv Funct Mater, 30 (34) (2020), Article 2003261.

[25] V. Artero, M. Chavarot-Kerlidou, M. Fontecave. Splitting water with cobalt. Angew Chem Int Ed, 50 (32) (2011), pp. 7238-7266.

[26] S. Surendran, S. Shanmugapriya, A. Sivanantham, S. Shanmugam, R. Kalai Selvan. Electrospun carbon nanofibers encapsulated with NiCoP: a multifunctional electrode for supercapattery and oxygen reduction, oxygen evolution, and hydrogen evolution reactions. Adv Energy Mater, 8 (20) (2018), Article 1800555.

[27] A. Kirubakaran, S. Jain and R. K. Nema, Renewable Sustainable Energy Rev., 2009, 13, 2430–2440.

[28] K. Zeng and D. Zhang, Prog. Energy Combust. Sci., 2010, 36, 307–326.

[29] C. W. B. Bezerra, L. Zhang, K. Lee, H. Liu, A. L. B. Marques, E. P. Marques, H. Wang and J. Zhang, Electrochim. Acta, 2008, 53, 4937.

[30] H. Wendt and G. Imarisio, J. Appl. Electrochem., 1988, 18, 1–14.

[31] J. F. Callejas, J. M. McEnaney, C. G. Read, J. C. Crompton, A. J. Biacchi, E. J. Popczun, T. R. Gordon, N. S. Lewis and R. E. Schaak, ACS Nano, 2014, 8, 11101–11107.

[32] A. T. Marshall, S. Sunde, M. Tsypkin and R. Tunold, Int. J. Hydrogen Energy, 2007, 32, 2320–2324.

[33] T. R. Cook, D. K. Dogutan, S. Y. Reece, Y. Surendranath, T. S. Teets and D. G. Nocera, Chem. Rev., 2010, 110, 6474–6502.

[34] M.-R. Gao, Y.-F. Xu, J. Jiang and S.-H. Yu, Chem. Soc. Rev., 2013, 42, 2986–3017.

[35] Y. Shi and B. Zhang, Chem. Soc. Rev., 2016, 45, 1529–1541.

[36] K. Hashimoto, H. Irie and A. Fujishima, Jpn. J. Appl. Phys., 2005, 44, 8269–8285.

[37] A. P. Simpson and A. E. Lutz, Int. J. Hydrogen Energy, 2007, 32, 4811–4820.

[38] L. Barelli, G. Bidini, F. Gallorini and S. Servili, Energy, 2008, 33, 554–570.

[39] D. K. Liguras, D. I. Kondarides and X. E. Verykios, Appl. Catal., B, 2003, 43, 345–354.

[40] Y. Kojima, K. Suzuki, K. Fukumoto, M. Sasaki, T. Yamamoto, Y. Kawai and H. Hayashi, Int. J. Hydrogen Energy, 2002, 27, 1029–1034.

[41] K. Tedsree, T. Li, S. Jones, C. W. A. Chan, K. M. K. Yu, P. A. J. Bagot, E. A. Marquis, G. D. W. Smith and S. C. E. Tsang, Nat. Nanotechnol., 2011, 6, 302–307.

[42] B. H. Liu, Z. P. Li and S. Suda, J. Alloys Compd., 2006, 415, 288–293.

[43] S. Anantharaj, S. R. Ede, K. Sakthikumar, K. Karthick, S. Mishra and S. Kundu, ACS Catal., 2016, 6, 8069–8097.

[44] S. Anantharaj, K. Karthick and S. Kundu, Mater. Today Energy, 2017, 6, 1–26.

[45] E. Fabbri, A. Habereder, K. Waltar, R. Ko¨tz, T. J. Schmidt, R. Kotz, T. J. Schmidt, R. Ko¨tz, T. J. Schmidt, R. Kotz and T. J. Schmidt, Catal. Sci. Technol., 2014, 4, 3800–3821.

[46] T. Hisatomi, J. Kubota and K. Domen, Chem. Soc. Rev., 2014, 43, 7520–7535.

[47] K. T. Fountaine, H. J. Lewerenz and H. A. Atwater, Nat. Commun., 2016, 7, 13706–13714.

[48] J. H. Kim, H. Lee, S. C. Han, H. S. Kim, M. S. Song and J. Y. Lee, Int. J. Hydrogen Energy, 2004, 29, 263–267.

[49] D. Xu, H. Zhang and W. Ye, Catal. Commun., 2007, 8, 1767–1771.

[50] S. Satyapal, J. Petrovic, C. Read, G. Thomas and G. Ordaz, Catal. Today, 2007, 120, 246–256.

[51] U. B. Demirci, O. Akdim and P. Miele, Int. J. Hydrogen Energy, 2009, 34, 2638–2645.

[52] O. Mabayoje, A. Shoola, B. R. Wygant and C. B. Mullins, ACS Energy Lett., 2016, 1, 195–201.

[53] C. Di Giovanni, W. A. Wang, S. Nowak, J. M. Grene`che, H. Lecoq, L. Mouton, M. Giraud and C. Tard, ACS Catal., 2014, 4, 681–687.

[54] W. Zhu, X. Yue, W. Zhang, S. Yu, Y. Zhang, J. J. Wang and J. J. Wang, Chem. Commun., 2016, 52, 1486–1489.

[55] M. Zeng and Y. Li, J. Mater. Chem. A, 2015, 3, 14942–14962.

[56] P. Xiao, W. Chen and X. Wang, Adv. Energy Mater., 2015, 5, 1500985.

[57] Y. Chen, R. Wu, P. Jiang, G. Bian, L. Kong and Y. Dong, RSC Adv., 2015, 5, 60674–60680.

[58] M. Shen, C. Ruan, Y. Chen, C. Jiang, K. Ai and L. Lu, ACS Appl. Mater. Interfaces, 2015, 7, 1207–1218.

[59] X. Xia, C. Zhu, J. Luo, Z. Zeng, C. Guan, C. F. Ng, H. Zhang and H. J. Fan, Small, 2014, 10, 766–773.

[60] B. You, N. Jiang, M. Sheng and Y. Sun, Chem. Commun., 2015, 51, 4252–4255.

[61] P. D. Tran, S. Y. Chiam, P. P. Boix, Y. Ren, S. S. Pramana, J. Fize, V. Artero and J. Barber, Energy Environ. Sci., 2013, 6, 2452–2459.

[62] Y. Yang, K. Zhang, H. Lin, X. Li, H. C. Chan, L. Yang and Q. Gao, ACS Catal., 2017, 7, 2357–2366.

[63] Z. Wu, B. Fang, A. Bonakdarpour, A. Sun, D. P. Wilkinson and D. Wang, Appl. Catal., B, 2012, 125, 59–66.

[64] Z. Qin, Y. Chen, Z. Huang, J. Su, Z. Diao and L. Guo, J. Phys. Chem. C, 2016, 120, 14581–14589.

[65] S. Yu, J. Kim, K. R. Yoon, J. W. Jung, J. Oh and I. D. Kim, ACS Appl. Mater. Interfaces, 2015, 7, 28116–28121.

[66] X. Shang, X. Li, W. H. Hu, B. Dong, Y. R. Liu, G. Q. Han, Y. M. Chai, Y. Q. Liu and C. G. Liu, Appl. Surf. Sci., 2016, 378, 15–21.

[67] J. Kibsgaard, T. F. Jaramillo and F. Besenbacher, Nat. Chem., 2014, 6, 248–253.

[68] A. I. Carim, F. H. Saadi, M. P. Soriaga and N. S. Lewis, J. Mater. Chem. A, 2014, 2, 13835–13839.

[69] C. Xia, Q. Jiang, C. Zhao, M. N. Hedhili and H. N. Alshareef, Adv. Mater., 2016, 28, 77–85.

[70] F. Ming, H. Liang, H. Shi, X. Xu, G. Mei and Z. Wang, J. Mater. Chem. A, 2016, 4, 15148–15155.

[71] X. Liu, J.-Z. Zhang, K.-J. Huang and P. Hao, Chem. Eng. J., 2016, 302, 437–445.

[72] M. Liao, G. Zeng, T. Luo, Z. Jin, Y. Wang, X. Kou and D. Xiao, Three-dimensional coral-like cobalt selenide as an advanced electrocatalyst for highly efficient oxygen evolution reaction, Elsevier Ltd, 2016, vol. 194.

[73] J. Zhu, Y. Koltypin and A. Gedanken, Chem. Mater., 2000, 12, 73–78.

[74] A. T. Swesi, J. Masud and M. Nath, Energy Environ. Sci., 2016, 9, 1771–1782.

[75] Z.Wang, J. Li, X. Tian, X. Wang, Y. Yu,K. A. Owusu, L. He and L. Mai, ACS Appl. Mater. Interfaces, 2016, 8, 19386–19392.

[76] Y. Hou, M. R. Lohe, J. Zhang, S. Liu, X. Zhuang and X. Feng, Energy Environ. Sci., 2016, 9, 478–483.

[77] X. Xu, P. Du, Z. Chen and M. Huang, J. Mater. Chem. A, 2016, 4, 10933–10939.

[78] V. Biju, T. Itoh, A. Anas, A. Sujith and M. Ishikawa, Anal. Bioanal. Chem., 2008, 391, 2469–2495.

[79] Z. Gao, J. Qi, M. Chen, W. Zhang and R. Cao, Electrochim. Acta, 2017, 224, 412–418.

[80] Q. Liu, J. Jin and J. Zhang, ACS Appl. Mater. Interfaces, 2013, 5, 5002–5008.

[81] A. Kleiman-Shwarsctein, Y.-S. Hu, G. D. Stucky and E. W. McFarland, Electrochem. Commun., 2009, 11, 1150–1153.

[82] P. F. Liu, S. Yang, L. R. Zheng, B. Zhang and H. G. Yang, J. Mater. Chem. A, 2016, 4, 9578–9584.

[83] C. Han, Q. Sun, Z. X. Cheng, J. L. Wang, Z. Li, G. Q. Lu and S. X. Dou, J. Am. Chem. Soc., 2014, 136, 17626–17633.

[84] H. Liang, A. N. Gandi, C. Xia, M. N. Hedhili, D. H. Anjum, U. Schwingenschlö gl and H. N. Alshareef, ACS Energy Lett., 2017, 2, 1035–1042.

[85] H. Liu, J. Qu, Y. Chen, J. Li, F. Ye, J. Y. Lee and J. Yang, J. Am. Chem. Soc., 2012, 134, 11602–11610.

[86] K. Ullah, Z. Lei, S. Ye, A. Ali and W. C. Oh, RSC Adv., 2015, 5, 18841–18849.

[87] Y. Xu, R. Wu, J. Zhang, Y. Shi and B. Zhang, Chem. Commun., 2013, 49, 6656–6658.

[88] Y. Shi, Y. Xu, S. Zhuo, J. Zhang and B. Zhang, ACS Appl. Mater. Interfaces, 2015, 7, 2376–2384.

[89] R. Xu, R. Wu, Y. Shi, J. Zhang and B. Zhang, Nano Energy, 2016, 24, 103–110.

[90] M. E. G. Lyons and L. D. Burke, J. Chem. Soc., Faraday Trans. 1, 1987, 83, 299–321.

[91] M. E. G. Lyons and S. Floquet, Phys. Chem. Chem. Phys., 2011, 13, 5314–5335.

[92] M. Gong and H. Dai, Nano Res., 2014, 8, 23–39.

[93] L. Trotochaud and S. W. Boettcher, Scr. Mater., 2014, 74, 25–32.

[94] M. E. G. Lyons and M. P. Brandon, J. Electroanal. Chem., 2010, 641, 119–130.

[95] R. L. Doyle, I. J. Godwin, M. P. Brandon and M. E. G. Lyons, Phys. Chem. Chem. Phys., 2013, 15, 13737.

[96] M. E. G. Lyons and M. P. Brandon, Int. J. Electrochem. Sci., 2008, 3, 1425–1462.

[97] A. T. Marshall and R. G. Haverkamp, Electrochim. Acta, 2010, 55, 1978–1984.

[98] X. Chen, G. Chen and P. L. Yue, J. Phys. Chem. B, 2001, 106, 4623–4628.

[99] T.-C. Wen, J. Electrochem. Soc., 1992, 139, 2158.

[100] J. F. C. Boodts and S. Trassati, J. Electrochem. Soc., 1990, 137, 3784–3789.

[101] J. F. C. Boodts and S. Trassati, J. Electrochem. Soc., 1990, 137, 3784–3789.

[102] R. Berenguer, C. Quijada and E. Morallo´n, Electrochim. Acta, 2009, 54, 5230–5238.

[103] C. Iwakura, M. Inai, T. Uemura and H. Tamura, Electrochim. Acta, 1981, 26, 579–584.

[104] B. Correa-Lozano, C. Comninellis and A. De Battisti, J. Appl. Electrochem., 1996, 26, 683–688.

[105] C. Quijada, J. L. Va, F. Vicent, E. Morallo, D. D. I. Textil, E. P. S. De Alcoy and U. P. De Valencia, J. Appl. Electrochem., 1998, 28, 607–612.

[106] X. Chen, G. Chen and P. L. Yue, J. Phys. Chem. B, 2001, 105, 4623–4628.

[107] H. Zhang, C. Hu, S. Chen, K. Zhang and X. Wang, Catal. Lett., 2012, 142, 809–815.

[108] V. A´vila-Va´zquez, J. C. Cruz, M. GalvA´n-Valencia, J. Ledesma- Garcı´a, L. G. Arriaga, C. GuzmA´n and S.M.Duro´n-Torres, Int. J. Electrochem. Sci., 2013, 8, 10586–10600.

[109] S. Yang, C. Zhao, C. Ge, X. Dong, X. Liu, Y. Liu, Y. Fang, H. Wang and Z. Li, J. Mater. Chem., 2012, 22, 7104–7107.

[110] J. Xu, G. Liu, J. Li and X. Wang, Electrochim. Acta, 2012, 59, 105–112.

[111] S. Natarajan, S. Anantharaj, R. J. Tayade, H. C. Bajaj and S. Kundu, Dalton Trans., 2017, 46, 14382–14392.

[112] V. Mani, S. Anantharaj, S. R. Mishra, K. Nallathamby and S. Kundu, Catal. Sci. Technol., 2017, 7, 5092–5104.

[113] M. Mathankumar, S. Anantharaj, A. K. Nandakumar, S. Kundu and B. Subramanian, J. Mater. Chem. A, 2017, 5, 23053–23066.

[114] S. Anantharaj, M. Venkatesh, A. S. Salunke, T. V. S. V. S. V. Simha, V. Prabu and S. Kundu, ACS Sustainable Chem. Eng., 2017, 5, 10072–10083.

[115] I. Hwang, Int. J. Electrochem. Sci., 2016, 11, 6204–6214.

[116] S. Mao, Z. Wen, T. Huang, Y. Hou and J. Chen, Energy Environ. Sci., 2014, 7, 609–616.

[117] T. Maiyalagan, K. a Jarvis, S. Therese, P. J. Ferreira and A. Manthiram, Nat. Commun., 2014, 5, 3949–3955.

[118] S. Peng, N. Li, X. Han, W. Sun, M. Srinivasan, S. G.Mhaisalkar, F. Cheng, Q. Yan, J. Chen and S. Ramakrishna, Angew. Chem., Int. Ed., 2014, 53, 12594–12599.

[119] M. Dinamani and P. V. Kamath, J. Appl. Electrochem., 2000, 30, 1157–1161.

[120] W. Zhang, W. Jiang, L. Yu, Z. Fu, W. Xia and M. Yang, Int. J. Hydrogen Energy, 2009, 34, 473–480.

[121] S. Anantharaj, K. Karthick, M. Venkatesh, T. V. S. V. Simha, A. S. Salunke, L. Ma, H. Liang and S. Kundu, Nano Energy, 2017, 39, 30–43.

[122] D. Tang, J. Liu, X. Wu, R. Liu and X. Han, ACS Appl. Mater. Interfaces, 2014, 6, 7918–7925.

[123] Y. Zhang, B. Cui, C. Zhao, H. Lin and J. Li, Phys. Chem. Chem. Phys., 2013, 15, 7363–7369.

[124] K. Fan, H. Chen, Y. Ji, H. Huang, P. M. Claesson, Q. Daniel, B. Philippe, H. Rensmo, F. Li, Y. Luo and L. Sun, Nat. Commun., 2016, 7, 11981–11989.

[125] J. Jiang, A. Zhang, L. Li and L. Ai, J. Power Sources, 2015, 278, 445–451.

[126] F. Dionigi and P. Strasser, Adv. Energy Mater., 2016, 6, 1600621.

[127] L. Feng, A. Li, Y. Li, J. Liu, L. Wang, L. Huang, Y. Wang and X. Ge, ChemPlusChem, 2017, 82, 483–488.

[128] Z. Li, M. Shao, H. An, Z. Wang, S. Xu, M. Wei, D. G. Evans and X. Duan, Chem. Sci., 2015, 6, 6624–6631.

[129] Z. Jia, Y. Wang and T. Qi, RSC Adv., 2015, 5, 83314–83319.

[130] D. G. Evans and R. C. T. Slade, in Layered Double Hydroxides, ed. X. Duan and D. G. Evans, Springer-Verlag, Berlin/ Heidelberg, 2006, vol. 119, pp. 1–87.

[131] M. Gong, Y. Li, H. Wang, Y. Liang, J. Z. Wu, J. Zhou, J. Wang, T. Regier, F. Wei and H. Dai, J. Am. Chem. Soc., 2013, 135, 8452–8455.

[132] R. Valdez, D. B. Grotjahn, D. K. Smith, J. M. Quintana and A. Olivas, Int. J. Electrochem. Sci., 2015, 10, 909–918.

[133] G. Abella´n, J. a. Carrasco, E. Coronado, J. Romero and M. Varela, J. Mater. Chem. C, 2014, 2, 3723–3731.

[134] X. Zhu, C. Tang, Q. Zhang, H.-F. Wang, C. Yang and F. Wei, J. Mater. Chem. A, 2015, 3, 24540–24546.

[135] C. Dong, X. Yuan, X. Wang, X. Liu, W. Dong and R. Wang, J. Mater. Chem. A, 2016, 4, 11292–11298.

[136] C. Qiao, Y. Zhang, Y. Zhu, C. Cao, X. Bao and J. Xu, J. Mater.Chem. A, 2015, 3, 6878–6883.

[137] Y. Li, L. Zhang, X. Xiang, D. Yan and F. Li, J. Mater. Chem. A, 2014, 2, 13250–13258.

[138] S. Anantharaj, J. Kennedy and S. Kundu, ACS Appl. Mater. Interfaces, 2017, 9, 8714–8728.

[139] K. Karthick, S. Anantharaj, P. E. Karthik, B. Subramanian and S. Kundu, Inorg. Chem., 2017, 56, 6734–6745.

[140] S. Anantharaj, P. N. Reddy and S. Kundu, Inorg. Chem., 2017, 56, 1742–1756.

[141] M. Wu, P. K. Shen, Z. Wei, S. Song and M. Nie, J. Power Sources, 2007, 166, 310–316.

[142] W. F. Chen, J. M. Schneider, K. Sasaki, C. H. Wang, J. Schneider, S. Iyer, S. Iyer, Y. Zhu, J. T. Muckerman and E. Fujita, ChemSusChem, 2014, 7, 2414–2418.

[143] W. Sheng, H. a. Gasteiger and Y. Shao-Horn, J. Electrochem. Soc., 2010, 157, B1529–B1536.

[144] B. E. Conway and L. Bai, J. Electroanal. Chem., 1986, 198, 149–175.

[145] X. Zhou, H. Dong and A.-M. Ren, Int. J. Hydrogen Energy, 2016, 41, 5670–5681.

[146] J. O. Bockris and T. Otagawa, J. Phys. Chem., 1983, 87, 2960–2971.

[147] Younis MA, Hou Y. Chapter 10 - nanocarbon-based hybrids as electrocatalysts for hydrogen and oxygen evolution from water splitting. In: Zhao Q, editor. Advanced nanomaterials for pollutant sensing and environmental catalysis. Elsevier; 2020. p. 379–418.

[148] Dau H, Limberg C, Reier T, Risch M, Roggan S, Strasser P. The mechanism of water oxidation: from electrolysis via homogeneous to biological catalysis. ChemCatChem 2010;2(7):724–61.

[149] Bolar S, , Shit, S, Samanta P, Chandra Murmu N, Kuila T. The structure–activity correlation of bifunctional MnO_2 polymorphic and MoS_2-based heterostructures: a highly efficient, robust electrochemical water oxidation and reduction reaction catalyst in alkaline pH. Sustain Energy Fuels 2021;5(4): 1148–57.

[150] Zhang H, Maijenburg AW, Li X, Schweizer SL, Wehrspohn RB. Bifunctional heterostructured transition metal phosphides for efficient electrochemical water splitting. Adv Funct Mater 2020;30(34):2003261.

[151] Zhao G, Rui K, Dou SX, Sun W. Heterostructures for electrochemical hydrogen evolution reaction: a review. Adv Funct Mater 2018;28(43):1803291.

[152] Fang Y, Cao D, Shi Y, Guo S, Wang Q, Zhang G, Cui P, Cheng S. Highly porous Pt_2Ir alloy nanocrystals as a superior catalyst with high-efficiency C–C bond cleavage for ethanol electrooxidation. J Phys Chem Lett 2021;12(29):6773–80.

[153] Bai J, Liu D, Yang J, Chen Y. Nanocatalysts for electrocatalytic oxidation of ethanol. ChemSusChem 2019;12(10):2117–32.

[154] M. G. Walter, E. L. Warren, J. R. McKone, S. W. Boettcher, Q. Mi, E. A. Santori and N. S. Lewis, Chem. Rev., 2010, 110, 6446–6473.

[155] Y. Lee, J. Suntivich, K. J. May, E. E. Perry and Y. Shao-Horn, J. Phys. Chem. Lett., 2012, 3, 399–404.

[156] B. S. Yeo and A. T. Bell, J. Am. Chem. Soc., 2011, 133, 5587–5593.

[157] M. Ledendecker, G. Clavel, M. Antonietti and M. Shalom, Adv. Funct. Mater., 2015, 25, 393–399.

[158] Y. Liang, Y. Li, H. Wang, L. Zhou, J. Wang, T. Regier and H. Dai, Nat. Mater., 2011, 10, 780–786.

[159] M. Gong, Y. Li, H. Wang, Y. Liang, J. Wu, J. Zhou, J. Wang, T. Regier, F. Wei and H. Dai, J. Am. Chem. Soc., 2013, 135, 8452–8455.

[160] X. Y. Lu, Y. H. Ng and C. Zhao, ChemSusChem, 2014, 7, 82–86.

[161] J. Duan, S. Chen and C. Zhao, Nat. Commun., 2017, 8, 1534.

[162] M. Liu, W. Zheng, S. Ran, S. T. Boles, L. Yoon and S. Lee, Adv. Mater. Interfaces, 2018, 5, 1800849.

[163] X. Luo, Q. Shao, Y. Pi and X. Huang, ACS Catal., 2019, 9, 1013–1018.

[164] Y. X. Chen, A. Lavacchi, H. A. Miller, M. Bevilacqua, J. Filippi, M. Innocenti, A. Marchionni, W. Oberhauser, L. Wang and F. Vizza, Nat. Commun., 2014, 5, 4036.

[165] P. Kuśtrowski , D. Sułkowska , L. Chmielarz and R. Dziembaj , Appl. Catal., A, 2006, 302 , 317 —324 CrossRef.

[166] L. Meili , P. V. Lins , C. L. P. S. Zanta , J. I. Soletti , L. M. O. Ribeiro , C. B. Dornelas , T. L. Silva and M. G. A. Vieira , Appl. Clay Sci., 2019, 168 , 11 —20 CrossRef.

[167] P. Lins , D. Henrique , A. Ide , C. Zanta and L. Meili , Sci. Pollut. Res., 2019, 26 , 31804 —31811 CrossRef.

[168] A. Navajas , I. Campo , A. Moral , J. Echave , O. Sanz , M. Montes and J. A. Odriozola , Fuel, 2018, 211 , 173 —181 CrossRef.

[169] M. Hájek , A. Tomášová , J. Kocík and V. Podzemna , Appl. Clay Sci., 2018, 154 , 28 —35 CrossRef.

[170] Zhang, Xinfang, et al. "Active corrosion protection of mg–al layered double hydroxide for magnesium alloys: a short review." Coatings 11.11 (2021): 1316.

[171] G. Hincapié , D. López and A. Moreno , Catal. Today, 2018, 302 , 277 —285 CrossRef.

[172] H. Griffiths Layered Double Hydroxides: Structure, Synthesis and Catalytic Applications , 2012 Search PubMed.

[173] J.-W. Yeh, S.-K. Chen, S.-J. Lin, J.-Y. Gan, T.-S. Chin, T.-T. Shun, C.-H. Tsau, S.-Y. Chang Nanostructured high-entropy alloys with multiple principal elements: novel alloy design concepts and outcomes Adv. Eng. Mater., 6 (2004), pp.

[174] B. Cantor, I.T.H. Chang, P. Knight, A.J.B. Vincent Microstructural development in equiatomic multicomponent alloys.Mater. Sci. Eng. A, 375–377 (2004), pp. 213-218.

[175] H. Li, H. Zhu, S. Sun, J. Hao, Z. Zhu, F. Xu, S. Lu, F. Duan, M. Du Thermodynamically driven metal diffusion strategy for controlled synthesis of high-entropy alloy electrocatalysts. Chem. Commun., 57 (2021), pp.

[176] X. Wang, Q. Dong, H. Qiao, Z. Huang, M.T. Saray, G. Zhong, Z. Lin, M. Cui, A. Brozena, M. Hong, Q. Xia, J. Gao, G. Chen, R. Shahbazian-Yassar, D. Wang, L. Hu. Continuous synthesis of hollow high-entropy nanoparticles for energy and catalysis applications. Adv. Mater., 32 (2020).

[177] N. Kumar Katiyar, K. Biswas, J.-W. Yeh, S. Sharma, C. Sekhar Tiwary. A perspective on the catalysis using the high entropy alloys. Nano Energy, 88 (2021), Article 106261.

[178] M. Fu, X. Ma, K. Zhao, X. Li, D. Su. High-entropy materials for energy-related applications. IScience, 24 (2021), Article 102177.

[179] Y.F. Ye, Q. Wang, J. Lu, C.T. Liu, Y. Yang. High-entropy alloy: challenges and prospects. Mater. Today, 19 (2016), pp. 349-362.

[180] W. Xiong, A.X.Y. Guo, S. Zhan, C.-T. Liu, S.C. Cao.

Refractory high-entropy alloys: a focused review of preparation methods and properties. J. Mater. Sci. Technol., 142 (2023), pp. 196-215.

[181] S. Singh, N.K. Katiyar, S. Goel, S.N. Joshi. Phase prediction and experimental realisation of a new high entropy alloy using machine learning. Sci. Rep., 13 (2023), p. 4811.

[182] Y. Zhang, R. Li. New advances in high-entropy alloys. Entropy, 22 (2020), p. 1158.

[183] A. Sarkar, L. Velasco, D. Wang, Q. Wang, G. Talasila, L. de Biasi, C. Kübel, T. Brezesinski, S.S. Bhattacharya, H. Hahn, B. Breitung. High entropy oxides for reversible energy storage. Nat. Commun., 9 (2018), p. 3400,

[184] B. Zhao, Y. Du, Z. Yan, L. Rao, G. Chen, M. Yuan, L. Yang, J. Zhang, R. Che. Structural defects in phase-regulated high-entropy oxides toward superior microwave absorption properties. Adv. Funct. Mater., 33 (2023),

[185] S.H. Albedwawi, A. AlJaberi, G.N. Haidemenopoulos, K. Polychronopoulou. High entropy oxides-exploring a paradigm of promising catalysts: a review. Mater. Des., 202 (2021), Article 109534,

[186] Y. Pan, J.-X. Liu, T.-Z. Tu, W. Wang, G.-J. Zhang. High-entropy oxides for catalysis: a diamond in the rough. Chem. Eng. J., 451 (2023), Article 138659,

[187] L. Lin, K. Wang, R. Azmi, J. Wang, A. Sarkar, M. Botros, S. Najib, Y. Cui, D. Stenzel, P. Anitha Sukkurji, Q. Wang, H. Hahn, S. Schweidler, B. Breitung. Mechanochemical synthesis: route to novel rock-salt-structured high-entropy oxides and oxyfluorides. J. Mater. Sci., 55 (2020), pp. 16879-16889.

[188] Q. Zheng, Z. Ren, Y. Zhang, X. Liu, J. Ma, L. Li, X. Liu, L. Chen. Surface-stabilized high-entropy layered Oxyfluoride cathode for Lithium-ion batteries. J. Phys. Chem. Lett., 14 (2023), pp. 5553-5559.

[189] A. Joshi, S. Chakrabarty, S.H. Akella, A. Saha, A. Mukherjee, B. Schmerling, M. Ejgenberg, R. Sharma, M. Noked. High-entropy co-free O3-type layered Oxyfluoride: a promising air-stable cathode for sodium-ion batteries. Adv. Mater., 35 (2023),

[190] L. Feng, W.G. Fahrenholtz, D.W. Brenner. High-entropy ultra-high-temperature borides and carbides: a new class of materials for extreme environments. Annu. Rev. Mater. Res., 51 (2021), pp. 165-185.

[191] M. Qin, Q. Yan, Y. Liu, J. Luo. A new class of high-entropy M3B4 borides. J. Adv. Ceram., 10 (2021), pp. 166-172,

[192]   H.-R. Mao, E.-T. Dong, S.-B. Jin, X.-M. Qiu, P. Shen.   Ultrafast high-temperature synthesis and densification of high-entropy carbides. J. Eur. Ceram. Soc., 42 (2022), pp. 4053-4065.

[193] K. Sidnov, D. Moskovskikh, S. Volodko, S. Yudin, C. Zhang, S. Vorotilo.High-throughput assessment of stability and mechanical properties of medium- and high-entropy carbides: bridging empirical criteria and ab-initio calculations. Comput. Mater. Sci., 244 (2024), Article 113158

[194] O.F. Dippo, N. Mesgarzadeh, T.J. Harrington, G.D. Schrader, K.S. Vecchio. Bulk high-entropy nitrides and carbonitrides. Sci. Rep., 10 (2020), Article 21288,

[195] J. Liu, X. Zhang, V. Pelenovich, Y. Xu, K. Tan, L. Hu, X. Zeng, Z. Zeng, Y. Lei, Y. Chen, B. Yang. Effects of duty cycle on microstructure and mechanical properties of (AlCrNbSiTi)N high-entropy nitride hard coatings deposited by pulsed arc ion plating. Vacuum, 225 (2024), Article 113219,

[196] C. Liu, M. Kuang, C. Bao, K. Xiang, F. Shen, H. Liu. The design of high-entropy metal sulfides promising high-performance gaseous elemental mercury removal. Fuel, 361 (2024), Article 130659,

[197] Y. Zhao, J. You, Z. Wang, G. Liu, X. Huang, M. Duan, H. Zhang. High-entropy FeCoNiCuAlV sulfide as an efficient and reliable electrocatalyst for oxygen evolution reaction. Int. J. Hydrog. Energy, 70 (2024), pp. 599-605.

[198] D. Lai, Q. Kang, F. Gao, Q. Lu. High-entropy effect of a metal phosphide on enhanced overall water splitting performance. J. Mater. Chem. A, 9 (2021), pp. 17913-17922,

[199] X. Zhao, Z. Xue, W. Chen, Y. Wang, T. Mu. Eutectic synthesis of high-entropy metal phosphides for Electrocatalytic water splitting. ChemSusChem, 13 (2020), pp. 2038-2042.

[200] K.-Y. Tsai, M.-H. Tsai, J.-W. Yeh. Sluggish diffusion in co–Cr–Fe–Mn–Ni high-entropy alloys. Acta Mater., 61 (2013), pp. 4887-4897.

[201] X. Wang, W. Guo, Y. Fu. High-entropy alloys: emerging materials for advanced functional applications. J. Mater. Chem. A, 9 (2021), pp. 663-701,

[202] J.-W. Yeh, S.-Y. Chang, Y.-D. Hong, S.-K. Chen, S.-J. Lin. Anomalous decrease in X-ray diffraction intensities of cu–Ni–Al–co–Cr–Fe–Si alloy systems with multi-principal elements. Mater. Chem. Phys., 103 (2007), pp. 41-46.

[203] X. Chen, C. Si, Y. Gao, J. Frenzel, J. Sun, G. Eggeler, Z. Zhang. Multi-component nanoporous platinum–ruthenium–copper–osmium–iridium alloy with enhanced electrocatalytic activity towards methanol oxidation and oxygen reduction. J. Power Sources, 273 (2015), pp. 324-332.

[204] A.-L. Wang, H.-C. Wan, H. Xu, Y.-X. Tong, G.-R. Li. Quinary PdNiCoCuFe alloy nanotube arrays as efficient Electrocatalysts for methanol oxidation. Electrochim. Acta, 127 (2014), pp. 448-453.

[205] C.-F. Tsai, P.-W. Wu, P. Lin, C.-G. Chao, K.-Y. Yeh. Sputter deposition of multi-element nanoparticles as Electrocatalysts for methanol oxidation. Jpn. J. Appl. Phys., 47 (2008), p. 5755.

[206] J. Hu, T. Guo, X. Zhong, J. Li, Y. Mei, C. Zhang, Y. Feng, M. Sun, L. Meng, Z. Wang, B. Huang, L. Zhang, Z. Wang. In situ reconstruction of high-entropy Heterostructure catalysts for stable oxygen evolution Electrocatalysis under industrial conditions. Adv. Mater., 36 (2024).

[207] Y. Mei, Y. Feng, C. Zhang, Y. Zhang, Q. Qi, J. Hu. High-entropy alloy with Mo-coordination as efficient Electrocatalyst for oxygen evolution reaction. ACS Catal., 12 (2022), pp. 10808-10817,

[208] M.W. Glasscott, A.D. Pendergast, S. Goines, A.R. Bishop, A.T. Hoang, C. Renault, J.E. Dick. Electrosynthesis of high-entropy metallic glass nanoparticles for designer, multi-functional electrocatalysis. Nat. Commun., 10 (2019), p. 2650.

[209] Z. Jin, J. Lv, H. Jia, W. Liu, H. Li, Z. Chen, X. Lin, G. Xie, X. Liu, S. Sun, H. Qiu. Nanoporous Al-Ni-co-Ir-Mo high-entropy alloy for record-high water splitting activity in acidic environments. Small, 15 (2019).

[210] T. Wang, H. Chen, Z. Yang, J. Liang, S. Dai. High-entropy perovskite fluorides: a new platform for oxygen evolution catalysis. J. Am. Chem. Soc., 142 (2020), pp. 4550-4554,

[211] X. Cui, B. Zhang, C. Zeng, S. Guo. Electrocatalytic activity of high-entropy alloys toward oxygen evolution reaction. MRS Commun., 8 (2018), pp. 1230-1235,

[212] T. Löffler, A. Savan, H. Meyer, M. Meischein, V. Strotkötter, A. Ludwig, W. Schuhmann. Design of Complex Solid-Solution Electrocatalysts by correlating configuration, adsorption energy distribution patterns, and activity curves. Angew. Chem. Int. Ed., 59 (2020), pp. 5844-5850.

[213] S. Li, X. Tang, H. Jia, H. Li, G. Xie, X. Liu, X. Lin, H.-J. Qiu. Nanoporous high-entropy alloys with low Pt loadings for high-performance electrochemical oxygen reduction. J. Catal., 383 (2020), pp. 164-171.

[214] T.A.A. Batchelor, J.K. Pedersen, S.H. Winther, I.E. Castelli, K.W. Jacobsen, J. Rossmeisl. High-entropy alloys as a discovery platform for Electrocatalysis. Joule, 3 (2019), pp. 834-845.

[215] M. Naguib, V.N. Mochalin, M.W. Barsoum, Y. Gogotsi. 25th anniversary article: MXenes: a new family of two-dimensional materials. Adv. Mater., 26 (2014), pp. 992-1005.

[216] M. Li, X. Xi, H. Wang, X. Lyu, Z. Li, R. Zhu, X. Ren, D. Yang, A. Dong. A universal, green, and self-reliant electrolytic approach to high-entropy layered (oxy)hydroxide nanosheets for efficient electrocatalytic water oxidation. J. Colloid Interface Sci., 617 (2022), pp. 500-510.

[217] L. Lv, Z. Yang, K. Chen, C. Wang, Y. Xiong. 2D layered double hydroxides for oxygen evolution reaction: from fundamental design to application. Adv. Energy Mater., 9 (2019).

[218] H. Zhang. Ultrathin two-dimensional nanomaterials. ACS Nano, 9 (2015), pp. 9451-9469.

[219] Y.-N. Zhou, R.-Y. Fan, Y.-N. Cao, H.-Y. Wang, B. Dong, H.-Y. Zhao, F.-L. Wang, J.-F. Yu, Y.-M. Chai. Oriented and robust anchoring of Fe via anodic interfacial coordination assembly on ultrathin co hydroxides for efficient water oxidation. Nanoscale, 13 (2021), pp. 13463-13472.

[220] Ding, Yiran, et al. "A Monolayer High-Entropy Layered Hydroxide Frame for Efficient Oxygen Evolution Reaction." Advanced Materials (2023): 2302860.

[221] K. Gu, X. Zhu, D. Wang, N. Zhang, G. Huang, W. Li, P. Long, J.Tian, Y. Zou, Y. Wang, R. Chen, S. Wang, J. Energy Chem. 2021, 60,121.

[222] Wan, Jun, et al. "Structure confined porous Mo2C for efficient hydrogen evolution." Advanced Functional Materials 27.45 (2017): 1703933.

[223] Zhou, Hongyu, Jiang Liu, and Chunli Xu. "NiFeCr–S/NiS/NF with modified 2D nanosheet array as bifunctional electrocatalysts for overall water splitting." International Journal of Hydrogen Energy 48.85 (2023): 33088-33097.

[224] Asghari Alamdari, Armin, et al. "Exploring the Role of Mo and Mn in Improving the OER and HER Performance of CoCuFeNi-based High-entropy Alloys." ACS Applied Energy Materials 7.6 (2024): 2423-2435.

[225] Xu, Hui, et al. "High-entropy layered double hydroxides tailor Pt electron state for promoting acidic hydrogen evolution reaction." Journal of Colloid and Interface Science 684 (2025): 566-574.

[226] J. Chang, Y. Xiao, M. Xiao, J. Ge, C. Liu, W. Xing, ACS Catal. 2015, 5, 6874.

[227] Wang, Ze, et al. "NiFeMn-layered double hydroxides linked by graphene as high-performance electrocatalysts for oxygen evolution reaction." Nanomaterials 12.13 (2022): 2200.

[228] Wu, Han, et al. "High-Entropy layered double hydroxides with highly adjustable components for enhancing electrocatalytic oxygen evolution." ACS Applied Materials & Interfaces 15.32 (2023): 38423-38432.

[229] Sun, Xiangyun, et al. "High-entropy layered double hydroxide catalyst decorated with Ag nanoparticles for highly efficient water oxidation." International Journal of Hydrogen Energy 67 (2024): 111-118.

[230] Wang, Fangqing, et al. "Activating lattice oxygen in high-entropy LDH for robust and durable water oxidation." Nature Communications 14.1 (2023): 6019.

APPENDICES

SUPPLEMENTARY DATA

S1. Material Characterization Techniques

The samples' crystalline structure and phase composition were examined using X-ray diffraction (XRD) on a TZY-XRD (D/MAX-TTRIII(CBO)) system with Cu–Kα radiation (λ = 1.5418 Å). The morphology and microstructure were characterized through Scanning Electron Microscopy (SEM) on a Hitachi S4800 field-emission scanning electron microanalyzer coupled with energy-dispersive X-ray spectroscopy (EDX). High-resolution Transmission Electron Microscopy (HR-TEM) and High Angle Annular Dark Field – Scanning Transmission Electron Microscopy (HAADF-STEM) micrographs were also recorded via Nancy JEOL ARM 200F with 2 CS correctors. The TEM has an in Nancy: MSC794 camera Gatan one view, JEOL HAADF detector, and a double-tilt sample holder.

S2. Electrochemical Measurements

Typically, electrochemical performance was measured using a Biologic electrochemical workstation instrument with techniques like Linear scanning voltammetry (LSV), cyclic voltammetry (CV), chronopotentiometry (CP), and Electrochemical impedance spectroscopy (EIS). All the electrochemical experiments were carried out in a three-electrode set-up (Ag/AgCl-reference, carbon black-graphite composite (CB/Gr)-counter, and as-prepared catalysts-working electrode, electrolyte-0.5 m KOH for HER and OER and mixed electrolyte solution containing 0.5 M KOH and 1 M EtOH for EOR. Before measuring LSV, CV was performed at a scan rate of 50 mV s^{-1} for 20 cycles to activate the surface of the catalyst. Then, LSV was carried out at a scan rate of 10 mV s^{-1}. . Tafel plots, derived from LSV data, were used to evaluate reaction kinetics and compare Tafel slopes across different reactions. The electrochemical double-layer capacitance (C_{dl}) of various electrocatalysts was also obtained using the CV in the non-Faradic area at varied sweeping speeds spanning from 80 mV s^{-1} to 200 mV s^{-1}. Electrochemical impedance spectroscopy (EIS) measurements were carried out from 0.01 to 100 000 Hz with an amplitude of 10 mV and an overpotential of 1.1 V. The electrochemical double-layer capacitance, expected to be linearly proportional to the Electrochemical active surface area (ECSA), was determined by measuring the capacitive current at non-Faradic regions from scan rate-dependent CV runs by the following equation: ECSA = C_{dl}/C_s, where C_s and C_{dl} are the specific capacitance in an acidic medium (0.040 mF cm^{-2} for the KOH electrolyte) and the specific capacitance of the double-layer region, respectively. In this work, All the potentials were calibrated to reversible hydrogen electrode (RHE) according to the equation: $E_{RHE} = E_{Ag/AgCl} + 0.197 + 0.0591 \times$ pH.

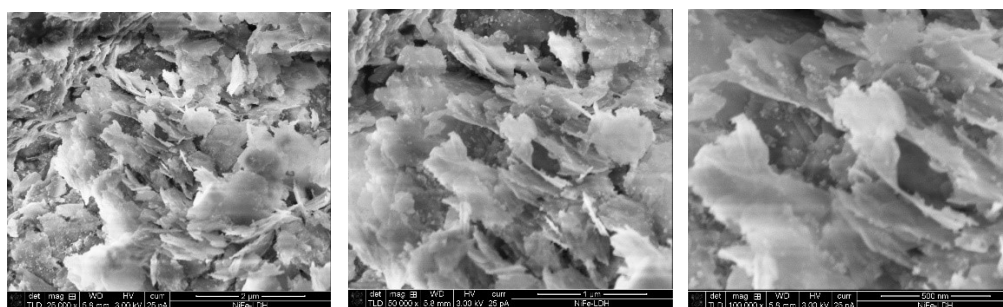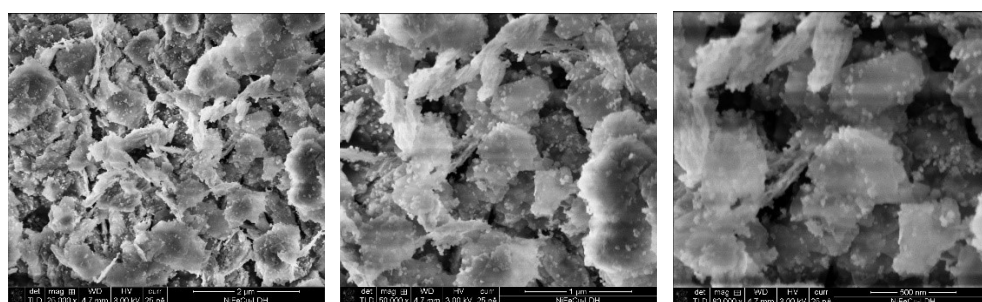**Figure S1.** SEM images of NiFe LDH

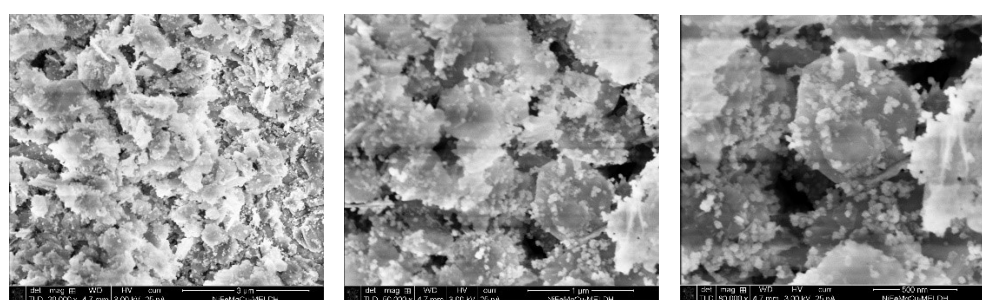**Figure S2.** SEM images of NiFeCu ME-LDH

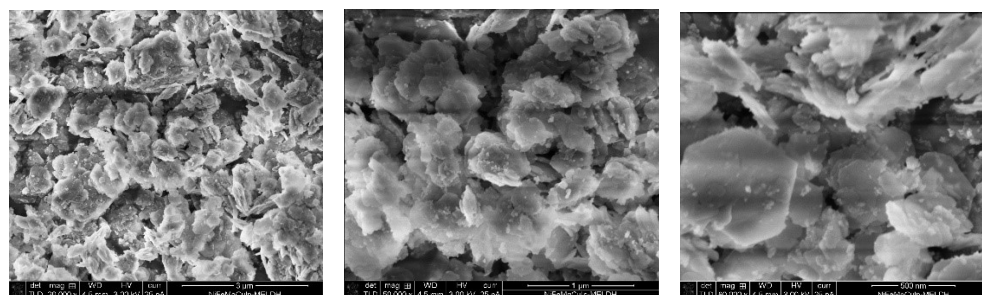**Figure S3.** SEM images of NiFeCuMg ME-LDH

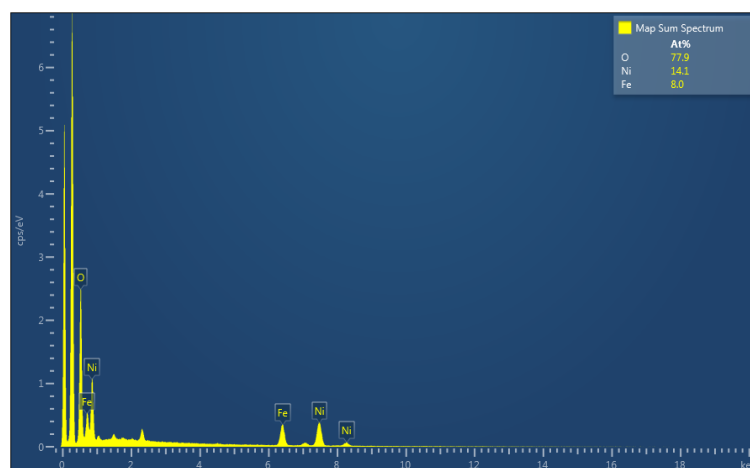**Figure S4.** SEM images of NiFeCuMgIn HE-LDH
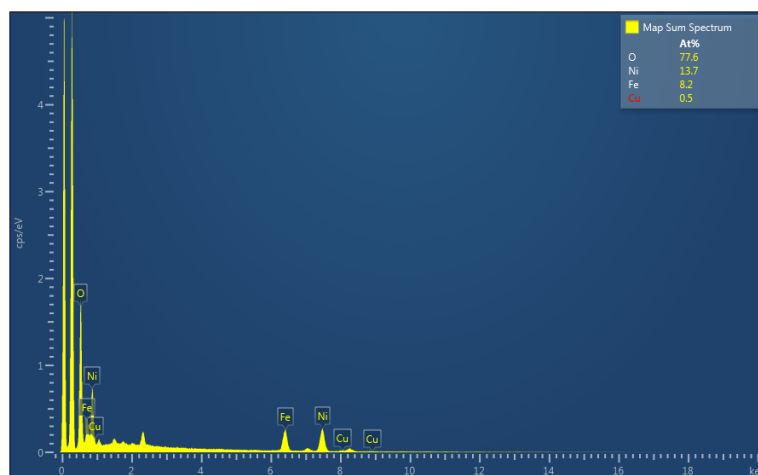
Figure S5. EDX maps of NiFe LDH

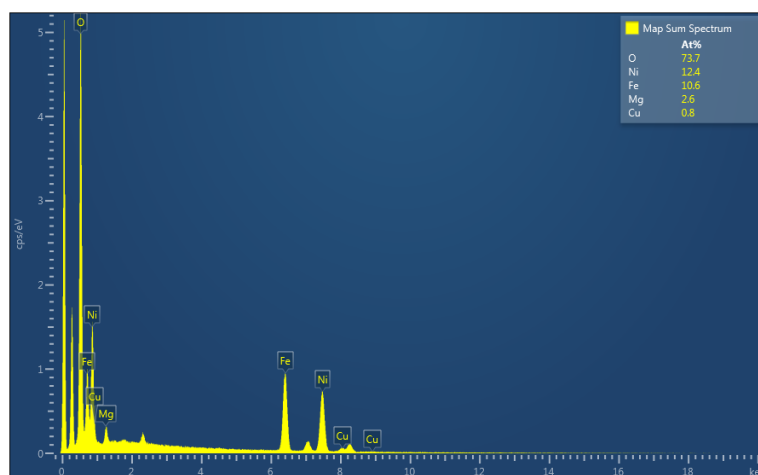
Figure S6. EDX maps of NiFeCu ME-LDH
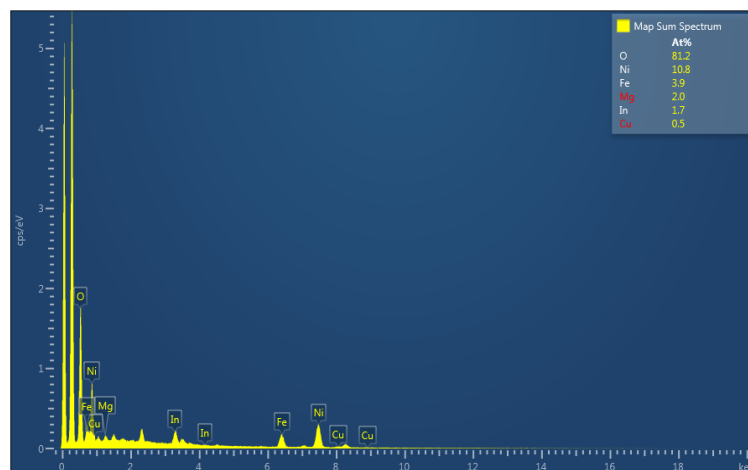
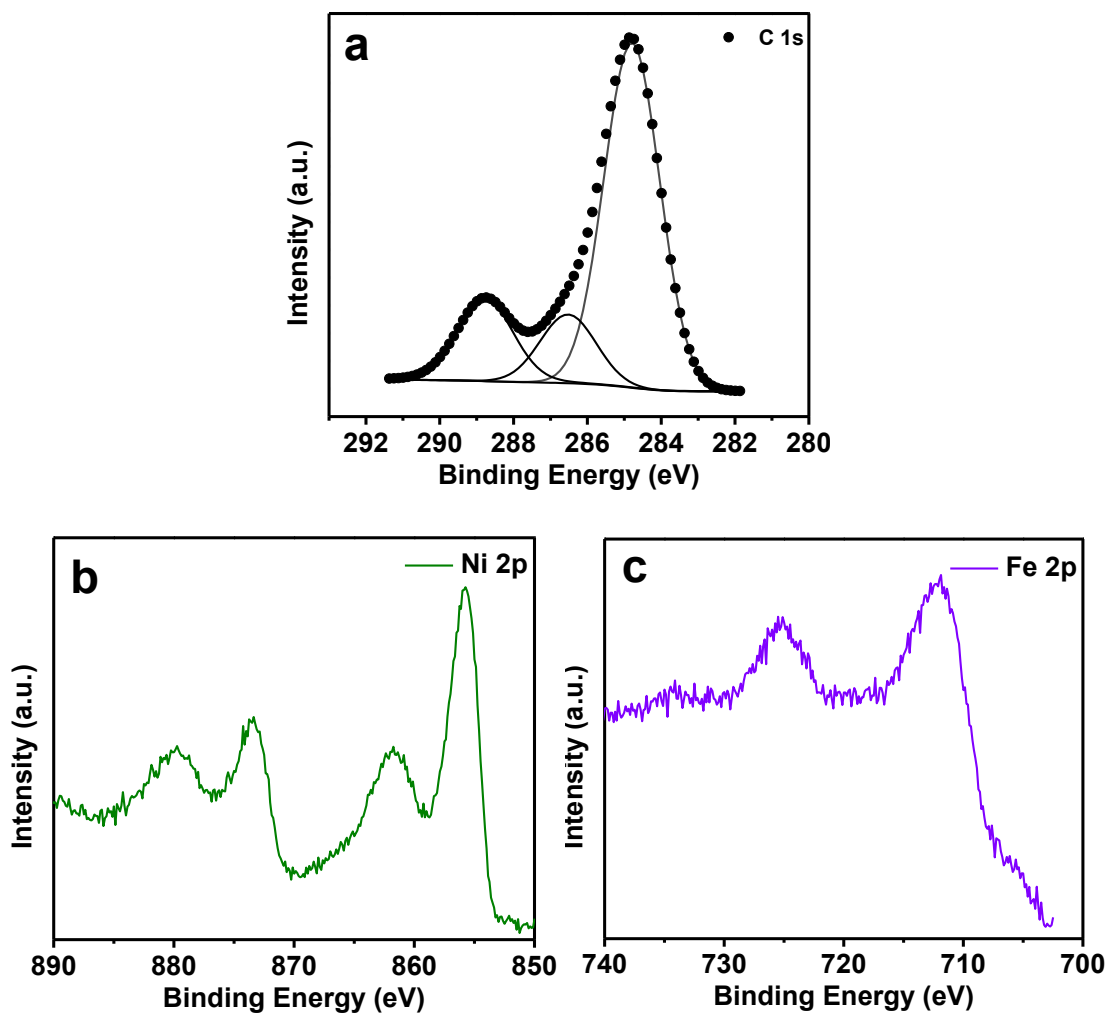**Figure S7.** EDX maps of NiFeCuMg ME-LDH

Figure S8. EDX maps of NiFeCuMgIn HE-LDH

Figure S9. XPS spectrum of the, (a) C 1s element of NiFe LDH, (b) Ni 2p element of NiFe LDH, and (c) Fe 3p element of NiFe LDH
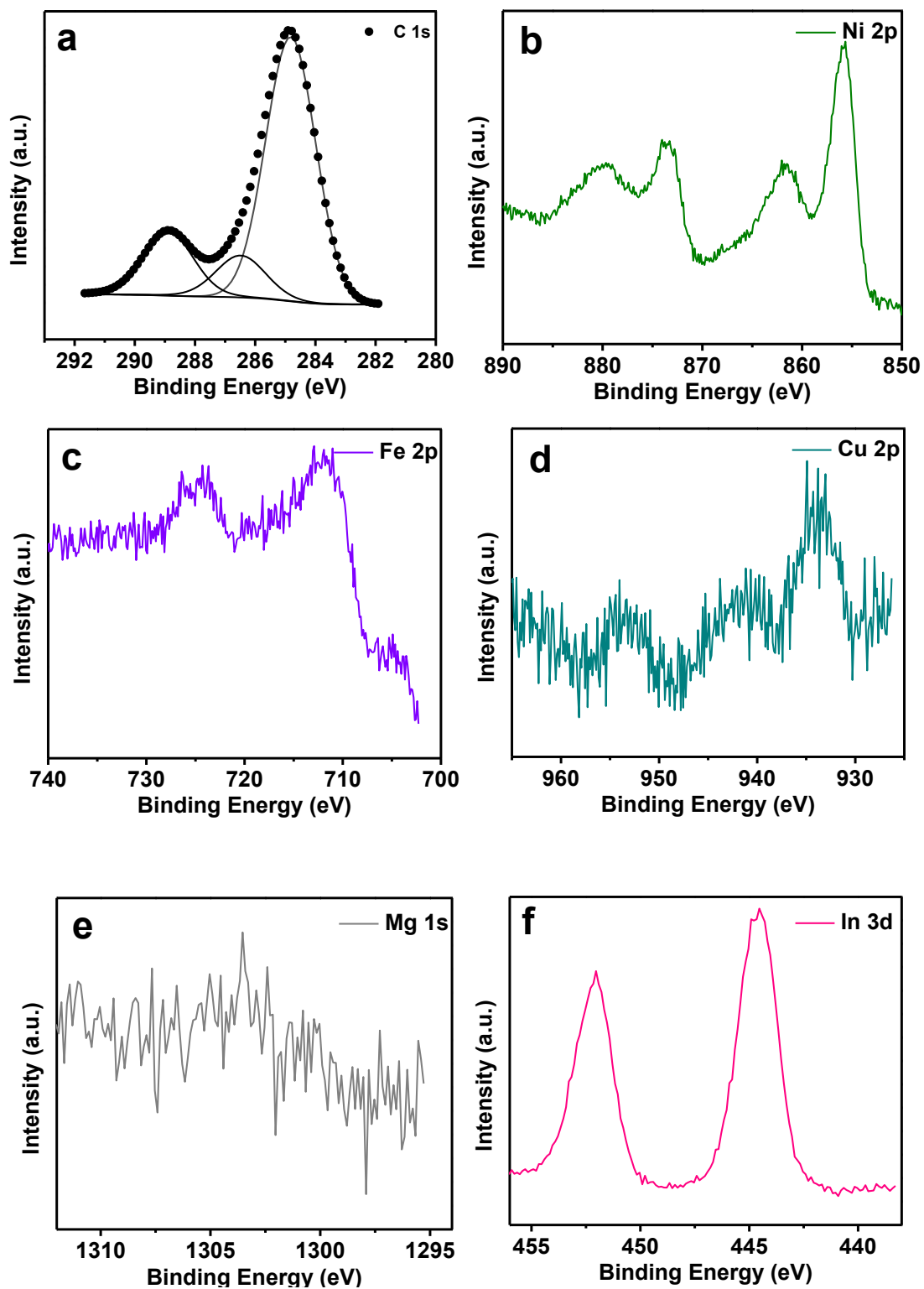
Figure S10. XPS spectrum of the, (a) C 1s element of HE-LDH, (b) Ni 2p element of HE-LDH, (c) Fe 3p element of HE-LDH, (d) Cu 2p element of HE-LDH, (E) Mg 1s element of HE-LDH, and (f) In 3d element of HE-LDH.
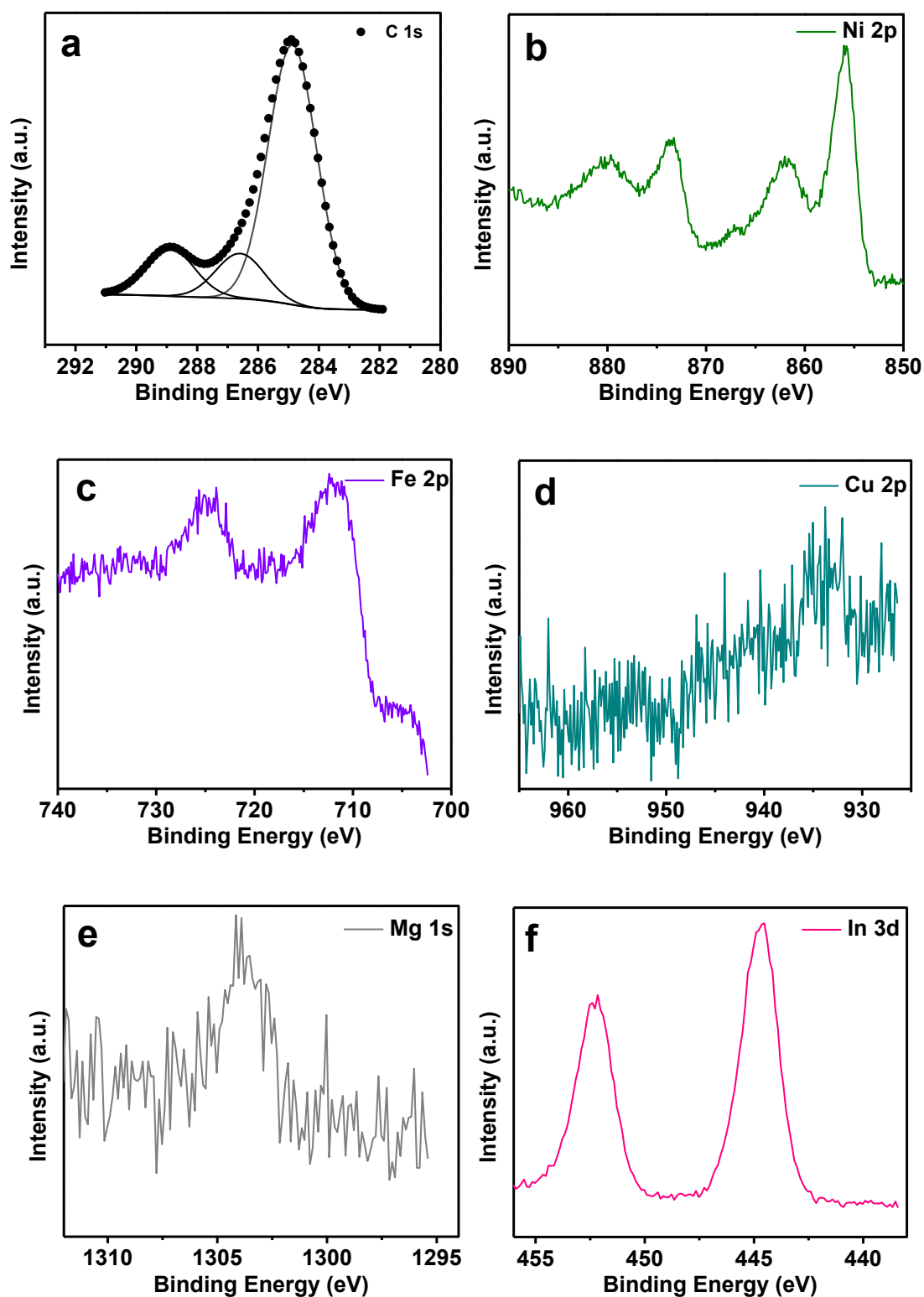
Figure S11. XPS spectrum of the, (a) C 1s element of et-HELDH, (b) Ni 2p element of et-HELDH, (c) Fe 3p element of et-HELDH, (d) Cu 2p element of et-HELDH, (E) Mg 1s element of et-HELDH, and (f) In 3d element of et-HELDH.
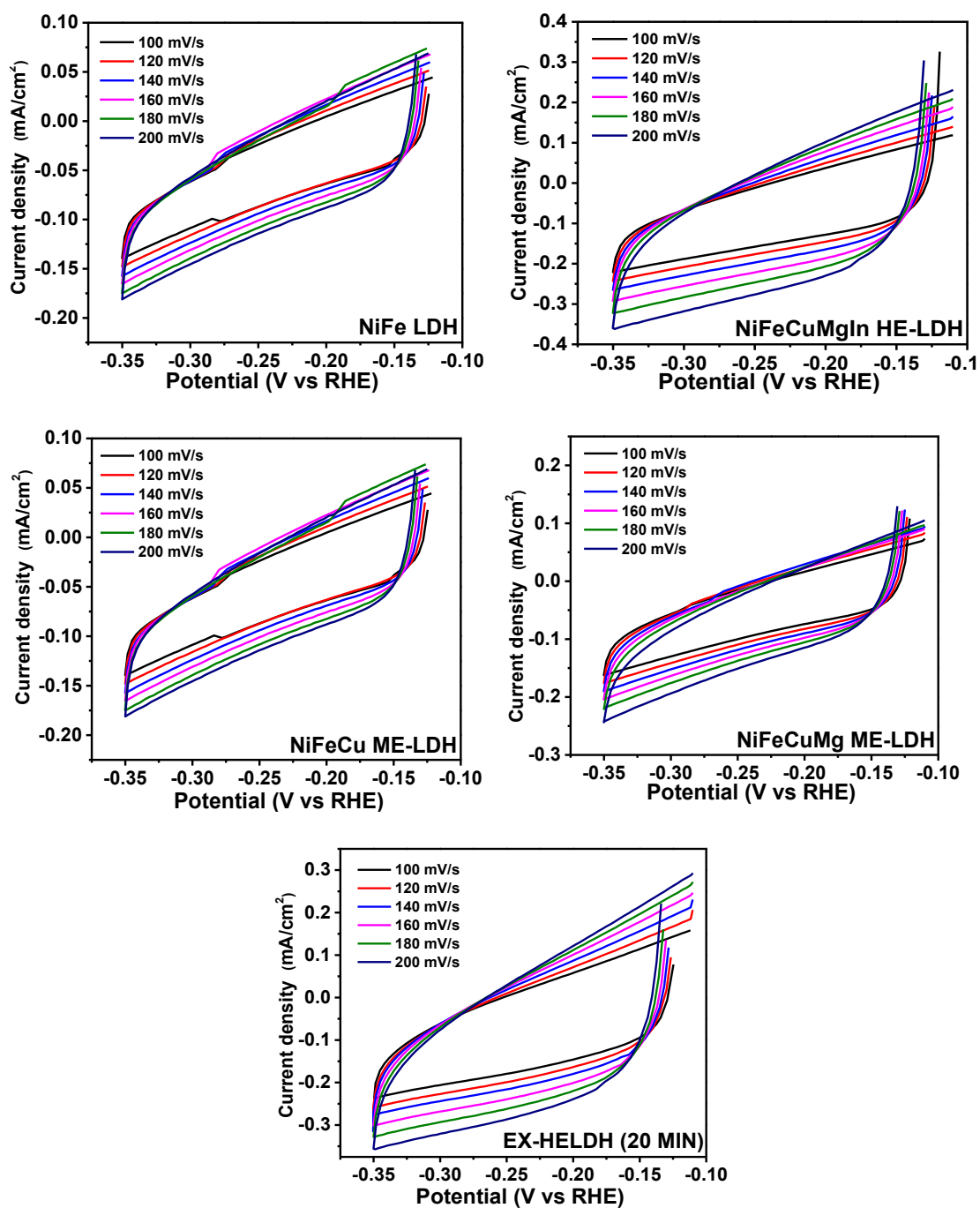
Figure S12. CV curves for different catalysts recorded in 0.5 M KOH at different scan rates.
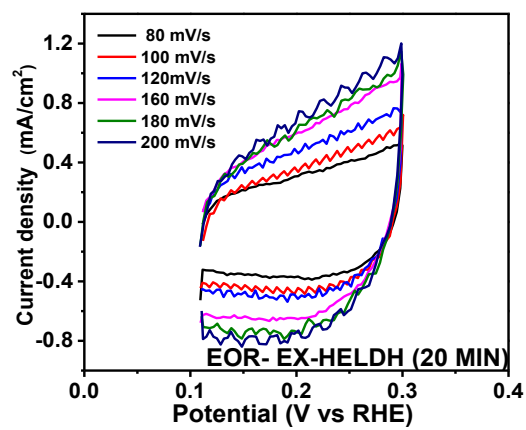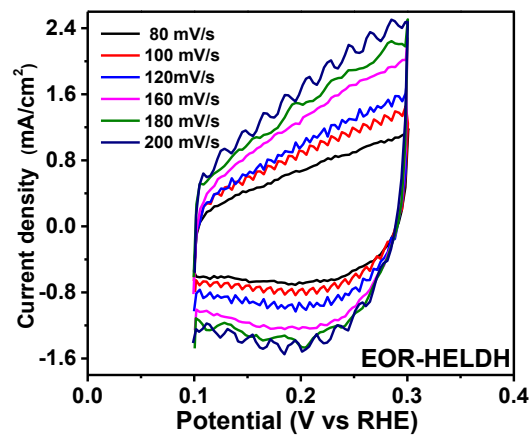
Figure 13. CV curves for different catalysts recorded in a mixed electrolyte solution containing (0.5 M KOH + 1 M EtOH) at different scan rates.
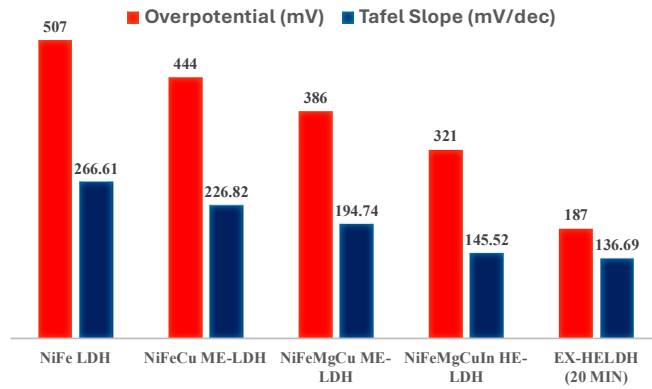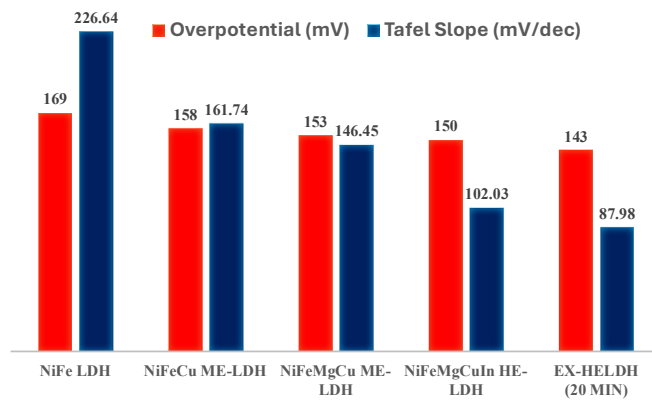
Chart 1. Summary of HER performance across all samples
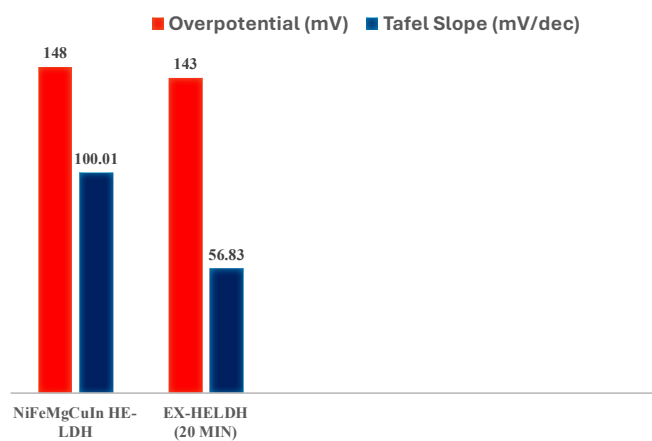

Chart 2. Summary of OER performance across all samples.

Chart 3. Summary of EOR performance across HE-LDH samples.